Developing and applying efficient DD-vMCG method for nonadiabatic simulations

Georgia Christopoulou

A dissertation submitted in partial fulfillment

of the requirements for the degree of

Doctor of Philosophy

of

University College London.

Chemistry Department

University College London

July 11, 2021

I, Georgia Christopoulou , confirm that the work presented in this thesis is my own. Where information has been derived from other sources, I confirm that this has been indicated in the work. Text taken from another source will be enclosed in quotation marks and a reference will be given.

Abstract

Gaussian wavepacket methods have been widely employed for the investigation of nonadiabatic molecular dynamics. The Direct Dynamics variational Multi-Configurational Gaussian (DD-vMCG) method provides a fully quantum mechanical solution to the time-dependent Schrödinger equation for the time evolution of nuclei with potential surfaces calculated *on-the-fly* using a quantum chemistry program. The first strand of this research study was to develop new, more efficient algorithms and improve the existing code for DD-vMCG aiming to increase both the accuracy and efficiency of this method. Thus, a new, efficient parallel algorithm to control the DD-vMCG database of quantum chemistry points is presented along with improvements to the interpolation scheme. Benchmark calculations on butatriene, allene and formamide showed that the new scheme is a very accurate, efficient and general method to employ for full-dimensional dynamics calculations.

The aforementioned algorithm was then used to describe the photodissociation dynamics of phenol including all degrees of freedom, as the second strand of this research work was to explore more complex chemical systems. Full-dimensional quantum dynamics calculations including for the first time six electronic states, along with a detailed comparison with existing 3-state and 4-state models are presented. Including the fifth singlet excited state has been shown to be vital in unravelling the photodissociation of phenol. State population and flux analysis provided new insights into the decay mechanism of phenol confirming the idea of rapid relaxation to the ground state through the $^1\pi\pi/1^1\pi\sigma^*$ conical intersection.

Finally, an effort to further improve the accuracy of DD-vMCG was made by employing a state-of-the-art approach where a Gaussian process regression scheme is introduced and machined-learned potential energy surfaces are obtained. All the findings suggest that this method could be promising to calculate potential

energy surface matrix elements. However, further development is essential to take advantage of its benefits and to deal with the computational cost.

Impact Statement

Understanding various chemical phenomena, such as photodissociation, occurring in a molecular system requires us to define the potential energy surfaces. To this end, the Born-Oppenheimer approximation is employed which enables decoupling the electronic and nuclear motions. However, upon consideration of the molecular dynamics in excited electronic states, this approximation breaks down. Describing the dynamics of a chemical system when the Born-Oppenheimer approximation is no longer valid, involves a quantum mechanical description of the nuclei.

Various methods exist which can describe nonadiabatic dynamics offering different levels of accuracy and flexibility. One of the most accurate methods is multi-configuration time-dependent Hartree (MCTDH) as it can provide numerically exact results for molecules. However, this method is not flexible as it requires precalculated potential energy surfaces. As a solution to overcome the former restriction, the variational multi-configurational Gaussian (vMCG) method was developed where the basis functions of MCTDH are replaced with Gaussian functions. This thesis is fully focused on the DD-vMCG method which has shown potential for flexible and accurate simulations of non-adiabatic excited-state molecular dynamics.

The original work presented in this thesis has a tangible impact on the area of molecular quantum dynamics as complex chemical systems can be now efficiently and accurately treated with DD-vMCG. Moreover, our work can be used from different research groups designing programs to analytically compute the potential energy surfaces of a molecule as it has been shown that the new efficient algorithm for DD-vMCG is able to better describe the dynamics of a molecule with less computational cost while offering more flexibility. The development work carried

out for DD-vMCG has been published and also accepted in the European HPC Centre of Excellence (E-CAM) software library.

Moreover, the successful investigation of the dissociation process of the phenol molecule carried out in this study has an important scientific value. Since phenol is the chromophore of the amino acid tyrosine and a major component of green fluorescent protein chromophores, the work in this thesis can reach a wide range of different researchers especially those focusing on protein investigation and design. This work has been submitted for publication.

Finally, the findings on machine-learned potentials could lead the way to improving GAP-vMCG and possibly in the future to be the sole method used for *on-the-fly* vMCG calculations.

Acknowledgements

The PhD journey was a wonderful and unique experience even through it was a period with a lot of stress and self-doubting and long days and especially in my case even longer nights trying to understand science and to find answers to complex questions. Maybe there is the magic in the joy of grasping a new idea that gave me the strength to continue and enjoy this big chapter in my life. This journey would have not been the same without the encouragement, the support and the consideration of all the people in my life.

My deepest appreciation goes to my supervisor Graham Worth for sharing his knowledge and enthusiasm about quantum chemistry, for taking the time to respond to every question I had (which were a lot!) and for always bringing optimism and joy to work. I feel incredibly lucky for having him as my PhD supervisor and very honoured to say that I was part of the Worth group (hopefully I will still be able to join for a pint of beer!).

Thanks to my colleagues in the Worth group, both new and old, for always being willing to help, to share their knowledge and to have fun with karaoke nights and board games. Special thanks to Thierry for his unreserved scientific help and to Sandra for her support, the fun we had in the last years and for being a very good friend.

For the love and for encouraging me to follow my dreams even when this meant moving abroad, I would like to thank my dad and mum and my siblings Roula and Marios. A million thanks to my UK friends, Marianna, Myropi, Maria-Eirini, Vaggelis, Eirini, Dimitra, Artemis, Angeliki and Kostas; and to my friends in Greece, Elena and Marietta for the countless calls, and to Dora for travelling around Greece and the world together and for always being my safe place. Special thanks to my friend Iasmi for being my biggest supporter and to my soon to be

goddaughter Ioli whose thought has been always filling me with happiness.

Finally, I would like to thank my best friend and partner George for always being by my side, believing in me, supporting me and for all the small things that are so precious to me. Thanks a lot for always being the brightest color in my life!

List of Publications

1. G. Christopoulou, A. Freibert, and G. A. Worth. Improved algorithm for the direct dynamics variational multi-Configurational Gaussian method. *J. Chem. Phys.*, (In Press).

2. G. Christopoulou, T. Tran, and G. A. Worth. Excited state non-adiabatic quantum dynamics simulations of the photodissociation of phenol. *Phys. Chem. Chem. Phys*, (Submitted).

Contents

List of Figures **xi**

List of Tables **xiii**

Glossary **xvi**

1 Introduction **1**

2 Theory **8**

2.1 Introduction 8

2.2 The Schrödinger Equation 8

2.3 The Hamiltonian 11

2.4 Born-Oppenheimer Approximation 12

2.5 Adiabatic Representation 15

2.6 Non-Adiabatic Corrections 16

2.7 Vibronic Coupling and Diabatic Representation 17

2.8 Potential Energy Surfaces 19

2.9 The Role of Conical Intersections 22

3 Methodology **24**

3.1 Introduction 24

3.2 Electronic Structure 24

3.2.1 Hartree-Fock Method 25

3.2.2 Basis Sets . . . 27
3.2.3 Beyond the Hartree-Fock Method . . . 29
3.3 Nuclear Dynamics . . . 31
3.3.1 Multi-Configuration Time-Dependent Hartree Method . . . 33
3.3.2 Variational Principles . . . 35
3.3.3 Variational Multi-Configurational Gaussian Method . . . 36
3.3.4 Direct Dynamics . . . 39
3.3.5 The Quantics Package . . . 49

4 Developing DD-vMCG 51
4.1 Introduction . . . 51
4.2 Modified Shepard Interpolation . . . 52
4.3 Local Dynamic Database . . . 54
4.3.1 Conceptual Development . . . 54
4.3.2 Code Implementation . . . 59
4.4 Parallelisation . . . 64
4.4.1 Parallel Environments in High Performance Computing . . . 64
4.4.2 Running Quantics on Parallel Architectures . . . 66
4.5 Test Cases . . . 68
4.5.1 Butatriene Cation . . . 68
4.5.2 Allene Radical Cation . . . 78
4.5.3 Formamide . . . 86
4.6 Summary . . . 93

5 Applying DD-vMCG to Study the Photodissociation of Phenol 95
5.1 Introduction . . . 95
5.2 Phenol . . . 96
5.3 External Molecular Potential Program . . . 100

5.4 Electronic structure and geometry optimisations . . . 103
5.5 Computational Details . . . 104
5.5.1 DD-vMCG Protocol . . . 104
5.5.2 Complex Absorbing Potential (CAP) and Flux Operator . . 106
5.6 Quantum Dynamics Calculations . . . 108
5.6.1 Potential Energy Surfaces . . . 108
5.6.2 State Population Analysis . . . 119
5.6.3 Flux Analysis . . . 124
5.7 Discussion . . . 126

6 Direct Dynamics using Gaussian Process Regression 129

6.1 Introduction . . . 129
6.2 Local Harmonic Approximation . . . 131
6.3 Gaussian Process Regression . . . 134
6.3.1 Introduction . . . 134
6.3.2 The General Algorithm . . . 136
6.3.3 Calculation of Potential Energy Surface Matrix Elements . . 138
6.4 Results . . . 141
6.4.1 Computational Details . . . 141
6.4.2 Ozone . . . 142
6.4.3 Analysis . . . 143
6.5 Discussion and Future Work . . . 154

7 Conclusions and Future Work 157

Bibliography 161

List of Figures

1.1 The Jablonski diagram showing the possible relaxation pathways following an excitation to an S_1 excited state where IC denotes the internal conversion and ISC the intersystem crossing. S_0 is the ground electronic state, S_1 and S_2 are excited singlet states and T_1 is the lowest triplet state. Adapted from ref.[4] 2

1.2 Potential energy surfaces of the S_0 and S_1 states of the cis-trans isomerization in rhodopsin. Reprinted with permission from Hahn, S.; Stock, G.J. *Phys. Chem.* **2000**, 104, 1146–1149. Copyright 2000 American Chemical Society. 3

1.3 Schematic representation of different methods for non-adiabatic molecular dynamics. Reprinted with permission from Curchod, B.; Martínez, T. *Chem. Rev.* **2018**, 118, 3305–3336. Copyright 2018 American Chemical Society. 6

2.1 The diabatic (a) and adiabatic (b) potential energy surfaces of the butatriene molecule along the C-C symmetric stretching mode, $14Ag$, and the CH_2 twisting mode, $5Au$. 19

2.2 Schematic two-dimensional representation of (a) a minimum, (b) a maximum stationary point and (c) a sadle point. 21

3.1 The flux of the wavepacket over the proton transfer of the salicylaldimine molecule as the number of GWPs increases. Reprinted with permission from ref. 82. 44
3.2 The flux of the wavepacket over the proton transfer of the salicylaldimine molecule as the dbmin parameter increases. Reprinted with permission from ref. 82. 46
3.3 Total number of points in the database for the salicylaldimine molecule in terms of the number of the propagations carried out, using as a starting point the database from the previous run. Reprinted with permission from ref. 82. 48

4.1 Attributes of computational methods. 52
4.2 Schematic representation of DD-vMCG method for excited-state dynamics where the green dots represent the centre of the GWP, the red dots the database energies and the black lines the fit to those points. 55
4.3 Flow chart showing the layout of the DB scheme. 58
4.4 Distance criterion for calculating a new point. 63
4.5 Illustration of a) a sequential program in comparison with b) a program using the fork/join parallel function of OpenMP. 64
4.6 Schematic of a single shared memory multiple processor node where C_i denotes the corresponding cache and P_i a processor. 65
4.7 Schematic of a cluster computer with multiple nodes, where C_{ii} denotes the cache assigned to the P_{ii} processor. 66
4.8 The equilibrium ground state structure of butatriene. 69

4.9 Two-dimensional cuts through the a) adiabatic and c) diabatic potential energy surfaces employing the original DD-vMCG version, and the b) adiabatic and d) diabatic potential energy surfaces employing the developed DD-vMCG version for butatriene cation along the $\nu_5(B_1)$ and $\nu_{11}(B_2)$ normal modes. 71
4.10 Normalised diabatic state population from DD-vMCG simulations of butatriene cation using a) the original DD-vMCG version and b) the developed local DB DD-vMCG version. 72
4.11 Total energy for butatriene as a function of time using a) the original and b) the improved interpolation scheme for direct dynamics. . . . 72
4.12 The population of S_0 (blue line) and S_1 (orange line) states for the same DD-vMCG calculation of butatriene cation employing a) the full DB with 115 points and the local DB with b) 4 points, c) 6 points and d) 10 points 75
4.13 The equilibrium ground state structure of allene. 79
4.14 Two-dimensional cuts through the a) adiabatic and c) diabatic potential energy surfaces employing the old DD-vMCG version, and the b) adiabatic and d) diabatic potential energy surfaces employing the new DD-vMCG version for allene cation along the $\nu_5(B_1)$ and $\nu_{11}(B_2)$ normal modes. 81
4.15 Normalised diabatic state populations from DD-vMCG simulations of allene cation using a) the original and b) the developed DD-vMCG version 82
4.16 Total energy for allene cation as a function of time using a) the original and b) the improved interpolation scheme for direct dynamics. 82

4.17 The population of S_0 (blue line) and S_1 (orange line) states for the same DD-vMCG calculation of allene cation employing a) the full DB with 317 points and the local DB with b) 4 points, c) 6 points and d) 10 points. 84
4.18 The equilibrium ground state structure of formamide. 86
4.19 One-dimensional cuts through a) the adiabatic and b) the diabatic potential energy surfaces of formamide along the ν_{11} N-H_2 symmetric stretching mode, and c) adiabatic and d) diabatic potential energy surfaces along the ν_{12} N-H_2 antisymmetric stretching mode employing the original DD-vMCG implementation. 88
4.20 One-dimensional cuts through a) the adiabatic and b) the diabatic potential energy surfaces of formamide along the ν_{11} N-H_2 symmetric stretching mode and c) adiabatic and d) diabatic potential energy surfaces along the ν_{12} N-H_2 antisymmetric stretching mode employing the new developed DD-vMCG implementation. 89
4.21 Normalised diabatic state population from DD-vMCG simulations of formamide using a) the original and b) the developed DD-vMCG version: S0: purple; S1: green; S2: light blue; S3: orange; S4: yellow; S5: dark blue; S6: red; S7: black. 90
4.22 Total energy for formamide as a function of time using a) the original and b) the improved interpolation scheme for direct dynamics. . . . 90

5.1 The equilibrium ground state structure of phenol. 97
5.2 Potential energy curves of the (a) adiabatic and (b) diabatic picture for the ground and excited singlet states as a function of R, the O-H bond distance. 98
5.3 Molecular orbitals used for the CASSCF calculation with phenol for the 10 electrons in 10 orbitals. 104

5.4 The three main coordinates of phenol accompanied with the associated normal modes during the DD-vMCG propagation. Reprinted with permission from Xie, C.; Ma, J.; Zhu, X.; Yarkony, D. R.; Xie, D.; Guo, H. *J. Am. Chem. Soc.* **2016**, 138, 7828–7831. Copyright 2016 American Chemical Society. 108

5.5 Cuts through the potential energy surfaces of phenol obtained from a DD-vMCG simulation employing OpenMolcas with a three states averaging, (a) adiabatic and (b) diabatic, and employing the 3-state PES_{XZYT} model for phenol as the external quantum chemistry program, (c) adiabatic and (d) diabatic, in the space of the O-H bond stretch, ν_{33}, normal mode. All other coordinates have a value of zero. 109

5.6 Cuts through the potential energy surfaces of phenol obtained from a DD-vMCG simulation employing OpenMolcas with a four states averaging, (a) adiabatic and (b) diabatic, and employing the 4-state PES_{ZY} program as the external program, (c) adiabatic and (d) diabatic, and obtained directly from the diabatic representation generated by the PES_{ZY} program (e) diabatic, in the space of the O-H bond stretch, ν_{33}, normal mode. All other coordinates have a value of zero. 111

5.7 Cuts through the (a,c) adiabatic and (b,d) diabatic 6- and 5-state potential energy surfaces, in the space of the O-H bond stretch, ν_{33}, normal mode employing DD-vMCG method with OpenMolcas. All other coordinates have a value of zero. 114

5.8 Cuts through the (a,c,e,g) adiabatic and (b,d,f,h) diabatic 6-, 5-, 4- and 3-state potential energy surfaces, in the space of the C-Ô-C bond angle, ν_{24}, normal mode employing DD-vMCG with OpenMolcas. All other coordinates have a value of zero. 117

5.9 Cuts through the (a,c,e,g) adiabatic and (b,d,f,h) diabatic 6-, 5-, 4- and 3-state potential energy surfaces, in the space of the CCOH torsion, ν_2, normal mode employing DD-vMCG with OpenMolcas. All other coordinates have a value of zero. 118

5.10 Diabatic state populations from DD-vMCG simulations of phenol starting with a vertical excitation to $\tilde{A}$ and $\tilde{B}$ states for the 3-state model. 119

5.11 Diabatic state populations from DD-vMCG simulations of phenol starting with a vertical excitation to $\tilde{A}$, $\tilde{B}$ and $\tilde{C}$ states for the 4-state model. 121

5.12 Diabatic state populations from DD-vMCG simulations of phenol starting with a vertical excitation to $\tilde{A}$, $\tilde{B}$, $\tilde{C}$ and $\tilde{D}$ states for the 5-state model. 122

5.13 Diabatic state populations from DD-vMCG simulations of phenol starting with a vertical excitation to $\tilde{A}$, $\tilde{B}$, $\tilde{C}$, $\tilde{D}$ and $\tilde{E}$ states for the 6-state model. 123

5.14 Normalised integrated flux as a function of time from DD-vMCG simulations of phenol starting with a vertical excitation to $\tilde{A}$ and $\tilde{B}$ states for the 4- and 6-state models. 125

6.1 Schematic representation of accuracy of different quantum chemistry methods and machine learning approximations as a function of timing (computational cost). SQC denotes the semiempirical quantum chemistry methods. Adapted with permission from ref. 198. 130

6.2 The equilibrium ground state structure of ozone. 143
6.3 One-dimensional cuts through the a) adiabatic and b) diabatic potential energy surfaces employing DD-vMCG, and the c) adiabatic and d) diabatic potential energy surfaces employing the GAP-vMCG method for ozone, in the space of the symmetric O-O bond stretch, ν_1, normal mode. All other coordinates have a value of 0. 144
6.4 One-dimensional cuts through the a) adiabatic and b) diabatic potential energy surfaces employing DD-vMCG, and the c) adiabatic and d) diabatic potential energy surfaces employing the GAP-vMCG method for ozone, in the space of the asymmetric O-O bond stretch, ν_3, normal mode. All other coordinates have a value of 0. 146
6.5 One-dimensional cuts through the a) adiabatic and b) diabatic potential energy surfaces employing DD-vMCG, and the c) adiabatic and d) diabatic potential energy surfaces employing the GAP-vMCG method for ozone, in the space of the O-O-O bond angle, ν_2, normal mode. All other coordinates have a value of 0. 147
6.6 One-dimensional cuts through the adiabatic potential energy surfaces along various coordinates obtained from DD-vMCG calculations (a,c,e) and (b,d,f) reprinted from Batista, V. S.; Miller, W. H.J. Chem. Phys. 1998, 108, 498–510, with the permission of AIP Publishing. 149
6.7 Normalised diabatic state populations from (a) DD-vMCG and (b) GAP-vMCG simulations of ozone starting with a vertical excitation to the $\tilde{B}(^1B_1)$ state for a 3-state model. 150

6.8 One-dimensional cuts through the adiabatic potential energy surfaces varying the α hyperparameter and employing the GAP-vMCG method for ozone, in the space of the O-O-O bond angle, ν_2, normal mode. All other coordinates have a value of 0. 152

List of Tables

4.1 Main subroutines in the Quantics program involved in using the DB. 59

4.2 The total elapsed time for serial DD calculations for the local DB and the full QC database when varying the number of points in the full QC database by using different distance criteria (dbmin values). For all calculations the n_{conf} parameter was equal to 6. 74

4.3 The total wall-clock time for a parallel implementation of DD-vMCG using local DBs, with different number of cores[1] for butatriene cation. 76

4.4 The total elapsed time for serial DD-vMCG calculations with 10 GWPs using the full QC database and local databases, varying the number of points in the QC database by using different distance criteria (dbmin values). For all calculations the n_{conf} parameter was equal to 6. 83

4.5 The total wall-clock time for a parallel implementation of DD-vMCG using local DBs, with different number of cores.[1] 85

4.6 The total elapsed time for serial DD-vMCG calculations with 10 GWPs using the full QC database and local databases, varying the number of points in the QC DB by using different distance criteria (dbmin values). For all calculations the n_{conf} parameter was equal to 6. 92

4.7 The total wall-clock time for a parallel implementation of DD-vMCG using local DBs, with different number of cores.[1] 93

5.1 Summary of state characters and symmetries (in C_s) and comparison of experimental and theoretical excitation energy (in eV) with those obtained by employing a CASSCF(10,10)/6-311+Gpp level of theory at the Franck–Condon point and for different state-averaging. 115

Glossary

ab initio From the latin term meaning "from the beginning". It is derived from "ab" meaning "from" and "initio" being the singular form of "initium" meaning "beginning". In the context of computational Chemistry it is usually refers to the methods by which the time-independent Schrödinger equation is solved, without the use of experimental data. 5, 24, 25, 27, 28, 46, 97, 132, 134

AIMS Ab-Initio Multiple Spawning. This method is a time-dependent formulation of quantum chemistry, developed by the group of Todd Martinez, used for running on-the-fly Ab-initio multiple spawning with a focus on the use of Graphics Processing Units to speed up calculations[1–3]. 5, 134

BOA Born-Oppenheimer approximation. 8, 15, 17, 24, 31

CAP Complex Absorbing Potential. 106, 107

CASSCF Complete Active Space Self-Consistent Field (method). 30, 31, 69, 79, 100

CI Configuration interaction. 29–31

CISD Configuration Interaction Singles and Doubles. 100, 105

CoI Conical Intersection. 8, 22, 23, 80, 99, 112, 123, 125, 143, 145, 148

CPU Central Processing Unit. 75, 83, 84

DB Database. v–vii, xii, xiii, 52, 54–63, 67, 68, 70, 72–77, 80, 82–85, 89–94, 153

DD-vMCG Direct-Dynamics Variational Multi-Configurational Gaussian (method). An on-the-fly quantum dynamics method based on vMCG. v–vii, x, xii, xiii, 4–7, 24, 39, 40, 42, 43, 48, 51, 52, 55, 56, 61, 63, 68–72, 74–76, 79–85, 87–90, 92–96, 100, 105, 106, 108, 110, 115, 126, 129, 131–133, 141–144, 146, 147, 149–151, 153–159

DOF Degree(s) of freedom. 15, 33, 34, 39, 131, 139, 154

DVR Discrete variable representation. 35

GAP-vMCG Direct-Dynamics Variational Multi-Configurational Gaussian method employing Gaussian-approximation potentials. x, xi, 131, 135, 140–148, 150–156, 159, 160

G-MCTDH Gaussian - MultiConfiguration Time-Dependent Hartree (method) where some of the SPFs of the Multi-Configuration Time-Dependent Hartree method are replaced by Gaussian functions. 35

GP Gaussian process also known as normal stochastic process. 136

GPR Gaussian Process Regression. 130, 134, 135, 137–142, 155, 156

GWP Gaussian wavepacket. v, 5, 36, 39, 40, 42–47, 55, 56, 59–62, 70, 76, 77, 80, 82–88, 91–94, 100, 105, 129, 131–135, 139–141, 156

LHA Local harmonic approximation. 36, 41, 129–131, 135, 140–142, 155, 156, 159

MCSCF Multiconfiguration Self-Consistent Field (theory). 30, 31

MCTDH Multi-Configuration Time-Dependent Hartree (method). 4, 33–35, 49, 106, 135, 143

ML Machine Learning. 129

MPI Message Passing Interface. 64, 65, 67

on-the-fly "As needed." Usually referring to a dynamics method that does not require precomputed potential energy surfaces and hence the surfaces are calculated as needed. xv, 4, 5, 7, 40, 47, 49, 132, 135

OpenMP Open Multi-Processing. v, 64, 65, 67

PES Potential energy surface. 2, 3, 17, 19–21, 32, 33, 39, 42, 48, 53, 56, 68, 98, 123, 126, 127, 129, 130, 132–135, 139, 141, 143–145, 147, 151, 154–156

QC Quantum Chemistry. xii, 57, 59–61, 68, 73, 74, 82, 91

SPF Single-particle function(s). xvi, 33–35

TDSE Time Dependent Schrödinger Equation. 3, 4, 34, 35

vMCG Variational Multi-Configurational Gaussian (method) where all SPFs of the Multi-Configuration Time-Dependent Hartree method are replaced with Gaussian functions. xv, 5, 35, 39, 49, 88, 134, 141, 145, 154, 159

Chapter 1

Introduction

Photochemistry and more specifically photochemical reactions has a wide range of applications, with some of them crucial to everyday life such as photosynthesis, vitamin D synthesis and vision. In simple terms, photochemistry focuses on the interaction between light and a chemical system and describes the promotion of this system to an excited state and its subsequent reactions. An excited molecule has properties, in particular its lifetime and energy, that depend on the nuclear and electronic configuration of the excited state. In a more general sense, photochemistry is outlined as the investigation of the time evolution of the electronic and nuclear structure after excitation where a plethora of pathways are available. These pathways allow transitions between the different electronic states of a chemical system.

The different possible photodynamics processes are illustrated in the Jablonski diagram, Fig. 1.1. The depicted transitions are divided into two categories, the *radiative* where the transition is accompanied with a photon and the *non-radiative* where it is not. Phosphorescence and fluorescence are both radiative transitions that take place between states of different spins, or the same spin, respectively. Intersystem crossing (ISC) and internal conversion (IC) belong to the non-radiative category and take place between states of different spin and same spin, respectively.

To unravel the photodissociation of a chemical system, apart from understand-

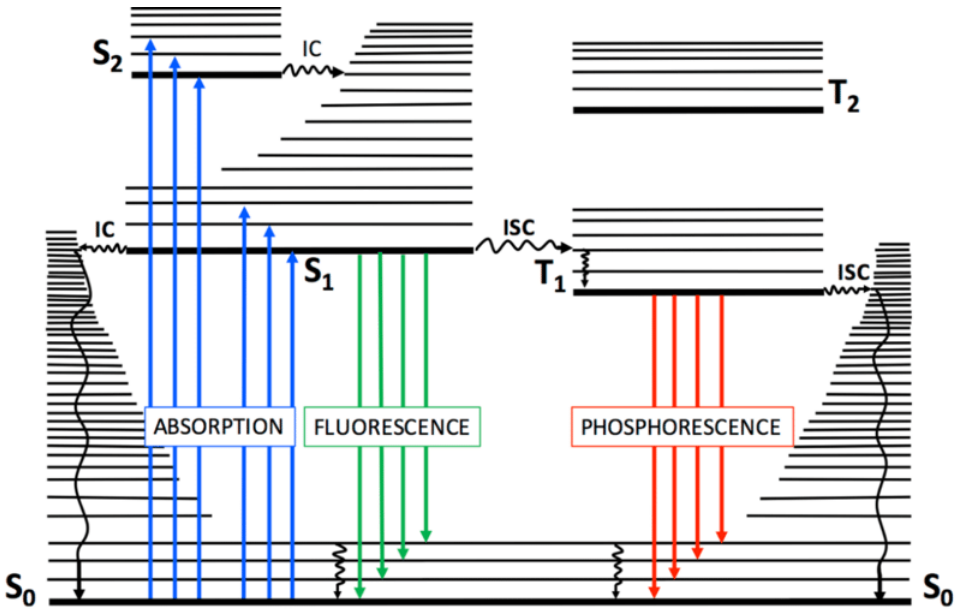

Fig. 1.1: The Jablonski diagram showing the possible relaxation pathways following an excitation to an S_1 excited state where IC denotes the internal conversion and ISC the intersystem crossing. S_0 is the ground electronic state, S_1 and S_2 are excited singlet states and T_1 is the lowest triplet state. Adapted from ref.[4]

ing the excited-state properties of this system from a static picture that the Jablonski diagram offers, it is also essential to establish the bond breaking and bond making in these excited states which requires a better understanding of how the molecule evolves chemically. Hence, obtaining a clear picture of the reaction pathways along the potential energy surfaces (PESs) of the photochemically active electronic states is very important. These ideas are illustrated in Fig. 1.2 where the mechanistic picture of the photoexcitation process in rhodopsin is illustrated. This schematic representation of the PESs is crucial as it plays a significant role in the interpretation of experimental data.

Various spectroscopic techniques exist such as femtosecond spectroscopy where ultrafast laser pulses are employed to study molecular processes on femtosecond timescales.[5–8] Another important technique which is based on femtochemistry is attosecond spectroscopy[9,10] where the electron dynamics of a chemical system are studied. These experimental techniques are essential to investigate a system,

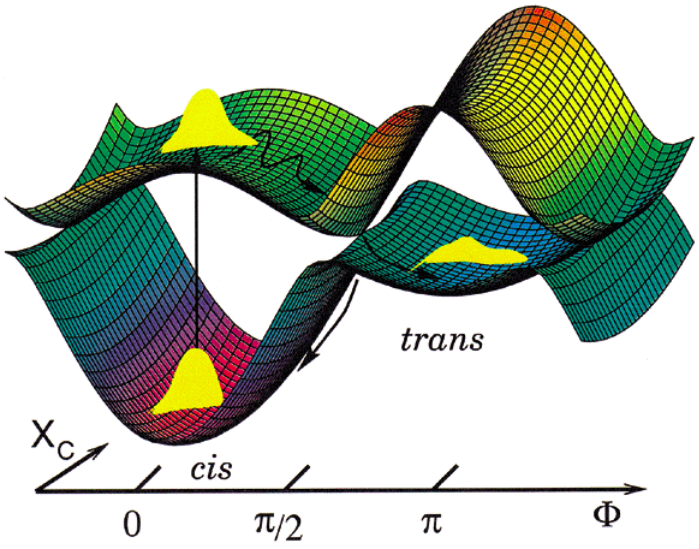

Fig. 1.2: Potential energy surfaces of the S_0 and S_1 states of the cis-trans isomerization in rhodopsin. Reprinted with permission from Hahn, S.; Stock, G.J. *Phys. Chem.* **2000**, 104, 1146–1149. Copyright 2000 American Chemical Society.

however, the spectroscopic results are sometimes hard to interpret. Computational photochemistry with advanced computer simulations plays a key role in answering why and how these complicated processes occur.

Computational photochemistry is an essential tool for the investigation of photochemical reaction mechanisms in molecular systems. This is a consequence of the continuous advance in computational power along with theoretical developments in the quantum chemistry field. These improvements enabled the investigation of other regions of the PESs apart from vertical excitations at the Franck–Condon geometry. Further, nonadiabatic molecular dynamics simulations have enabled significant breakthroughs in the understanding of photochemical processes. Nowadays, computational photochemistry investigations such as photoinduced electron transfer, photodissociation and photoisomerization are well established.

Describing the aforementioned dynamical processes and studying how quantum mechanical systems evolve in time, requires solving the time-dependent Schrödinger equation (TDSE). As it is difficult to solve the Schrödinger equation for complex systems, the Born-Oppenheimer approximation[11] is employed that simplifies the

eigenvalue problem. Within the Born-Oppenheimer approximation for the separation of electronic and nuclear motions, the nuclei move on potential energy surfaces provided by the electrons. In this way, an electronic Schrödinger equation[12] is solved for a set of fixed nuclear arrangements, yielding the potential energy surface for the nuclei motion through a specific electronic state, to obtain the resolution of the molecular problem within the so-called *adiabatic approximation.*[13–17] In general, for a N atoms molecular system, the potential energy surface is a function of the $3N$ nuclear Cartesian coordinates, $\mathbf{x} = (x_1, y_1, z_1, ..., x_N, y_N, z_N)$ which is completely described by $3N - 6$ linearly independent coordinates ($3N - 5$ for a linear molecule), as the Hamiltonian is invariant to rotation and translation of the entire system.

Direct Dynamics is the branch of molecular dynamics simulations that solves the TDSE by allowing the calculation of potential energy surfaces on-the-fly.[18,19] This enables the analysis of the influence of quantum effects on reactivity without the time-consuming need to pre-compute potential energy surfaces. One of the major advantages of this method is that it is feasible to treat any system available to quantum chemistry as simply as using a modern quantum chemistry computer program. In this research study the *Direct Dynamics variational multi-configuration Gaussian wavepacket* (DD-vMCG) method[18,19] is employed, which is derived from the multi-configuration time-dependent Hartree (MCTDH) method. DD-vMCG is a fully variational solution to the TDSE, i.e. it can provide a complete representation of the time evolution of the system treating both nuclei and electrons quantum mechanically. In its present implementation, all energies, gradients and Hessians calculated during a propagation are stored in a database. One bottleneck of this method is the time needed to continually reread, sort and analyse this database which makes the calculation of a large system very expensive. To this end, the challenge is to improve the existing method to be more efficient

so that larger molecules such as the green fluorescence protein can be treated.[20] The DD-vMCG method is included in the powerful and flexible Quantics software package.[21]

Other methods for non-adiabatic molecular dynamics also exist. Of the most successful are trajectory surface hopping methods and Ehrenfest dynamics,[22–27] which are mixed quantum-classical techniques where quantum mechanical effects are incorporated into classical molecular dynamics simulations. The basic idea in surface hopping dynamics is that a set of electronic amplitudes are integrated with the classical trajectories, and determines the probability of the trajectory hopping between electronic states. These methods offer the advantage of a less computationally expensive method compared to DD-vMCG. However these are approximate methods.

Gaussian-based quantum dynamics methods similar to DD-vMCG where the electronic structure quantities, energies and gradients, are calculated on-the-fly include *ab initio* multiple spawning[1–3] (AIMS) which is a time-dependent quantum chemistry formulation, comprising of a simultaneous solution of nuclear dynamics and electronic structure problems. Another Gaussian wavepacket (GWP) method is multi-configurational Ehrenfest dynamics[28,29] (MCE) which focuses on non-adiabatic dynamics and it is someway in-between AIMS and vMCG as an effort to combine some of the best features of these two techniques has been made. Both AIMS and MCE are in principle exact, however they have poorer convergence properties than vMCG. A schematic representation of the former direct non-adiabatic dynamics methods is given in Fig. 1.3.[1]

The aforementioned methods are not the only ones available for non-adiabatic dynamics but the ones where the nuclear wave function is expanded as a linear combination of travelling Gaussian basis functions. Thus, examples such as the quantum-classical Liouville approaches,[30] the exact-factorization-based mixed

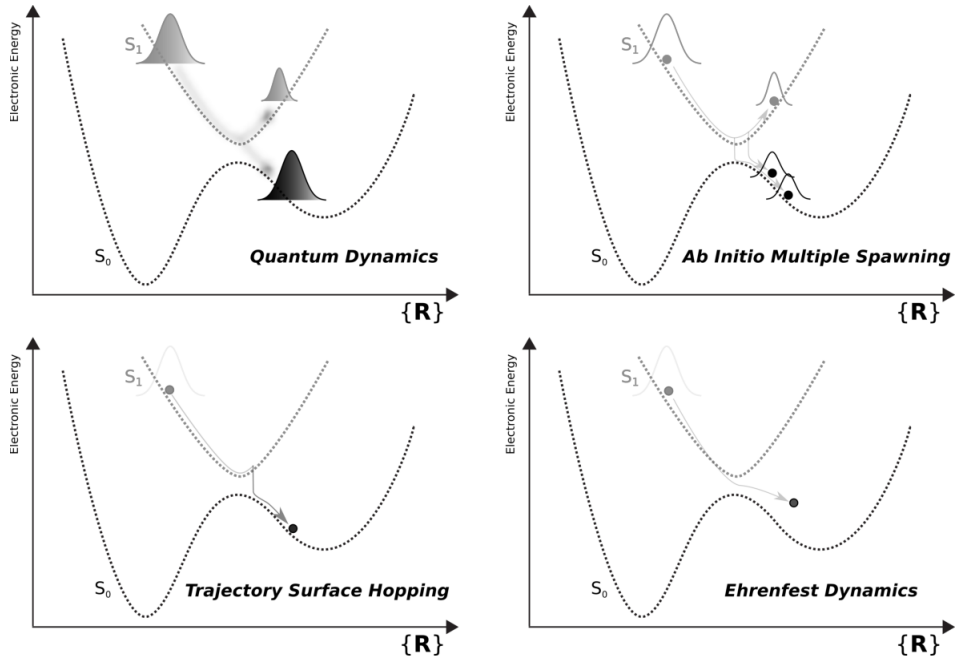

Fig. 1.3: Schematic representation of different methods for non-adiabatic molecular dynamics. Reprinted with permission from Curchod, B.; Martínez, T. *Chem. Rev.* **2018**, 118, 3305–3336. Copyright 2018 American Chemical Society.

quantum-classical algorithms[31] and Bohmian dynamics[32] belong to the bigger group of nonadiabatic molecular dynamics.

The first part of this thesis, **Chapter 2**, is focused on setting the theoretical framework for this research study. Beginning with the Schrödinger equation that constitutes the key equation to simulate the photo-activated processes from first principles, along with detailed explanation of the adiabatic and diabatic representation and the Born-Oppenheimer approximation. Finally, the concept of the potential energy surfaces is presented together with the importance of conical intersections.

In **Chapter 3**, the different schemes for electronic and nuclear dynamics related to the scope of this research are described. Since the core subject of this chapter is the DD-vMCG method, it will be mainly employed and developed.

Further, **Chapter 4** includes all the methodological updates to the DD-vMCG method which deal with the database, and the efficiency and accuracy bottlenecks.

Firstly, a new, efficient parallel algorithm to control the DD-vMCG database of quantum chemistry points is described along with improvements to the Shepard interpolation scheme. Next, benchmark calculations on the butatriene cation, allene radical cation and formamide including all degrees of freedom are presented.

The application of the developed efficient algorithm for direct dynamics is presented in **Chapter 5** where the photodissociation dynamics of phenol including all degrees of freedom is examined. A detailed comparison with the existing 4-state model for the potential energy surfaces along with new insights into the excited state photochemistry of phenol by including five excited states are presented. Including more excited states than the target ones, has been shown here to be vital in order to successfully unravel the non-adiabatic photodissociation of phenol to the phenoxyl radical and hydrogen atom. All the findings are compared and linked to each other and to the existing literature.

In **Chapter 6**, the use of Gaussian process regression to fit on-the-fly the potential energy surfaces of DD-vMCG is introduced along with its implementation focusing on the optimisation of the kernel hyperparameters. This approach enables the exact and efficient analytic calculation of Hamiltonian matrix elements and consequently removes the accuracy errors of the local harmonic approximation approach. Test calculations on the multiple-state non-adiabatic dynamics of the ozone molecule are also presented.

At the closing chapter, **Chapter 7**, a summary of the main results in this thesis is presented along with future prospects based on the lines of research that arose from this research study.

Chapter 2

Theory

2.1 Introduction

A critical review of the literature associated with the subject area of this research study will be presented in this chapter. The theories and mathematical principles of relevance to computational quantum chemistry will be identified and analysed in depth.

In this chapter, an effort to build an understanding regarding the different forms of the fundamental Schrödinger equation and the construction of the Hamiltonian, subject to the system under examination, is made. The Born-Oppenheimer Approximation (BOA) will be then presented and cases where this approximation breaks down will be also discussed. The importance of understanding and visualizing the relationship between molecular geometry and potential energy will be presented. Finally, the time evolution and the role of conical intersections (CoIs) in many photochemical transformations will be introduced.

2.2 The Schrödinger Equation

The Schrödinger equation[12] is the fundamental equation of non-relativistic quantum mechanics. It describes the temporal evolution of a state of a physical system.

The time-dependent Schrödinger equation is written as

$$i\hbar\frac{\partial}{\partial t}\Psi\left(\boldsymbol{r},t\right)=\hat{H}\Psi\left(\boldsymbol{r},t\right) \tag{2.1}$$

where $i=\sqrt{-1}$, $\hbar$ is equal to $\frac{h}{2\pi}$ and denotes the reduced Planck constant, $\frac{\partial}{\partial t}$ represents the partial derivative with respect to time, Ψ is the time-dependent wavefunction , $\boldsymbol{r}$ is the position vector, t is time and $\hat{H}$ is the Hamiltonian which in its time independent form contains the following kinetic and potential energy terms

$$\hat{H}=-\frac{\hbar^2}{2m}\nabla^2+V\left(\boldsymbol{r}\right) \tag{2.2}$$

where m is the mass for a particle, ∇^2 is the Laplacian and $V\left(\boldsymbol{r}\right)$ is the time-independent potential energy.

Eq. 2.1 contains the derivative of Ψ with respect to time which means that if Ψ is known at time $t=0$ then it can be calculated at some later time t. The physical significance of the wavefunction is that $\left|\Psi\right|^2 d\tau=\Psi^*\Psi$ is the probability density, where Ψ^* is the complex conjugate of Ψ. In essence, the probability of finding a particle in the volume element $d\tau$ is proportional to the square of the wavefunction. For a normalised wavefunction the integral of the probability over all space takes the value of unity

$$\int_{-\infty}^{\infty}\Psi^*\Psi d\tau=1 \tag{2.3}$$

The time-independent Schrödinger equation can be derived from the time-dependent form. As long as the potential energy, V, is time-independent the time and space dependent parts of Eq. 2.1 can be separated and the wavefunction written as

$$\Psi\left(\boldsymbol{r},t\right)=f\left(t\right)\psi\left(\boldsymbol{r}\right) \tag{2.4}$$

Substituting this into Eq. 2.1 gives

$$i\hbar\frac{\partial f\left(t\right)}{\partial t}\psi\left(\boldsymbol{r}\right)=-\frac{\hbar^2}{2m}\nabla^2 f\left(t\right)\psi\left(\boldsymbol{r}\right)+V\left(\boldsymbol{r}\right)f\left(t\right)\psi\left(\boldsymbol{r}\right) \tag{2.5}$$

and then dividing both sides by $f(t)\,\psi(\boldsymbol{r})$ gives

$$i\hbar\frac{1}{f(t)}\frac{\partial f(t)}{\partial t} = -\frac{\hbar^2}{2m}\frac{1}{\psi(\boldsymbol{r})}\frac{d^2\psi(\boldsymbol{r})}{dr^2} + V(\boldsymbol{r}) \tag{2.6}$$

The right hand side of Eq. 2.6 is a function of $\boldsymbol{r}$ only and is independent of a change in t, whereas the left hand side is a function of t only and is independent of a change in $\boldsymbol{r}$. As the two sides are equal to one another there has to be some value which each side equates to that does not depend either on $\boldsymbol{r}$ or on t and must, therefore, be a constant. This constant has units of energy and is labelled as E.

Equating first the left hand side of Eq. 2.6 to E and then the right hand side generates two separate equations

$$i\hbar\frac{\partial f(t)}{\partial t} = Ef(t) \tag{2.7}$$

$$-\frac{\hbar^2}{2m}\frac{d^2\psi(\boldsymbol{r})}{dr^2} + V(\boldsymbol{r})\,\psi(\boldsymbol{r}) = E\psi(\boldsymbol{r}) \tag{2.8}$$

Eq. 2.7 has the solution

$$f(t) = e^{-iEt/\hbar} \tag{2.9}$$

and the complete wavefunction, $\Psi = \psi f$ can be written

$$\Psi(\boldsymbol{r}, t) = \psi(\boldsymbol{r})\, e^{-iEt/\hbar} \tag{2.10}$$

Eq. 2.8 is the time-independent Schrödinger (TISE) equation with a general form

$$\hat{H}\psi = E\psi \tag{2.11}$$

Consequently, it can be said that the TISE is an eigenvalue equation which describes the stationary states of, or definite energy solutions to, the TDSE. Contextually these may also be referred to as energy eigenstates or as orbitals.[22]

2.3 The Hamiltonian

In quantum theory observable quantities are described by operators.[22] As previously defined, the energy observable is expressed by an operator named the Hamiltonian operator, $\hat{H}$. For the systems that we shall consider, the classical Hamiltonian is just the sum of the kinetic and potential energies, T and V respectively, of the system[33–35]

$$H = T + V \tag{2.12}$$

The relation connecting the operators for momentum, energy and position is assumed to be similar to the one between the classical parameters. Particularly, the Hamiltonian operator of a single particle in one dimension with mass m and a $V(\boldsymbol{r})$ potential energy of the system is assumed to be[36,37]

$$\hat{H} = \frac{\hat{p}^2}{2m} + V(\hat{r}) \tag{2.13}$$

Taking into consideration that momentum and position observables are expressed in quantum mechanics by operators and extending the Schrödinger Hamiltonian further into 3 dimensions, Eq. 2.13 of the Hamiltonian operator becomes

$$\begin{aligned} \hat{H} &= -\frac{\hbar^2}{2m}\nabla^2 + V(\mathbf{r}) \\ &= -\frac{\hbar^2}{2m}\left(\frac{\partial^2}{\partial x^2} + \frac{\partial^2}{\partial y^2} + \frac{\partial^2}{\partial z^2}\right) + V(x, y, z, t) \end{aligned} \tag{2.14}$$

which is linear and Hermitian. In the case where there are many particles Eq. 2.14 takes the following form

$$\hat{H} = \sum_{i=1}^{N}\left(-\frac{\hbar^2}{2m_i}\nabla_i^2 + V(\boldsymbol{r}_i, t)\right) = \sum_{i=1}^{N}\hat{h}_i \tag{2.15}$$

where the total Hamiltonian is the sum of the Hamiltonians for each particle and m_i is the mass of the i^{th} particle and ∇_i^2 is the Laplacian operator containing the coordinates of the i^{th} particle.

Finally, the dual role of the Hamiltonian operator, $\hat{H}$, in quantum mechanics ought to be emphasized.[38] Firstly, the Hamiltonian operator describes the energy

observable; hence the energy expectation value for a particle with wavefunction $\Psi(\mathbf{r}, t)$ at time t is

$$\langle E \rangle = \int \Psi^*(\mathbf{r}, t)\, \hat{H} \Psi(\mathbf{r}, t)\, d^3\mathbf{r} \tag{2.16}$$

Secondly, the time evolution of the wavefunction is determined by the Hamiltonian operator since the Schrödinger equation for a particle moving in the three-dimensional potential energy field $V(\mathbf{r})$ has the following form

$$\hat{H}\Psi = \left[-\frac{\hbar^2}{2m}\nabla^2 + V(\mathbf{r}) \right] \Psi = i\hbar \frac{\partial \Psi}{\partial t} \tag{2.17}$$

Thus, a fundamental connection between energy and time exists in quantum mechanics.

2.4 Born-Oppenheimer Approximation

It is difficult to solve the Schrödinger Eq. 2.1, because it contains the enormous number of variables of the many-body wavefunction, Ψ. Hence, a system has $3n + 3N$ degrees of freedom, three spatial coordinates for each electron and for each nucleus when consisting of n electrons and N nuclei. Born and Oppenheimer demonstrated in 1927[11] that to a very good approximation the nuclei in a molecule are stationary with respect to electrons. Considering that electrons are much lighter than the nuclei (nuclei are about 10^3 to 10^5 times heavier compared to electrons), their motion will be much quicker, resulting in much smaller characteristic time scales of processes involving the electrons. Consequently, it is assumed that when a nucleus moves the electrons immediately reorder themselves around it. The electronic wavefunctions can be constructed by assuming that the nuclei are fixed in space. The nuclear coordinates are then just parameters in the electronic Schrödinger equation and the nuclear and electronic motions are thus said to be decoupled. By separating the kinetic energy and potential terms for the

nuclei and electrons the Hamiltonian operator takes the following form

$$\hat{H} = \hat{T}_N + \hat{T}_e + \hat{V}_{eN} + \hat{V}_{ee} + \hat{V}_{NN} \tag{2.18}$$

where $\hat{T}_N$ and $\hat{T}_e$ are the kinetic energy operators for the nuclei and electrons respectively, and $\hat{V}_{eN}$, $\hat{V}_{ee}$ and $\hat{V}_{NN}$ the potential energy operators for the nuclear-electron, electron-electron and nuclear-nuclear interactions accordingly. The full form of the previous equation (2.18) for the Hamiltonian operator is

$$\begin{aligned} \hat{H} = &- \frac{\hbar^2}{2} \sum_{\alpha} \frac{1}{m_\alpha} \nabla_\alpha^2 - \frac{\hbar^2}{2m_e} \sum_i \nabla_i^2 \\ &- \sum_\alpha \sum_i \frac{Z_\alpha e^2}{r_{i\alpha}} + \sum_\alpha \sum_{\beta>\alpha} \frac{Z_\alpha Z_\beta e^2}{r_{\alpha\beta}} + \sum_j \sum_{i>j} \frac{e^2}{r_{ij}} \end{aligned} \tag{2.19}$$

where m refers to mass, r to distance, Z to atomic number and the subscripts α, β and i, j refer to nuclei and electrons respectively.

The large number of terms in Eq. 2.19 clearly shows that obtaining an analytical solution of the Schrödinger equation is impossible for anything apart from hydrogen molecule. However, this can be addressed by taking advantage of the large mass difference between the nuclei and the electrons which implies that the position of the electrons changes instantaneously along with any change in the nuclear geometry. Thus, the nuclei can be considered to be fixed and the Schrödinger equation may be then solved only for the electrons at a fixed nuclear geometry. The aforementioned concept is demonstrated by expressing the full wavefunction as a product of the electronic ψ wavefunction and the nuclear wavefunction χ

$$\Psi(r;R) = \psi(r;R)\chi(R) \tag{2.20}$$

Substituting Eq. 2.20 and 2.18 in Eq. 2.11

$$[\hat{T}_N(R)+\hat{T}_e(r)+\hat{V}_{eN}(r,R)+\hat{V}_{ee}(r)+\hat{V}_{NN}(R)]\psi(r;R)\chi(R) = E\psi(r;R)\chi(R) \tag{2.21}$$

Considering that T_e is independent of the nuclear position the following equation can be written

$$T_e\psi\chi = \chi T_e\psi \tag{2.22}$$

However, a similar formula for the nuclear kinetic energy operator cannot be written since it depends on the nuclear position. For this case, the product rule is employed

$$\frac{\partial^2}{\partial R^2}\psi\chi = \psi\frac{\partial^2}{\partial R^2}\chi + 2\frac{\partial}{\partial R}\psi\frac{\partial}{\partial R}\chi + \chi\frac{\partial^2}{\partial R^2}\psi \tag{2.23}$$

The Schrödinger equation now has the form

$$H\psi\chi = T_e\psi\chi + V_{eN}\psi\chi + V_{ee}\psi\chi + V_{NN}\psi\chi + W = E\psi\chi \tag{2.24}$$

where W has the following form

$$W = -\sum_a \frac{\hbar^2}{2m_a}(\psi\frac{\partial^2}{\partial R^2}\chi + 2\frac{\partial}{\partial R}\psi\frac{\partial}{\partial R}\chi + \chi\frac{\partial^2}{\partial R^2}\psi) \tag{2.25}$$

As discussed at the beginning of this section, in the Born-Oppenheimer approximation the nuclear masses (m_a) are assumed to be relatively large thus Eq. 2.25 is considered to be almost zero and all the elements inside this expression are neglected. This equation acts as a limit for BOA as when it can no longer be ignored, there is coupling between the electronic and nuclear motion and very important and interesting quantum dynamical phenomena arise. Consequently, Eq. 2.24 can be rewritten as

$$\psi T_N\chi + (T_e\psi + V_{eN}\psi + V_{ee}\psi + V_{NN}\psi)\chi = E\psi\chi \tag{2.26}$$

Moreover, by multiplying Eq. 2.24 on the left by ψ^* and integrating over electronic coordinates the nuclear Schrödinger equation is yielded

$$(T_N + V)\chi = E\chi \tag{2.27}$$

where T_N is the kinetic energy of the nuclei and V is the potential as a result of the electronic motion.

2.5 Adiabatic Representation

The adiabatic representation is based on the Born-Oppenheimer approximation. This is a fundamental approach and many different research techniques such as spectroscopy heavily rely on the adiabatic picture. Moving outside the scope of the BOA, the exact solution in the adiabatic basis can be written as

$$\Psi\left(r;R\right)=\sum_{n=0}^{\infty}\psi_{n}\left(r;R\right)\chi_{n}\left(R\right) \tag{2.28}$$

For simplicity the former sum includes only the bound electronic states, however for completeness an integral over the unbound states should be included. Substituting the ansatz 2.28 in Eq. 2.11 and with the Hamiltonian (Eq. 2.18), and projecting from the left with $\psi_m(r;R)$ results in

$$\sum_{n}\left\{(T_N+E_n(R)+V_N(R))\delta_{nm}+2T^{(1)}_{mn}(R)\nabla+T^{(2)}_{mn}(R)\right\}\chi_n(R)=E\chi_m(R) \tag{2.29}$$

The number of $T^{(1)}_{mn}$ vector components equals the number of degrees of freedom (DOFs) and $T^{(2)}_{mn}$ is a scalar

$$T^{(1)}_{mn}(R)=\langle\psi_m\mid\nabla\psi_n\rangle \tag{2.30}$$

$$T^{(2)}_{mn}(R)=\left\langle\psi_m\mid\nabla^2\psi_n\right\rangle \tag{2.31}$$

When the electronic and nuclear coupling is small, only the diagonal elements of Eq. 2.29 are kept. Thus, the Schrödinger equation as expressed in Eq. 2.27 with an additional small but non-vanishing $T^{(2)}_{nn}$ becomes

$$\sum_{n}(T_N+E_n+V_N+T^{(2)}_{nn})\chi_n=E\chi_n \tag{2.32}$$

2.6 Non-Adiabatic Corrections

In the event of large non-adiabatic couplings the off-diagonal elements of Eq. 2.29 can no longer be ignored and can be very complex to calculate. To this end, Eq. 2.29 can be simplified so that the wavefunction is written as

$$(\hat{T}_N + V_i) \mid \Psi_i\rangle - \sum_j \Lambda_{ij} \mid \Psi_i\rangle = i\hbar \frac{\partial}{\partial t} \mid \Psi_i\rangle \tag{2.33}$$

which is a time-dependent form of the Schrödinger equation and j and i denote the electronic states and Λ_{ij} is the non-adiabatic coupling matrix which can be expressed as

$$\Lambda_{ij} = \frac{1}{2M}(G_{ij} + 2F_{ij}\nabla) \tag{2.34}$$

where G_{ij} is a matrix of numbers which can be expressed as

$$G_{ij} = \langle \Psi_i | \nabla^2 \Psi_j \rangle = \left\langle \Psi_i | \frac{\partial^2}{\partial R^2} \Psi_j \right\rangle \tag{2.35}$$

and F_{ij} is the non-adiabatic coupling vector.

$$F_{ij} = \langle \Psi_i | \nabla \Psi_j \rangle = \left\langle \Psi_i | \frac{\partial}{\partial R} \Phi_j \right\rangle = \frac{1}{E_j - E_i} \left\langle \Psi_i | \frac{\partial \hat{H}_{el}}{\partial R} \Psi_j \right\rangle \tag{2.36}$$

Hence, F_{ij} inversely depends on the energy gap between the 2 states, in such a way that as the gap becomes larger the coupling decreases whereas if the two states become degenerate the non-adiabatic coupling vector will become infinite.

Thus, solving Eq. 2.33 implies that the first, $\frac{\partial}{\partial R}$, and second, $\frac{\partial^2}{\partial R^2}$, derivatives of electronic wavefunctions must be solved. In the adiabatic representation the coupling can be neglected and the derivatives are small resulting in the following equation

$$[\hat{T}_N + V_i - E]\chi_i = 0 \tag{2.37}$$

where there is no coupling and V_i is known as the potential energy surface, also called the potential because it is the potential energy in the dynamical equation of nuclear motion, being one of the most important concepts in physical chemistry.

More detailed description of the adiabatic approximation, such as, its validity, its generalization, the problem of deriving corrections to it and many other aspects are thoroughly discussed in the literature.[15,39–45]

2.7 Vibronic Coupling and Diabatic Representation

During ultrafast processes, such as those pertaining to the photochemistry of polyatomic molecules, the vibronic coupling can become significant when a molecule reaches a region where PESs are close and separating the electronic and nuclear motions becomes impossible. Hence, the BOA breaks down. Within the adiabatic representation the difficulty arises when trying to calculate the first and second derivatives in the coupling matrix of the electronic wavefunctions. In order for these derivatives to be as small as possible or even absent, the electronic basis functions should not depend on the nuclear coordinates, thereby there is no change in the electronic wavefunction with nuclear geometry. These electronic basis functions are known as the *diabatic basis*. For systems with significant non-adiabatic effects, the diabatic representation is the obvious choice as it eliminates singularities which arise when $E_j - E_i \rightarrow 0$ in Eq. 2.36 resulting in smooth and simple potential energy surfaces.[46]

Accordingly, the Schrödinger equation in the diabatic basis can be expressed as

$$\tilde{T}_N \mid \Psi_i\rangle + \sum_j W_{ij} \mid \Psi_j\rangle = i\hbar\frac{\partial}{\partial t} \mid \chi_i\rangle \tag{2.38}$$

where W_{ij} denotes the potential matrix and has the following form

$$W_{ij} = \left\langle \Phi_i \left| \tilde{H}_{el} \right| \Phi_j \right\rangle \tag{2.39}$$

Commonly a unitary transformation of the adiabatic states, ϕ, is employed to determine the diabatic states, Φ. The orthogonal matrix, S, is used to transform

the operator from adiabatic to diabatic

$$(|\Phi_1\rangle|\,\Phi_2\rangle) = S\,(|\phi_1\rangle|\,\phi_2\rangle) \tag{2.40}$$

where Φ and ϕ denote the diabatic and adiabatic electronic wavefunctions respectively. More specifically, the transformation at each fixed geometry for a two-state system is expressed as

$$\begin{pmatrix}\Phi_1\\ \Phi_2\end{pmatrix} = \begin{pmatrix}\cos a & \sin a\\ -\sin a & \cos a\end{pmatrix}\begin{pmatrix}\phi_1\\ \phi_2\end{pmatrix} \tag{2.41}$$

where a is the mixing angle between the two adiabatic states depending on the $\boldsymbol{r}$ and $\boldsymbol{R}$ coordinates. The diagonal terms of Eq. 2.41 have the following form

$$W_{11} = \left\langle \Phi_1 \left| \hat{H}_{el} \right| \Phi_1 \right\rangle = V_1 \cos^2 a + V_2 \sin^2 a \tag{2.42}$$

$$W_{22} = \left\langle \Phi_2 \left| \hat{H}_{el} \right| \Phi_2 \right\rangle = V_1 \sin^2 a + V_2 \cos^2 a \tag{2.43}$$

and the off-diagonal terms

$$W_{12} = \left\langle \Phi_1 \left| \hat{H}_{el} \right| \Phi_2 \right\rangle = (V_1 - V_2) \cos a \sin a \tag{2.44}$$

where for this two state system $V_{1,2}$ are the adiabatic potential energies, W_{11} and W_{22} are the diabatic potential energies and $W_{12} = W_{21}$ represent the coupling between these two states.

The two criteria for selecting the mixing angle, a, are firstly obtaining smooth surfaces and secondly that the following condition is true[47]

$$\nabla \mathbf{S} = -\mathbf{F}\mathbf{S} \tag{2.45}$$

where F as earlier described is the non-adiabatic coupling vector. A point where the diabatic and adiabatic surfaces are the same is selected to initially define the **S** matrix, which in most cases is the Frank-Condon point. According to the Frank-Condon principle, a vertical electronic transition from the minimum of the PES of

the ground state occurs without changes in the positions and momentum of the nuclei. The point of intersection,at which a vertical line cuts through the PES of the excited electronic state, is called the Franck–Condon point, and the resulting state is a Franck–Condon (excited) state with the Franck–Condon geometry, which is the equilibrium geometry of the former ground state. The diabatisation scheme is defined by the solutions to the differential equation.

A visual example of a two state molecule such as butatriene is depicted in Fig. 2.1 where it can be observed that the diabatic representation has smoother PESs compared to the adiabatic one and the conical crossing is eliminated.

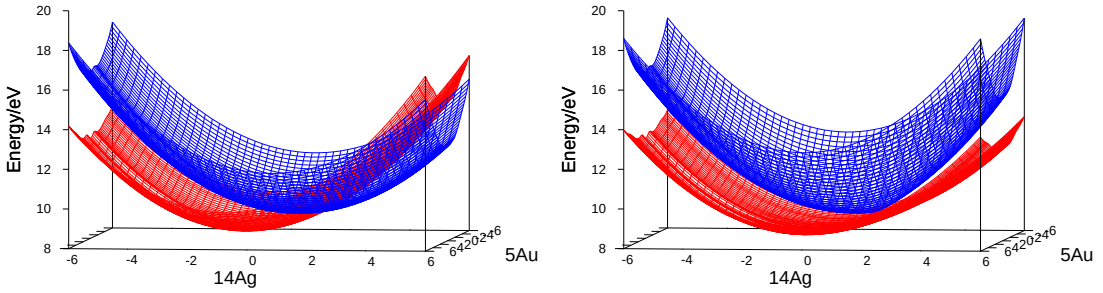

(a) (b)

Fig. 2.1: The diabatic (a) and adiabatic (b) potential energy surfaces of the butatriene molecule along the C-C symmetric stretching mode, $14Ag$, and the CH_2 twisting mode, $5Au$.

2.8 Potential Energy Surfaces

Potential energy surfaces are essential in understanding and visualizing the relationship among molecular geometry and potential energy. The potential energy surface, which can be a function obtained by fitting to the *ab initio* energies, should describe the molecular energy as the internuclear distances change. *Ab initio* energies used to map a potential energy surface can be gathered by solving the electronic problem and obtaining the electronic wavefunction $\psi(\boldsymbol{R}, \boldsymbol{r})$. Methods aimed at solving this problem are broadly referred to as electronic structure

calculations[48] and important improvements have been made[49] to allow an accurate *ab initio* evaluation of the molecular energy within the Born-Oppenheimer approximation.[11]

The most important features of PESs for discussing chemical reactions are the stationary points, which on a PES are points at which the target surface is flat, i.e. parallel to a horizontal line corresponding to one geometric parameter (or to the plane corresponding to two geometric parameters, or to the hyperplane corresponding to more than two geometric parameters). A marble placed on a stationary point will remain balanced, i.e. stationary. At any other point on a potential surface the marble will roll toward a region of lower potential energy. Mathematically, a stationary point is one at which the first derivative of the potential energy with respect to each geometric parameter is zero[50–52]

$$\frac{\partial V}{\partial q_1} = \frac{\partial V}{\partial q_2} = ... = 0 \tag{2.46}$$

These stationary points can be distinguished by the second derivatives of the potential energy in terms of the internal coordinates, according to the number of positive, negative and zero eigenvalues of the (3N-6) x (3N-6) matrix, we can get:

For a minimum, along all the reaction coordinate q

$$\frac{\partial^2 V}{\partial q^2} > 0 \tag{2.47}$$

For a transition state, for all q

$$\frac{\partial^2 V}{\partial q^2} > 0 \tag{2.48}$$

except along the reaction coordinate where

$$\frac{\partial^2 V}{\partial q^2} < 0 \tag{2.49}$$

Thus, if all of the eigenvalues of the Hessian matrix are positive, the stationary point is a minimum with all real frequencies, which occupies the lowest-energy

point in the region of the PES, corresponding to reactants, products or intermediates.[53] The Hessian matrix is a square matrix of second-order partial derivatives of a scalar-valued function, or scalar field. It describes the local curvature of a function of many variables. If the minimum is the lowest-energy minimum on the entire PES, it is called a global minimum. The transition state linking the two minima represents a maximum along the direction of the intrinsic reaction coordinate, yet along the other directions it is a minimum. This is typical for a saddle-shaped surface, and the transition state is known as saddle point. The former main features of PESs are visualised in Fig. 2.2.

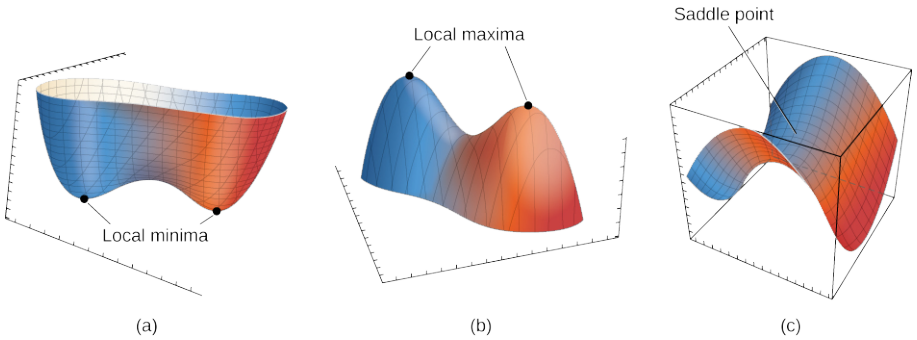

Fig. 2.2: Schematic two-dimensional representation of (a) a minimum, (b) a maximum stationary point and (c) a sadle point.

A transition state is a first order saddle point, with only one negative eigenvalue. These are of particular interest in chemical kinetics because they lie on the paths between points on the surface identified with reactant and points on the surface identified with product species, offering a practical way of tracing those paths in a steepest descent manner. Some PESs have points where the second derivative of energy with respect to more than one coordinate is negative; these are higher-order saddle points; for instance, a second-order saddle point is a point on the PES that is a maximum along two paths connecting stationary points, hence of little relevance in kinetics.[46,54,55] The location of a stationary point on the PES can be achieved by many different methods see Refs.[56–59]

2.9 The Role of Conical Intersections

Initially, a photochemical reaction for any excited molecule was conceptually defined as a decay occurring at an excited state energy minimum with a simultaneous avoided crossing region between the ground state and the excited state potential energy surfaces.[60] Nevertheless, Michl,[61] Teller[62] and Zimmerman[63] presented the *photochemical funnels* concept. In the research work of the aforementioned authors, it was primarily proposed that some photoproducts might be produced by nonradioactive decay of the excited state molecule via a degeneracy - a crossing point - between the ground and the excited state potential energy surfaces, instead of an avoided crossing.

These degenerate points are generally known as *conical intersections*[50] (CoIs) or *conical crossings*.[62] Even though CoIs were believed to be an exception instead of the rule, over two decades of computational Quantum Chemistry research studies[64–66] have confirmed that they are very common in polyatomic systems. Such crossings give very effective funnels for radiationless deactivation such as internal conversion.

Given the central role of these CoIs in many photochemical transformations, we need to explore the conditions for their existence. To this end, let $\mathbf{H}^{el}$ be an electronic Hamiltonian, via which Φ_1 and Φ_2 electronic states are interacting.

$$\mathbf{H}^{el} = \begin{pmatrix} H_{11}(R) & H_{12}(R) \\ H_{21}(R) & H_{22}(R) \end{pmatrix} \tag{2.50}$$

with

$$H_{ij} = \left\langle \Phi_i \left| H^{el} \right| \Phi_j \right\rangle \tag{2.51}$$

By diagonalizing the two-by-two matrix operator, we obtain the adiabatic potentials:

$$V_{\pm} = \bar{H} \pm \sqrt{\Delta H^2 + H_{12}^2} \tag{2.52}$$

where $\bar{H} = (H_{11} + H_{22})/2$ and $\Delta H = (H_{11} - H_{22})/2$. Finally, the requirements for two adiabatic potentials to cross, are the following two independent conditions:

$$H_{11}(R) = H_{22}(R) \tag{2.53}$$

$$H_{12}(R) = 0 \tag{2.54}$$

If the wavefuctions of two electronic states have the same symmetry, the $H_{12}(R)$ will be zero for any nuclear coordinates. In this case there might be a point or points where we have degeneracy and these points are CoIs[67] or avoiding crossings. On the other hand, if the wavefuctions of two electronic states have different symmetries, their PESs will always cross. Von Neumann and Wiger[68] established these two requirements which are known as the *non-crossing rule* for degeneracy as in a one-dimensional system the conditions cannot be both fulfilled and the surfaces do not cross.

Finally, although the role of conical intersections in photochemical reactions cannot be easily ascertained experimentally, it is now computationally validated.[69–71] A particular conical intersection, the symmetry-induced crossings in Jahn-Teller active molecules, is however an exception, since it has long been investigated by spectroscopic techniques.[72] Laser-induced fluorescence from a non-degenerate excited electronic state to a degenerate one[73] and photoelectron spectroscopy from a neutral closed-shell species to an open-shell Jahn-Teller active species[74] are some of the most commonly used techniques.

Chapter 3

Methodology

3.1 Introduction

Following the theories and hypotheses described in Chapter 2, this Chapter focuses on the different electronic structure and nuclear dynamics methods related to the scope of this research study. Initially, Section 3.2 outlines the various electronic structure methods, known as *ab initio* methods,[26,75] employed to solve the time-independent Schrödinger equation within the limits of the Born-Oppenheimer approximation (BOA). Subsequently, different existing nuclear dynamics methods that can be applied to solve the time-dependent Schrödinger equation and thus cases where the Born-Oppenheimer approximation breaks down are extensively presented in Section 3.3. The main focus of this chapter is to build an understanding regarding the direct dynamics variational multi-configurational Gaussian (DD-vMCG) method which is the main method used and developed during this study.

3.2 Electronic Structure

A wide range of different *ab initio* methods exist where all the information is obtained from theoretical calculations without using any experimental data. The most simple and well-known electronic structure method is Hartree-Fock,[76,77] a mean-field method where a single determinant is employed to describe the wave-

function. A "nontrivial" solution exists only if the determinant is equal to zero and this determinant is known as secular determinant. Hartree-Fock theory neglects electron correlation since the electron-electron repulsion is treated as an average. HF accounts for around 99% of the exact energy of a molecule in its ground state as ground states are usually very well described by a single electronic configuration. However, to describe any process involving electronic excited states which are multi-configurational, such as those involved in photodissociation or converted via a conical intersection, more advanced methods which are briefly discussed in section 3.2.3 are required.

3.2.1 Hartree-Fock Method

The Hartree-Fock method is the most commonly applied theory to solve the electronic time-independent Schrödinger equation and has been often used as a starting stage in a plethora of *ab initio* quantum chemistry methods. According to this method, the electron-electron repulsion is averagely treated since every electron is assumed to move in an average potential based on the other electrons and the nuclei. Additionally, in the Hartree-Fock method a single particle function can be used to describe the motion of each electron.

Taking into consideration the Hamiltonian operator, Eq. 2.19 from Chapter 2, the time independent electronic Schrödinger equation can be expressed as follows

$$[\hat{T}_e(\boldsymbol{r}) + \hat{V}_{ne}(\boldsymbol{r}, \boldsymbol{R}) + \hat{V}_{nn}(\boldsymbol{R}) + \hat{V}_{ee}(\boldsymbol{r})]\Psi(\boldsymbol{r}, \boldsymbol{R}) = E_e(\boldsymbol{R})\Psi(\boldsymbol{r}; \boldsymbol{R}) \tag{3.1}$$

Within the Born-Oppenheimer approximation, a set of electronic wavefuctions exists for each fixed nuclear geometry that satisfies the following equation

$$\hat{H}_e\Psi_e = E_e\Psi_e \tag{3.2}$$

The kinetic energy of the electrons and the electron-nuclear attraction are a sum of different terms, each one relying only on the coordinates of one electron

while the electron-electron repulsion relies on two. At a given fixed geometry, the nuclear-nuclear repulsion is considered as a constant variable since it is independent of the electronic coordinates.

$$\boldsymbol{T}_e = -\sum_{i=1}^{N} \frac{1}{2}\nabla_i^2 \tag{3.3}$$

$$\boldsymbol{V}_{ne} = -\sum_{i=1}^{N}\sum_{a} \frac{Z_a}{|\boldsymbol{R}_a - \boldsymbol{r}_i|} \tag{3.4}$$

$$\boldsymbol{V}_{ee} = \sum_{i=1}^{N}\sum_{ji}^{N} \frac{1}{|\boldsymbol{r}_i - \boldsymbol{r}_j|} \tag{3.5}$$

$$\boldsymbol{V}_{nn} = \sum_{a}\sum_{ba} \frac{Z_a}{Z_b} |\boldsymbol{R}_a - \boldsymbol{R}_b| \tag{3.6}$$

Based on the former terms, the following expressions can be used for the one- and two-electron operators

$$\boldsymbol{h}_i = -\frac{1}{2}\nabla_i^2 - \sum_{a} \frac{Z_a}{|\boldsymbol{R}_a - \boldsymbol{r}_i|} \tag{3.7}$$

$$\boldsymbol{g}_{ij} = \frac{1}{|\boldsymbol{r}_i - \boldsymbol{r}_j|} \tag{3.8}$$

$$\boldsymbol{H}_e = \sum_{i=1}^{N} \boldsymbol{h}_i + \sum_{i=1}^{N}\sum_{j>1}^{N} \boldsymbol{g}_{ij} + V_{nn} \tag{3.9}$$

where $\boldsymbol{h}_i$ denotes the motion of the i electron and $\boldsymbol{g}_{ij}$ describes the two-electron operator. Ignoring the $\boldsymbol{g}_{ij}$ coupling, Eq. 3.2 can be written as the sum of the one-electron terms

$$h_i\varphi_i = \epsilon_i\varphi_i \tag{3.10}$$

- where ϵ_i denotes the energy of electron i.

A product of one-electron wavefunctions can be employed, known as a Hartree product in order to solve Eq. 3.10

$$\Psi_e = \varphi_1^{(1)}\varphi_2^{(2)}\cdots \tag{3.11}$$

By considering the Pauli exclusion principle[78] for fermions and the spin of the electrons, the total wavefuction must, however, be written as a Slater determinant[79] and the one-electron wavefunctions can be expressed as spin orbitals, $\phi_\alpha(i)$. A fermion is any subatomic particle that follows Fermi-Dirac statistics and complies with the Pauli exclusion principle. The determinant takes the following form for N spin orbitals and N electrons

$$\Phi = \frac{1}{\sqrt{N!}} \begin{vmatrix} \phi_1(1) & \phi_2(1) & ... & \phi_N(1) \\ \phi_1(2) & \phi_2(2) & ... & \phi_N(2) \\ . & . & . & . \\ . & . & . & . \\ . & . & . & . \\ \phi_1(N) & \phi_2(N) & ... & \phi_N(N) \end{vmatrix} \tag{3.12}$$

where

$$\langle \phi_i | \phi_j \rangle = \delta_{ij} \tag{3.13}$$

Eq. 3.12 can be written in a compact notation as follows

$$\Phi = |\phi_1(1)\phi_2(2)...\phi_N(N)\rangle \tag{3.14}$$

The time-independent Schrödinger equation is now solved for the determinant ϕ by employing the variational principle with Φ being a trial wavefunction. Within the variational principle, any trial wavefunction has a higher energy compared to the true energy. As a result, the Hartree-Fock equations are derived.

3.2.2 Basis Sets

Expressing the molecular orbitals which are unknown functions in the form of a linear combination of atomic orbitals is a standard practice when *ab initio* methods are employed

$$\phi_i = \sum c_{ia}\chi_a \tag{3.15}$$

where c are the coefficients and χ is a sum of known functions such as Gaussian functions. To overcome the obstacle of the unknown functions, the molecular orbitals, a set of known functions, called the basis set, is introduced. The level of accuracy of the employed restricted basis set relies on how well the unknown function is represented by the basis function and also on the size of the basis set. A large basis set means more Gaussian or Slater type orbitals are employed to describe each molecular orbital and thus a better description of it is achieved.

One of the most commonly used functions in *ab initio* methods are the Slater Type Orbitals[21,80–82] which have the following form

$$\chi_{\zeta,n,m}(r,\theta,\varphi) = NY_{l,m}(\theta,\xi)r^{n-1}e^{-\zeta r} \tag{3.16}$$

where N denotes the normalisation constant, $Y_{l,m}$ are spherical harmonic functions, r indicates the distance between the electron and the atomic nucleus and lastly ζ denotes the orbital exponent related to the nucleus effective charge.

Another important known function are the Gaussian Type Orbitals[21,80,82] and can be expressed as a function of cartesian, Eq. 3.17, or polar, Eq. 3.18 coordinates

$$\chi_{\zeta,l_x,l_y,l_z}(x,y,z) = Nx^{l_x}, y^{l_y}, z^{l_z}e^{-\zeta r^2} \tag{3.17}$$

$$\chi_{\zeta,n,m}(r,\theta,\varphi) = NY_{l,m}(\theta,\xi)r^{2n-2-l}e^{-\zeta r^2} \tag{3.18}$$

where the type of the orbital is determined by the sum of l_x,l_y, and l_z.

Slater Type Orbitals are more accurate since they are based on the solution of the Schrödinger equation for the hydrogen atom yet Gaussian type orbitals are cheaper and behave better numerically. During this research study different basis sets have been employed and the criteria of choosing a specific function when dealing with different molecules will be discussed in detail in the following chapters.

3.2.3 Beyond the Hartree-Fock Method

In the Hartree-Fock method, the electron-electron repulsion is treated as an average since only a single determinant is selected for the trial wavefunction. The difference of the exact energy with the Hartree-Fock energy is known as *Electron Correlation* energy. Two types of correlation energy are defined, the "dynamic" which accounts for the instantaneous movement of the electrons and the "static" or "non-dynamic" which applies to degeneracy near cases which a single determinant cannot describe correctly. Despite that the *Electron Correlation* energy is a small fraction of the total energy, it becomes important in some cases, such as excited state calculations. Thus, a variety of methods which employ the Hartree-Fock wavefunction as a starting point (trial wavefunction), consisting of more than one determinant have been developed

$$\Psi = c_0\Phi_{HF} + \sum_{i=1} c_i\Phi_i \tag{3.19}$$

where the excited configurations can be obtained from the Hartree-Fock determinant if occupied orbitals are substituted by unoccupied ones. In order to determine the coefficients either perturbation theory[83] or the variational principle can be used. A full configuration interaction (CI) wavefunction that sums all the possible determinants and describes all the possible excitations has the following form

$$\Psi_{CI} = c_0\Phi_{HF} + \sum_S c_S\Phi_S + \sum_D c_D\Phi_D + \sum_T c_T\Phi_T + \cdots = \sum_{i=0} c_i\Phi_i \tag{3.20}$$

where S, D and T denote the single, double and triple electron excitation respectively.

Although an exact solution of the time-independent Schrödinger equation can be obtained with the CI method, it is computationally very expensive apart from the case of small molecules with no more than three atoms. Thus, a further approximation could be applied where the full CI expansion is truncated at a

specific excitation level. If only single electron excitations are included then the configuration interaction singles (CIS) is obtained. Analogously, single and double electron excitations are included at the configuration interaction singles doubles (CISD) level of theory and so on. However, truncated CI methods are not suitable for large molecules since the *Electron Correlation* energy is not properly scaled.

A very common approach is to use perturbation theory, where a small correction is added to a known solution of a simpler problem, to develop new methods. One of the most well-known methods is the Møller-Plesset second order perturbation theory (MP2).[84] Other methods are also available such as, coupled cluster (CC)[85] approach where an exponential excitation operator is employed to add correlation. The density functional theory (DFT)[85] is another approach, where the high dimensional electronic wavefunction is replaced by a three-dimensional density. In general, the aforementioned methods can acceptably calculate ground state energies and wavefunctions but they cannot describe excited states. Hence, other developments are needed such as algebraic diagrammatic construction (ADC),[86] equation-of-motion coupled-cluster model with single and double substitutions (EOM-CCSD)[87] and time-dependent density functional theory (TDDFT).[88]

Furthermore, in the cases where the Hartree-Fock wavefunction cannot be used as a reference, static correlation effects can be added to the reference wavefunction when more than one electronic configuration is needed to describe the ground state and therefore as a reference for the excited states leading to the multiconfigurational self-consistent field (MCSCF) method.[85] In this method both the orbitals and the coefficients are iteratively optimized in contrast with the CI method where only the coefficients are optimized. A very popular variant of the MCSCF method is the complete active space self-consistent field (CASSCF)[89,90] where the orbitals that contribute most to the target electronic states, known as active orbitals, are selected and then a full CI calculation is performed in this active space. The

active orbitals used as a starting point for CASSCF are normally a subset of the highest occupied and lowest unoccupied orbitals calculated using the Hartree-Fock method. One bottleneck of this method is that it heavily relies on the knowledge of the system under investigation in order to choose the appropriate active space.

The missing static correlation energy is addressed by the various methods presented above but further approaches are needed to approximate the dynamic correlation energy. To this end, a multi-reference configuration interaction (MRCI)[85] approach has been developed applying a CI method on a MCSCF wavefunction resulting in a quite accurate but extremely expensive method. To overcome this drawback a set of configurations is selected, such as symmetry adapted linear combinations of Slater determinant, leading to a multi-reference perturbation theory (MRPT)[85] method where Møller-Plesset perturbation theory is applied on a MCSCF reference. This method is mainly used within a reduced active space in order to still be accurate but also reduce the computational effort, resulting in a method known as complete active space perturbation theory second order (CASPT2).[83,91] It is commonly used in many studies to benchmark the computer simulations of any molecule under investigation.

3.3 Nuclear Dynamics

As described in Chapter 2, to study the electronic structure of a molecule the time-independent Schrödinger equation needs to be solved usually within the bounds of the BOA. Hence, single point calculations are performed at each nuclear geometry visited during the dynamics. However, molecules are not stationary which lead to the development of a plethora of dynamics methods focusing on the nuclear movement. Dynamics methods can be divided into three main categories, classical, semi-classical and quantum.

The first category is classical dynamics where in computational chemistry the

molecular mechanics subset is employed. Molecular mechanics employs classical mechanics in order to model a molecular system. The Born–Oppenheimer approximation is considered valid and the potential energy is calculated as a function of the nuclear coordinates employing force fields. Molecular mechanics can be employed to investigate molecule systems with varying size and complexity.

The next category is the semi-classical methods where the simulation of molecular dynamics is accomplished by introducing quantum mechanical corrections into classical dynamics simulations. In semiclassical methods similarly with classical, the nuclei move according to the Newton equations of motion. The main reason that these methods were established was to carry out molecular fragmentation simulations following electronic decay processes. In these methods the nuclei evolve classically, while the electrons (or the PES) are calculated with *ab-initio* methods. A very popular one, among semi-classical methods was developed by Tully[92] to treat large systems and is known as surface hopping.

Finally, quantum molecular dynamics methods, which is the area under investigation in this research study, endeavour to characterize at the atomic level a chemical system's time-dependent evolution including quantum effects. Thus, a solution of the time-dependent Schrödinger equation[93] is attempted which can be written as

$$i\dot{\Psi} = \hat{H}\Psi \tag{3.21}$$

using units in which $\hbar = 1$. In every method that falls into this category a wavefunction is employed to describe the nuclei instead of describing them as particles. The system's energy in the configuration space can be calculated at different points in time, where a more general picture for the various molecular configurations is described by a potential energy surface. Areas on these surfaces where the nuclear wavefunction has a larger amplitude suggest the most likely position of the molecule.

3.3.1 Multi-Configuration Time-Dependent Hartree Method

The multi-configuration Time-Dependent Hartree (MCTDH) method is an algorithm for solving the time-dependent Schrödinger equation. This grid-based method can treat multi-dimensional, non-adiabatic systems in which PESs are strongly coupled. MCTDH is derived from standard propagation methods, in which the wavepacket and Hamiltonian are represented by a time-independent product basis, the calculation becomes computationally unfeasible as the number of degrees of freedom (DOF) increases. The MCTDH method accounts for this by representing the wavefunction using a number of so called single particle functions (SPFs) which may be one- or multi-dimensional and are time-dependent. The MCTDH wavefunction ansatz to solve the time-dependent Schrödinger equation can be presented as:

$$\Psi\left(q_1,..q_f,t\right)=\sum_{j_1=1}^{n_1}...\sum_{j_f=1}^{n_f}A_{j_1...j_f}\left(t\right)\varphi_{j_1}^{(1)}\left(q_1,t\right)...\varphi_{j_f}^{(f)}\left(q_f,t\right) \tag{3.22}$$

where $q_1,..q_f$ are the nuclear coordinates, $A_{j_1...j_f}$ are the time-dependent expansion coefficients and $\varphi_{j_1}^{(1)}...\varphi_{j_f}^{(f)}$ are the time-dependent SPFs for each DOF. Convergence for a dynamics calculation is accomplished by increasing the number of SPFs until the measured value does not change,[94,95] as in electronic structure methods. In a photodissociation reaction, for instance, an absorption spectrum that no longer changes would show that convergence has been reached.

Using a composite index for simplicity where $J=j_1...j_f$ and $\Phi_J=\varphi_{j_1}...\varphi_{j_f}$, equation 3.21 can be written:

$$i\sum_J\dot{A}_J\mid\Phi_J\rangle+i\sum_J A_J\mid\dot{\Phi}_J\rangle=\sum_J HA_J\mid\Phi_J\rangle \tag{3.23}$$

Multiplying from the left by $\langle\Phi_L|$

$$i\sum_J\dot{A}_J\langle\Phi_L\mid\Phi_J\rangle+i\sum_J A_J\left\langle\Phi_L\mid\dot{\Phi}_J\right\rangle=\sum_J\langle\Phi_L\mid HA_J\mid\Phi_J\rangle \tag{3.24}$$

where as $\langle \Phi_L | \Phi_J \rangle = \delta_{L,J}$, it is assumed that a time-independent basis-set, Φ, gives a solution for A

$$\begin{aligned} i\dot{A}_J &= \sum_J A_J \Phi_J \\ &= \sum_L \langle \Phi_J | H | \Phi_L \rangle A_L \end{aligned} \tag{3.25}$$

This is the full solution to the TDSE. For MCTDH Φ depends on time and a variational solution to the time-dependent Schrödinger equation needs to provide a coupled set of equations for the expansion coefficients and for the SPFs

$$i\dot{\boldsymbol{A}} = \boldsymbol{\mathcal{K}}\boldsymbol{A} \tag{3.26}$$

$$i\dot{\boldsymbol{\varphi}}^{(\kappa)} = \left(1 - P^{(\kappa)}\right)\left(\boldsymbol{\rho}^{(\kappa)}\right)^{-1}\boldsymbol{\mathcal{H}}^{(\kappa)}\boldsymbol{\varphi}^{(\kappa)} \tag{3.27}$$

where $\boldsymbol{\mathcal{K}}$ is the Hamiltonian matrix element

$$\mathcal{K}_{JL} = \langle \Phi_J | H | \Phi_L \rangle \tag{3.28}$$

and $\boldsymbol{\rho}$ is a density matrix defined as

$$\rho_{ab}^{(\kappa)} = \left\langle \Psi_a^{(\kappa)} | \Psi_b^{(\kappa)} \right\rangle \tag{3.29}$$

where the SPF of the κ^{th} mode, $\phi_a^{(\kappa)}$ are ignored by the single hole functions, $\Psi_a^{(\kappa)}$, and integration is over all the DOF apart from κ. $P^{(\kappa)}$ is the projector onto the space spanned by the SPFs

$$P^{(\kappa)} = \sum_j \left|\varphi_j^{(\kappa)}\right\rangle \left\langle \varphi_j^{(\kappa)}\right| \tag{3.30}$$

and the operator $\left(1 - P^{(\kappa)}\right)$ ensures that the time derivative of the SPF is orthogonal to the space spanned by the functions. A solution of the integrals of the following form is essential to solve the equations of motion for the coefficients and for the SPFs, Eq. 3.25.

$$\begin{aligned} \boldsymbol{\mathcal{K}} &= \langle \Phi_J | T + V | \Phi_L \rangle \\ &= \left\langle \varphi_{j1}^{(1)} ... \varphi_{jf}^{(f)} | T + V | \varphi_{j1}^{(1)} ... \varphi_{jf}^{(f)} \right\rangle \end{aligned} \tag{3.31}$$

The multi-dimensional integral can be conveniently evaluated if the SPFs are represented using a discrete variable representation (DVR)[96,97] as a basis set. The matrix elements of the kinetic energy operator can also be evaluated in the related finite basis representation (FBR). For full details see reference from Beck and Meyer.[98]

MCTDH is a really advantageous method, however in order to treat larger molecules new approximation pathways should be introduced that remove the grid restrictions. To that end, a more efficient approach is to employ suitable parametrized functions to replace some of the SPFs. By choosing Gaussian functions as the parametrized functions, the MCTDH wavefunction ansatz can be rewritten as follows

$$\Psi\left(q_1,..q_f,t\right)=\sum_{j_1=1}^{n_1}...\sum_{j_f=1}^{n_f}A_{j_1...j_f}\left(t\right)\prod_{k=1}^{d}\varphi_{j_k}^{(k)}\left(q_k,t\right)\prod_{k=d+1}^{f}g_{j_k}^{k}(q_k,t) \tag{3.32}$$

resulting in the G-MCTDH method.[82,99]

The reason behind choosing Gaussian functions is that initially the G-MCTDH method was developed for treating system-bath problems and Gaussian functions can very well describe the bath which is a set of oscillators. This method has been extensively applied in vibronic coupling models[100] and in high-dimensional system-bath cases.[101]

3.3.2 Variational Principles

Variational equations of motion, such as those of MCTDH in the previous section and vMCG in the next, mean that the expansion coefficients and basis functions evolve to provide the best possible solution to the TDSE. They are derived using a variational principle. The three best-known variational principles are Dirac-Frenkel,[102] McLachlan[103] and Lagrange.[104] In all the theories presented in this research study only the Dirac-Frenkel principle was employed which has the following form

$$\left\langle \delta\Psi \left| H - i\frac{\partial}{\partial t} \right| \Psi \right\rangle = 0 \tag{3.33}$$

Theorem

"The equations of motion derived from the Dirac-Frenkel variational principle conserve both norm and energy, if the Hamiltonian is Hermitian and time-independent, $\frac{\partial}{\partial t}H = 0$*, and if the model wavefunction* Ψ *itself is contained in the space of the allowed variations:* $\Psi \in \{\delta\Psi\}$*."*[105]

3.3.3 Variational Multi-Configurational Gaussian Method

One of the most significant disadvantages of grid-based methods is the necessity that prior to any calculation being performed, the complete, global potential energy surfaces must be fitted or computed as the integrals run over the whole configurational space. To eliminate the aforementioned restrictions the variational multi-configurational Gaussian (vMCG) method was introduced.[19,82,106] In this method parametrised Gaussian functions are replacing the multi-dimensional basis functions, which results in a purely Gaussian Wavepacket (GWP)[82,100,101,106–108] method.

The vMCG method employs the wavefunction *ansatz*:

$$\Psi(\boldsymbol{x}, t) = \sum_i A_i(t)\, g_i(\boldsymbol{x}, t) \tag{3.34}$$

with every part of the wavepacket described as a superposition of frozen GWPs. Every Gaussian is defined by its position and momentum in phase space.

The equations of motion require the evaluation of matrix elements of the potential energy function. Local harmonic approximation (LHA)[109–111] can be applied to the potential to make the evaluation of integrals straightforward. As a result, the potential is expanded around the centre point of every Gaussian function to the second-order

$$V_i(\boldsymbol{x}) = V(\boldsymbol{x}_0) + \boldsymbol{q}_i^T \boldsymbol{V}' + \boldsymbol{q}_i^T \boldsymbol{V}'' \boldsymbol{q}_i \tag{3.35}$$

where $\boldsymbol{V}^{'}$ and $\boldsymbol{V}^{''}$ are the first and second derivatives of the potential energy at $\boldsymbol{x}_0$, and $\boldsymbol{q}_i$ is the displacement coordinates from this point.

The kinetic operator has the following form if rectilinear coordinates are used

$$T = \sum_i \frac{1}{2m_i} \frac{\partial^2}{\partial x_i^2} \tag{3.36}$$

Each Gaussian basis function in the wavefunction ansatz, Eq. 3.34, is a multi-dimensional parametrised function of a set of coordinates, $\boldsymbol{x}$, and can be written as

$$g_i(\boldsymbol{x}, t) = \exp\left(\boldsymbol{x}^T \boldsymbol{\varsigma}_i(t)\, \boldsymbol{x} + \boldsymbol{x}^T \boldsymbol{\xi}_i(t) + \eta_i(t)\right) \tag{3.37}$$

with $\boldsymbol{x}$ a column vector of the coordinates, and $\boldsymbol{x}^T$ its transpose. The complex, time-dependent parameters in this function, represent the widths of the Gaussian functions with a square matrix ($\boldsymbol{\varsigma}$), the coordinates of the centre of the Gaussian functions and the momentum with a vector ($\boldsymbol{\xi}$) and the remaining parameters of the functions with a number (η). These parameters are advantageously arranged into a vector

$$\boldsymbol{\Lambda}_i = \{\boldsymbol{\varsigma}_i, \boldsymbol{\xi}_i, \eta_i\} \tag{3.38}$$

Thus, applying the Dirac-Frenkel variational principle, Eq. 3.33, and in consideration of the variations in the wavefunction ($\delta\Psi$), regarding both the Gaussian function and the expansion coefficients parameters, the equations of motion can be obtained. Using vector notation the former equations of motion can be written as

$$\boldsymbol{i}\dot{\boldsymbol{A}} = \boldsymbol{S}^{-1}(\boldsymbol{H} - \boldsymbol{i\tau})\, \boldsymbol{A} \tag{3.39}$$

$$\boldsymbol{i}\dot{\boldsymbol{\Lambda}} = (\boldsymbol{C})^{-1}\, \boldsymbol{Y} \tag{3.40}$$

where $\boldsymbol{H}$ is the Hamiltonian operator matrix

$$H_{ij} = \left\langle g_i \middle| \hat{H} \middle| g_j \right\rangle \tag{3.41}$$

and $\boldsymbol{S}$ is the overlap matrix expressed in the Gaussian function basis set

$$S_{ij} = \langle g_i | g_j \rangle \tag{3.42}$$

and $\boldsymbol{\tau}$ is differential overlap matrix

$$\tau_{ij} = \left\langle g_i | \frac{\partial}{\partial t} g_j \right\rangle \tag{3.43}$$

Eq. 3.39 is connected to the equations of motion used for the expansion coefficients in wavepacket dynamics (Eq. 3.26). The vMCG equations have thus some extra terms as the Gaussian basis set are non-orthogonal.

In Eq. 3.40, the tensor $\boldsymbol{C}$ is considered as a matrix and the matrices $\boldsymbol{Y}$ and $\boldsymbol{\Lambda}$ as vectors. Employing the usual nomenclature[106] $\boldsymbol{C}$ and $\boldsymbol{Y}$ have the form

$$C_{i\alpha,j\beta} = \rho_{ij} \left(S_{ij}^{(\alpha\beta)} - \left[\boldsymbol{S}^{(\alpha 0)} \left(\boldsymbol{S} \right)^{-1} \boldsymbol{S}^{(0\beta)} \right]_{ij} \right) \tag{3.44}$$

$$Y_{i\alpha} = \sum_j \rho_{ij} \left(H_{ij}^{(\alpha 0)} - \left[\boldsymbol{S}^{(\alpha 0)} \boldsymbol{S}^{-1} \boldsymbol{H} \right]_{ij} \right) \tag{3.45}$$

with

$$\rho_{ij} = A_i^* A_j \tag{3.46}$$

being the density matrix, and the superscripts α, β in the matrix elements indicate the derivatives of the Gaussian functions regarding the parameters of the Gaussian form (Eq. 3.37)

$$S_{ij}^{(\alpha\beta)} = \left\langle \frac{\partial g_i}{\partial \lambda_{i\alpha}} | \frac{\partial g_j}{\partial \lambda_{j\beta}} \right\rangle \tag{3.47}$$

$$S_{ij}^{(\alpha 0)} = \left\langle \frac{\partial g_i}{\partial \lambda_{i\alpha}} | g_j \right\rangle \tag{3.48}$$

$$H_{ij}^{(\alpha 0)} = \left\langle \frac{\partial g_i}{\partial \lambda_{i\alpha}} \middle| \hat{H} \middle| g_j \right\rangle \tag{3.49}$$

If $\alpha = 0$, then

$$\frac{\partial g_i}{\partial \lambda_{i0}} = g_i \tag{3.50}$$

that is equivalent to setting $\lambda_{i0} = \eta_i$.

Throughout this research work, the single-set formalism was employed to treat the various non-adiabatic cases where multiple electronic states were involved. The electronic states in the single-set formalism are incorporated as an additional DOF outlined by a finite basis labelling the states with only a single set of basis functions being employed

$$\Psi(\boldsymbol{x}, t) = \sum_{s=1}^{n_s} \sum_{j=1}^{n_j} A_{j,s}(t) g_j(\boldsymbol{x}, t)|s\rangle \tag{3.51}$$

The multi-set method also exists where in contrast to the single-set in which the GWPs have the same position in all the states, each PES has a set of GWPs where independent movement on other states is allowed. Since in direct dynamics fewer functions overall are required compared to standard vMCG and thus fewer evaluations of the PESs, the single-set method is more appropriate.

3.3.4 Direct Dynamics

Direct dynamics is the branch of molecular dynamics simulations that solves the time-dependent Schrödinger equation by allowing the calculation of potential energy surfaces *on-the-fly*.[18,19,106,112] The (DD-vMCG) method was developed to go beyond methods which are limited by the choice of coordinates and the need to know beforehand the shape of the PESs. Thus, an important advantage is the straightforward extension to larger systems that undergo long-range dynamics, and now the only limitation is the need to calculate potential energies with a quantum chemistry method of choice.

Direct dynamics simulations of photo-excited molecules are becoming the method of choice and a number of methods and codes have been developed for this, as described in detail in a review by Crespo-Otero et al.[113] These include surface hopping,[22,23,25–27,114] ab initio multiple spawning (AIMS)[1–3] and multi-configurational Ehrenfest (MCE).[22,23,25–27,114] DD-vMCG has the potential advantage over all of

these methods that it converges faster and includes all terms and couplings in the Hamiltonian.

DD-vMCG builds up the potential energy surfaces by creating a database of energies, gradients, Hessians and other information which are calculated on-the-fly through an interface to an external quantum chemistry software package. The idea of reading all the required information from a database instead of performing expensive electronic structure calculations for each point reached by the GWPs was applied previously in classical trajectory[115,116] and quantum trajectory methods.[117]

A major advantage of DD-vMCG is the freedom of choice of coordinates to avoid complicated expressions for the kinetic energy operator, while in grid-based methods coordinates must be chosen carefully when potential energy surfaces are fitted. Therefore, different studies have been performed employing the DD-vMCG method in normal modes,[118–121] Jacobi coordinates[122] and atomic Cartesian coordinates.[108]

Potential Energy Surface Database

When a DD-vMCG calculation is conducted, the nuclear wavepacket is built by using a linear combination of multi-dimensional GWPs, each placed at the centre of a specific point in the configuration space. Thus, rather than calling at each time step the external electronic structure program, all the information needed is read from the database.

At the beginning of the calculation a parameter (db_{min}) which is called the database minimum distance is defined.[122] A detailed explanation of the use of the dbmin parameter is given below. The choice of the value of database minimum depends on the system. For each new molecular geometry, the Euclidean norm of the difference is calculated between the vector of all these new points and all the points of the geometries existing in the database. Then, if the lowest value of the aforementioned norm is greater than the database minimum the external program

is called to compute the energy, gradients and Hessian and everything is saved in the appropriate database. This stored information is then applied to expand the potential energy surface to second order of a Taylor series (LHA)

$$\boldsymbol{V}(\boldsymbol{x}) = \boldsymbol{V}(\boldsymbol{x}_0) + \boldsymbol{V}'(\boldsymbol{x}_0) \cdot (\boldsymbol{x}_0)(\boldsymbol{x} - \boldsymbol{x}_0) + \frac{1}{2}(\boldsymbol{x} - \boldsymbol{x}_0) \cdot \boldsymbol{V}''(\boldsymbol{x}_0)(\boldsymbol{x}_0) \cdot (\boldsymbol{x} - \boldsymbol{x}_0) \tag{3.52}$$

where the gradient $\boldsymbol{V}'(\boldsymbol{x}_0)$ and the Hessian $\boldsymbol{V}''(\boldsymbol{x}_0)$ are estimated at x_0 and are relative to any alteration in nuclear geometry.

In the case where the lowest norm is less than the database minimum then the energy, gradient and Hessian needed for LHA are obtained by a Shepard weighted interpolation[117] of existing database points which has the following formula

$$V(\boldsymbol{q}) = \sum_i \omega_i(\boldsymbol{q}) T_i(\boldsymbol{q}) \tag{3.53}$$

where T_i is the Taylor series expansion of the energy centred at the i^{th} database entry and w_i is a weight function that weights the contribution of this Taylor expansion

$$\omega_i(\boldsymbol{q}) = \frac{\nu_i(\boldsymbol{q})}{\sum_j \nu_j(\boldsymbol{q})} \tag{3.54}$$

and

$$\nu_i(\boldsymbol{q}) = \frac{1}{|\boldsymbol{q} - \boldsymbol{q}_i|^{2p}} \tag{3.55}$$

$$\text{with} \quad 2p > 3N - 3 \tag{3.56}$$

where N denotes the number of atoms and i the location inside the database. If the exponent p is sufficiently large then, in the limit, $N_{d\to\infty}$, Eq. 4.1 converges to the exact potential.

To be able to use once again the LHA, the expansion is truncated at second order while the energy, gradients and Hessian are saved for each entry. Nevertheless, the Taylor series in Eq. 3.53 must be truncated to first order to be used for the

gradients, and to zeroth order for the Hessians. In line with Eq. 3.52, for every $\boldsymbol{x}_i$ point the second-order Taylor series for the PES is formed and the energy is calculated at the new geometry.

Hessian Matrix Updating

As described above, the potential energy, gradient vector and Hessian matrix must be included in the database in order that local harmonic approximation can be employed to calculate matrix elements and extrapolated energies, gradients and Hessians. However, computing a Hessian at every database point is computationally very demanding, even if computationally cheap methods such as restricted Hartree-Fock are available.

In the interest of reducing the effort in executing a DD-vMCG calculation, an approximation method to calculate Hessians is applied which only needs a reference Hessian and gradient information. A version of the Powell update algorithm[117] was introduced to the Quantics program to avoid problems in the case where the Hessian becomes singular. The equation that gives the Hessian update has the following form

$$\mathbf{HS}_{New} = \mathbf{HS}_{Old} + \frac{1}{\boldsymbol{\delta}.\boldsymbol{\delta}}(\boldsymbol{\epsilon} \otimes \boldsymbol{\delta} + \boldsymbol{\delta} \otimes \boldsymbol{\epsilon}) - \frac{\boldsymbol{\epsilon}.\boldsymbol{\delta}}{(\boldsymbol{\delta}.\boldsymbol{\delta})^2}\mathbf{HS}_{Old}.\boldsymbol{\delta} \otimes \boldsymbol{\delta}.\mathbf{HS}_{Old} \qquad (3.57)$$

where $\mathbf{HS}_{New}$ is the updated Hessian, $\mathbf{HS}_{Old}$ is the reference Hessian, $\boldsymbol{\epsilon}$ is the vector of gradient difference and $\boldsymbol{\delta}$ is the vector of the position difference between the two examined geometries. The symbol $\otimes$ denotes the direct sum.

At the beginning of any calculation generally the database is empty, thus the evaluation of the Hessian matrix for the first GWP at the first point to obtain the reference Hessian for the later calculations is necessary. If the calculation starts with a non-empty database the primary entry will play the role of the reference. So as the propagation progresses, the only change with the former approximation is that each time a new database point is required, just the calculation of the

energy and gradient at this point is performed. The distance among the reference and the new point, and also the distances among the reference point and all points included in the database are calculated. The database entries are then divided into two groups; an external part of points that are further away from the reference point and an internal part that are closer.

A Powell update for the Hessian ($\mathbf{HS}_i$) is calculated at any new point by employing the gradient at this new point, and the gradient and Hessian at any point in the internal part. The former calculation is performed for all the points in the internal part. Thus, knowing the distance among the new point and all the internal points (d_i), the Hessian at any new point can be obtained from the following weighted sum

$$\mathbf{HS}_{new} = \frac{\sum_{i \in Internal} d_i^{-4} \mathbf{HS}_{Old}^{(i)}}{\sum_{i \in Internal} d_i^{-4}} \tag{3.58}$$

Moreover, since a new Hessian is included in the database which is close to the reference point, it is important that the Hessians of all the external points are updated by using a similar Powell update which in this case includes also the Hessian at the new point. This procedure is vital to ensure that at each step, the Hessian of every point is generated via extrapolation of all the points nearer to the reference point than itself.

The Hessian approximation offers a significant improvement in reducing the time needed for a DD-vMCG calculation, depending also on the examined system and is very important especially for high level quantum chemistry methods where the computational cost of computing Hessians significantly increases. However, the accuracy of this method needs to be further tested.

Convergence with number of GWPs

In order to explore the relation between the number of Gaussian functions and the convergence an example computed using Direct Dynamics in a recent review[109]

will be followed. The system involves a proton transfer and the property calculated is the flux over the barrier. As depicted in Fig. 3.1, as the number of the GWPs increases the flux expectation value converges. It should be noted that for the first 15 fs the number of the GWPs does not affect the convergence. However, the 8 GWPs graph is quite inaccurate compared to the rest after 15 fs. As displayed, with 16 GWPs only quantitative differences exist and minima and maxima occurred at the same time during the propagation in comparison with greater number of GWPs. It is also important to note that the number of GWPs needed for convergence is also affected by the molecule under investigation.

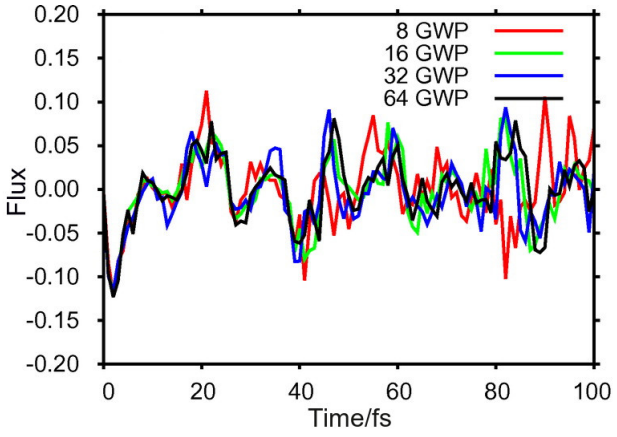

Fig. 3.1: The flux of the wavepacket over the proton transfer of the salicylaldimine molecule as the number of GWPs increases. Reprinted with permission from ref. 82.

As the number of GWPs becomes bigger, the fact that there is no orthogonality condition attached to the GWP basis can result in linear dependency problems within the basis. The solution to this problem is to remove the offending function from the basis set while the propagation progresses. This explains the undesirable fluctuations in the case of 64 GWPs after 60 fs.

In general, for the wavepacket dynamics methods like vMCG to accurately describe the dynamics of a molecule on a long time scale, a great number of GWPs is required. The explanation is that as time passes, the wavepacket can move quite far from its localised starting point thus a bigger number of basis

functions is required for the representation of the dynamics. At the same time, a drawback is that as the number of the GWPs is increasing the computational demand is higher as well. For instance, the direct dynamics calculation presented for the salicylaldimine molecule using 8 GWPs requires 221 seconds while with 32 GWPs the time was 7929 seconds.

Convergence with dbmin

Another important factor which can affect the convergence during a direct dynamics calculation is how often a computation of a new electronic structure will be executed. As mentioned before, this parameter is known as dbmin and its value can be altered in the input file in the Quantics package. As the GWPs move, the centre of a GWP will reach a new point, which represents a molecular geometry, where the potential needs to be calculated. If this point has not been examined before from any other GWP, to obtain the potential either a weighted expansion of prior calculated energies should be performed by using gradients and Hessians or a new energy value should be determined by conducting an electronic structure calculation.

So as to decide which strategy to follow the difference between all the geometries in the database and the new geometry is evaluated by calculating the Euclidean norm of the difference vector among all the coordinates. On condition that the minimum value of the former norm, i.e. the closest point in the database, is greater than the dbmin parameter, a new point should be calculated, but if it is smaller then the potential expansion is carried out.

To further understand how dbmin is connected with convergence, the example of the salicylaldimine molecule is considered again with varying dbmin values, from 0.075 Bohr to 0.75 Bohr, as depicted in Fig. 3.2. During the first 10 fs all the plots seem to be in agreement. As the time progresses, it is clear that the plots for higher values of dbmin and especially the one for 0.75 Bohr converge slower

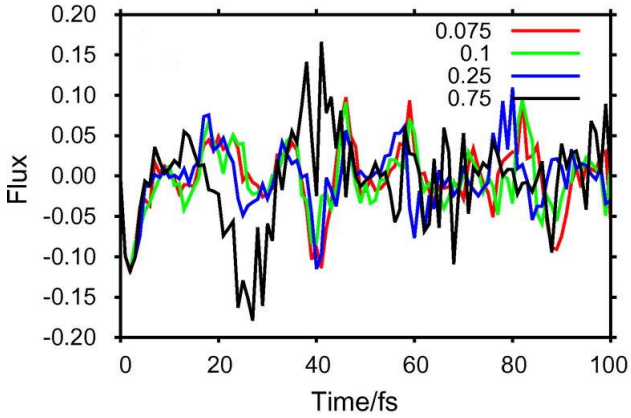

Fig. 3.2: The flux of the wavepacket over the proton transfer of the salicylaldimine molecule as the dbmin parameter increases. Reprinted with permission from ref. 82.

to the one with the lowest value, which will be considered as a reference for this comparison since it is constructed by employing *ab initio* points that are very narrowly spaced.

The reason behind all these inaccurate results in the propagation by using higher dbmin values is mostly connected with the number of points in the database. If the dbmin value is quite large, as explained above, in most cases when a GWP reaches a new point the energy will be calculated by weighted expansion and the previously calculated energies that are important for this approximation will be quite far from the point under investigation, which involves a higher error and eventually leads to a high inaccuracy since the harmonic assumption connected to the extrapolation becomes less valid. Thus, different dbmin values will give different dynamics in most cases.

Moreover, comparing the 0.1 Bohr dbmin value with the reference the results from the propagation are quite accurate and in agreement for almost the whole propagation. Some slight differences can be noticed after 90 fs but apart from the accuracy in convergence the computational cost should be considered as calculation of new points in the database is very expensive. For this example, 1262 points were calculated when dbmin = 0.075 Bohr and only 122 for dbmin = 0.1 Bohr.

Finally, this parameter is connected with the investigated molecule and the best practice is always to run different run tests before deciding the dbmin value. It is important to sensibly decide this value as we want to achieve the best possible convergence using the least computational effort.

Convergence of the Database

In order to study how the database converges, a first run will start with an empty database and then a subsequent propagation with the same initial conditions but with the database from the preceding propagation should be carried out. Considering only one GWP in a direct dynamics propagation that reaches multiple times the same point in the configuration space, each time a propagation is performed, the database is different as it is built and diabatised on-the-fly and therefore the extrapolated potential will not be the same. Hence, to get the best rendering of the dynamics, multiple propagations should be executed until no new points are added to the database. The former process of re-running a calculation aiming to add more points in the database is a key feature of direct dynamics. As a next step the final propagation will use this database to read all required information, energy, gradients and Hessian at each step which requires less computational effort.

Additionally, to ensure that there is no need of a re-run and convergence has been achieved, another important factor should be checked. No further calculations are needed only when there is no additional change to our selected expectation value and no new points added at the database. As depicted in Fig. 3.3, the salicylaldimine molecule is used again to test the database convergence. For this example a 32 GWPs basis and a 0.1 bohr dbmin have been used. All the different parameters in our input files play a crucial role, hence if a different number of GWPs was used that number of runs needed for the database to converge would have probably been completely different.

As taking into account the computational cost of on-the-fly quantum chem-

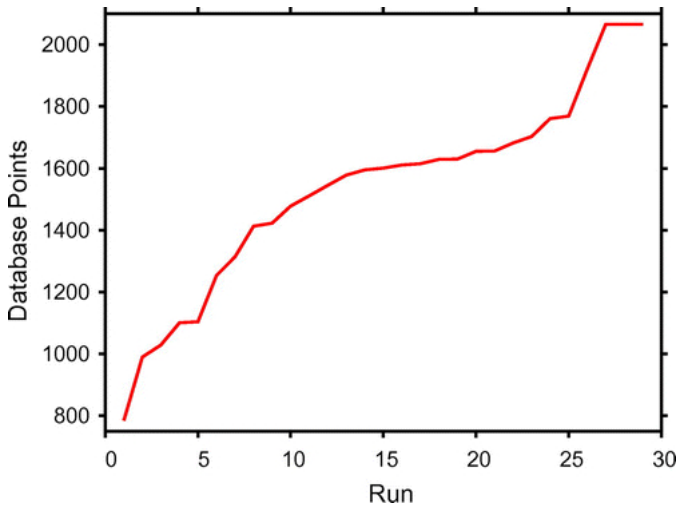

Fig. 3.3: Total number of points in the database for the salicylaldimine molecule in terms of the number of the propagations carried out, using as a starting point the database from the previous run. Reprinted with permission from ref. 82.

istry calculations is crucial, for quite large systems is impossible for the database to converge. Every time a re-run propagation is carried out, the database gets larger and the time needed for reading and sorting increases. Besides, different tests performed, including those on the salicylaldimine molecule, showed that the integrator's steps were shorter when changes in the PESs occurred and therefore the propagation time was longer.

Relaxation

Imaginary time relaxation is a method that can be used within the DD-vMCG framework, to locate, on a particular potential energy surface, a minimum energy nuclear eigenfunction.[123] This relaxation method is based on expressing the wavepacket as a set of eigenfunctions

$$\Psi(x,t) = \sum_i c_i \psi_i(x) e^{-i\frac{E_i t}{\hbar}} \tag{3.59}$$

where c_i represents the coefficient, E_i the energy and they are both associated with ψ_i which represents the eigenfunctions of the time-independent Hamiltonian. Subsequently, if real time is replaced by imaginary time and the energies are rescaled

allowing the minimum value to be zero

$$t \rightarrow \tau = it \tag{3.60}$$

eigenstates and eigenenergies of ground and/or low lying excited states can be obtained

$$\Psi = \sum_i c_i \psi_i e^{-\frac{E}{\hbar}\tau} \tag{3.61}$$

The higher energy components will decay faster exponentially as the propagation proceeds until only the wavepacket with the lowest energy eigenfuction remains. Relaxation requires much less computational effort compared to that needed for real time dynamics as just a small percentage of the configuration space is required to be sampled.

In relaxation, the PES is created similarly with the real time propagation where on-the-fly electronic structure calculations are performed. The database and the integrator's steps are also smaller compared to propagation which also explains the time difference between these two calculations. The output file created from the relaxation is going to be used as the initial wavefunction for the real time propagation.

3.3.5 The Quantics Package

The QUANTICS package[21] was used for the nuclear dynamics throughout this project. It solves the time-dependent Schrödinger equation for the nuclear motion by propagating wavepackets. Various algorithms can be employed, depending on the system of interest and the accuracy required. The focus of the package is the MCTDH and vMCG algorithms. Numerically exact propagation, as well as numerically exact diagonalisation of a one-dimensional Hamiltonian to get the eigenvalues and eigenvectors is feasible for small systems, and also solving the time-independent Schrödinger equation through Lanczos diagonalisation. The package also has the capability of generating a ground state or a nuclear excited state

wavefunction by employing energy relaxation, which is propagation in imaginary time. The code is Fortran 90 based with full dynamical allocation of memory. Parallelisation using OpenMP and MPI is made in many parts of the code to speed up calculations.[21] The code along with all the developments and improvements carried out during this research study is available on request in a private repository on GitLab.

Chapter 4

Developing the Direct Dynamics Variational Multi-Configurational Gaussian Method

The work of this Chapter has been published as G. Christopoulou, A. Freibert and G. A. Worth, J. Chem. Phys., 2021, (In Press)

4.1 Introduction

This chapter includes detailed results concerning the development of the *direct dynamics variational multi-configurational Gaussian* method. The main idea was to improve the existing code to have the best possible performance so that the treatment of complex molecules is feasible. Initially, different methods for interpolation were investigated and the most successful for direct dynamics is presented.

Computational methods typically have two of the three attributes described on the vertices of the triangle shown in Fig. 4.1, efficiency, accuracy or generality. Two are often achieved at the expense of the third attribute that they do not possess. Generality represents how well the method can adapt to a broad range of molecules. DD-vMCG calculations have the attributes of accuracy and generality, but they can be computationally expensive. The amount of time required to propagate quite complex chemical systems can last from several weeks for very experienced users, to even months for novice users.

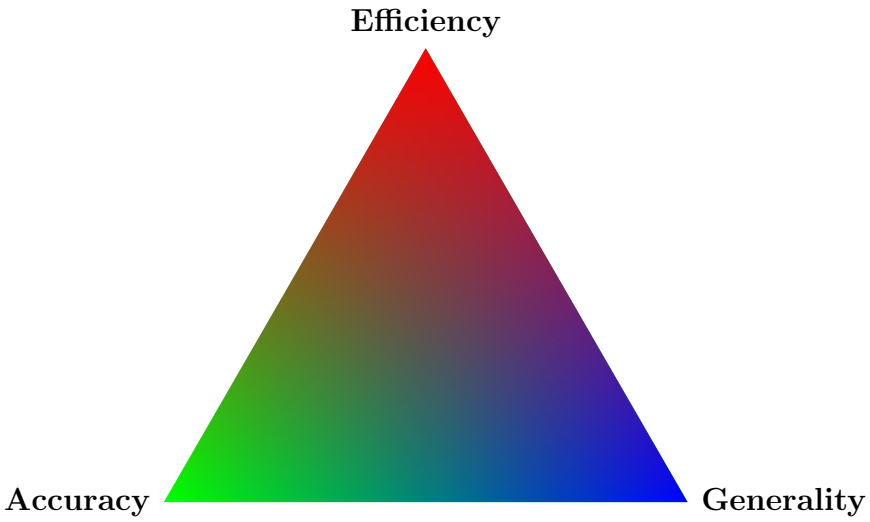

Fig. 4.1: Attributes of computational methods.

Aiming to increase the speed of the DD-vMCG method, a parallel algorithm focusing on improving both the efficiency and the accuracy of the currently employed code has been developed. A new approach for dealing with the computationally heavy process of continuously reading, sorting and analysing the DB is thoroughly discussed along with the efficient parallelisation of this part of the code. Finally, all the aforementioned methodological updates to the DD-vMCG implementation are described followed by an application of both the original and the updated version of the program to butatriene, allene and formamide molecules.

4.2 Modified Shepard Interpolation

As discussed in Chapter 3, in cases where there is no need for a new point to be calculated, a modified Shepard interpolation[117] can be employed to obtain the energies, gradients and Hessian matrix. The first step is to calculate the Euclidean norm of the difference vector of all atomic coordinates between the new point and each point inside the DB. The potential energy is then calculated by employing a weighted average of the Taylor series over the N_d data points.

$$V(\boldsymbol{x}) = \sum_i w_i(\boldsymbol{x}) T_i(\boldsymbol{x}) \tag{4.1}$$

where T_i is the Taylor expansion and w_i the function that weights the contribution of the Taylor expansion terms and has the following form

$$w_i(\boldsymbol{x}) = \frac{v_i(\boldsymbol{x})}{\sum_{j=1}^{N_d} v_j(\boldsymbol{x})} \tag{4.2}$$

In its simplest form, data points that are not close to $\boldsymbol{x}$ are assigned smaller weights compared to the ones that are very close by employing the primitive weight function v_i

$$v_i(\boldsymbol{x}) = \frac{1}{|\boldsymbol{x} - \boldsymbol{x}_i|^{2p}} \tag{4.3}$$

$$\text{with} \quad 2p > 3N - 3 \tag{4.4}$$

where N is the number of atoms and i the index of the point. If the exponent p is sufficiently large, then Eq. 4.1 in the limit, $N_{d\to\infty}$, converges to the exact potential.

To make this procedure more efficient, a maximum weight can be used as a criterion to exclude from the PES calculation the data points a large distance away from the new geometry. Together with this selection procedure, the aforementioned method allows a remarkably accurate calculation of PES for small chemical systems ($N < 4$).[124]

In a series of papers, Collins et al. investigated different forms of the weight function[115–117,125,126] for larger chemical systems ($N > 4$). It was concluded,[124] that a better performance is obtained using the following expression for the weight function

$$v_i(\boldsymbol{x}) = \left\{ \left[\frac{\|\boldsymbol{x} - \boldsymbol{x}_i\|}{rad_i} \right]^{2q} + \left[\frac{\|\boldsymbol{x} - \boldsymbol{x}_i\|}{rad_i} \right]^{2p} \right\}^{-1} \tag{4.5}$$

$$\text{with} \quad 2q > 2 \quad \text{and} \quad 2p > 3N - 3 \tag{4.6}$$

where p and q are positive integers and $p \gg q$ ensures that the first term of this equation is sum-dominant when $\|\boldsymbol{x} - \boldsymbol{x}_i\| < rad_i$ whereas the second term is sum-dominant when $\|\boldsymbol{x} - \boldsymbol{x}_i\| > rad_i$. The rad_i distance is a type of "confidence radius" supplied by a close point in the DB, j

$$rad_i = \|\boldsymbol{x}_j - \boldsymbol{x}_i\| \tag{4.7}$$

and the selection of the point j depends on the number of nearest points to be included and the molecule under investigation.

4.3 Local Dynamic Database

4.3.1 Conceptual Development

This section describes the methodology behind the improvement of the database scheme. Currently, the Quantics code is reading, sorting and analysing the whole database during each propagation step. This approach results in a great increase of the total calculation time for direct dynamics which is a limitation for successfully treating more complex chemical systems. While the main focus is to reduce the time needed for direct dynamics calculations, it is vital to build an algorithm that maintains a good balance between efficiency, accuracy and generality. Hence, the following requirements must be taken into consideration:

i. The algorithm should address the time delays caused by reading, sorting and analysing the database.

ii. The algorithm should have a high degree of accuracy when executing simulations.

iii. The algorithm should have a high computational efficiency with as little as possible redundant code.

iv. The algorithm should have the ability to run efficiently on both sequential and parallel operation

v. The algorithm should be robust with effective error controlling.

This database challenge is addressed by initially understanding the actual distribution of the data points during each propagation. Fig. 4.2 illustrates the concept employed by DD-vMCG during an excited-state dynamics where the green dots represent the centre of the GWP, the red ones the database points and the black lines the fit to these database points. The grey circle around the GWP of the ground state shows that at each time only a small number of closest points is required instead of the whole database, which constitutes the key concept of the development work presented here.

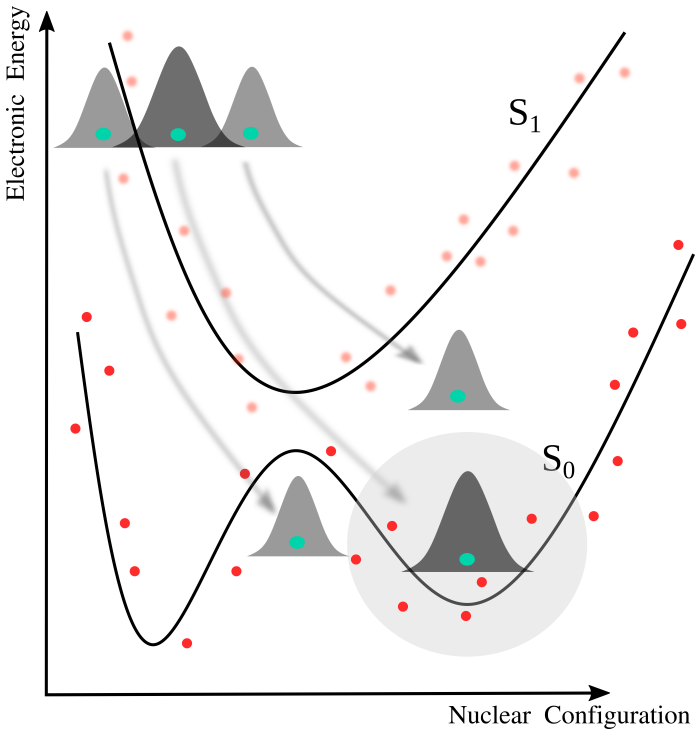

Fig. 4.2: Schematic representation of DD-vMCG method for excited-state dynamics where the green dots represent the centre of the GWP, the red dots the database energies and the black lines the fit to those points.

The next step was to determine a local database (DB) containing the n_{db} closest points in the database for each GWP by calculating the distances between the new

point and all the reference points in the database. It is important that the local databases are updated quite often so there are enough points each time sufficiently close to the centre of the GWP, allowing an efficient interpolation that does not lead to integration errors or instabilities. At the same time, updating the local DBs too often is not efficient, as it will slow down the calculation.

Aiming to find the best timescale for updating the database, the integration scheme was considered. The DD-vMCG method employs various integration schemes where the integration time is divided in two different time scales based on the constant mean-field integrator (CMF) that was developed for MCTDH.[98] Larger time steps, t_{large}, are used to describe quantities such as density, overlap and Hamiltonian matrices that generally tend to change slower than functions which are integrated individually using smaller, t_{small}, time steps. Hence the databases are refreshed every t_{large} where typically the movement of the GWP centre is significant.

A basic layout of the developed DD-vMCG algorithm is illustrated in Fig. 4.3. Begin and end time of the propagation is included for illustration purposes only as the flow chart mainly shows the part of the code where the local database is evolving. Also, for simplicity the flow chart shows the procedure for one point and hence one GWP during one propagation cycle. In a full direct dynamics propagation this process will of course be repeated at each integration step for each GWP.

Following the flow chart, after initialisation of the starting conditions, where parameters such as n_{db} and dbmin are defined, each GWP is going to reach a point in the configuration space, the reference point. The three different routes denote the three different options regarding the database existing in Quantics package and are itemized below:

i. **read**: the code only reads the database, calculates the PES from the database

and does not perform further QC calculations (route 1).

ii. **read and write**: the code reads the database and also performs QC calculations (route 2).

iii. **write**: the code performs QC calculations at each step and results are stored in the database (route 3).

When the **read** option is selected (route 1), then the local database is refreshed if the propagation time is equal to t_{large}. Subsequently, the local DB is read, sorted and analysed for the interpolation. In the case of the **read and write** option (route 2) there is an additional initial step to the process described for route 1. The code is searching for a point inside the DB that is at a distance less than dbmin compared to the reference point. If either the DB is empty or the datapoints are too far away then a quantum chemistry program will be called to compute the energy, gradients and Hessian matrix at the new point and then everything will be stored in the full QC and local DB. In the case of option **write** (route 3), most of the steps illustrated in the flow chart are skipped since only the quantum chemistry calculation is performed and then all information is stored in the local and full QC DB. The user can select which route the propagation will follow at the direct dynamics input file.

The role of the DB is quite crucial since the program could read, sort and analyse the DB three times for one point in the read and write option.

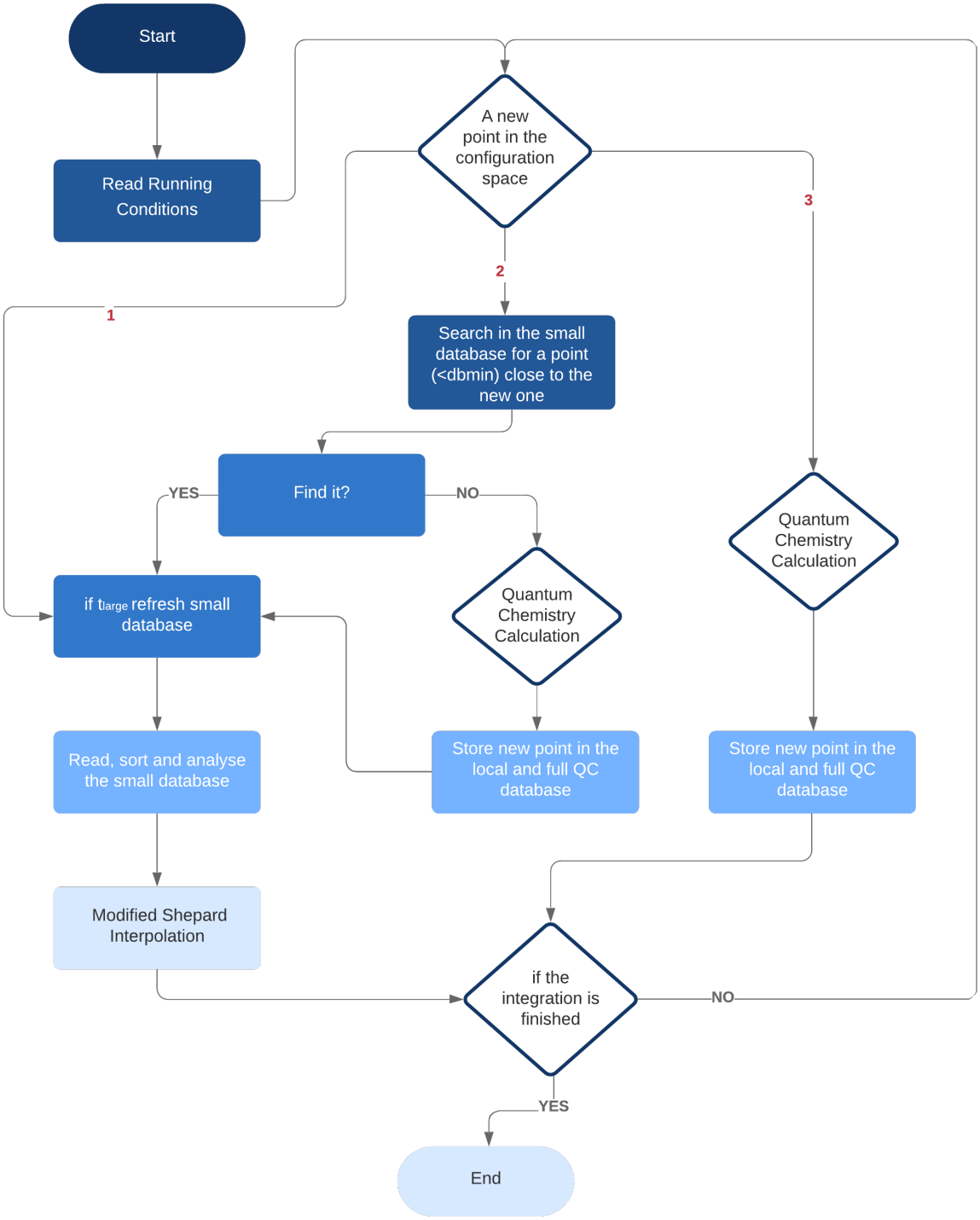

Fig. 4.3: Flow chart showing the layout of the DB scheme.

4.3.2 Code Implementation

The Quantics code is for the most part written in Fortran95, while a Fortran77 style is used for some of the older subroutines. The source code is divided into separate modules which combine interconnected subroutines and functions, such as one for data input and another for data output subroutines. Table 4.1 lists the main subroutines and their purpose.

Table 4.1: Main subroutines in the Quantics program involved in using the DB.

Subroutine	Description
prop	Controls the propagation of the wavefunction
funkr	Calculates the time derivatives of the wavefunction
gh_elements	Calculates Gaussian matrix elements of overlap and Hamiltonian
poteval	Calculates the value of the potential
DBread	Reads, sorts and analyses the DB
getddpes	Calculates potential energy surface(s) for direct dynamics

The first approach to implement the local DB idea presented in the previous section was to develop a small copy of the full QC database for each GWP that contains the energies, gradients and Hessians of the corresponding n_{db} closest points inside the full QC database. Every t_{large}, a small dynamic copy of the full QC database was created. Even though this approach was efficient and accurate, some bottlenecks arose. Between two updates of the local DB there is high chance that the centre of a GWP will reach a point in the configuration space where a new point needs to be computed and added both to the local and the full QC database. As a result, redundant code is created since big memory arrays are created to save the same data twice, when the local DB is refreshed and also when new points are added. Additionally, the size of the local DB arrays should be predefined, consequently the memory allocation always has to be bigger than needed to avoid the risk of not saving a new point.

Reflecting on the disadvantages of the aforementioned approach leads to a new

scheme which employs a single-linked list array whose size matches the number of GWPs and consists of a series of individual node elements pointing to the location of each of the $n_{\mathrm{db}}^{\mathrm{th}}$ closest points in the DB. In other words, instead of copying all the information, the location of the closest points inside the full QC database is tracked and copied using pointers that do not need to have predefined size as shown in Listing 4.1 where nGWP denotes the total number of the Gaussian wavepackets. A linked list is a linear data structure with its elements linked using pointers and are not stored at a contiguous location. Computationally, with this approach the upper limit on the number of elements is not fixed and does not need to be predefined which offers greater flexibility. Also, it is cheaper to use linked lists instead of arrays when possible as inserting a new element in an array of elements requires a space that is created for this new element by shifting the existing ones.

```
type ptr
  integer :: locDB
  type (ptr), pointer  :: next
endtype ptr

type list
  type (ptr), pointer  :: locpt
endtype list

type (list), dimension(nGWP), allocatable, save  :: ngp_loc
```

Listing 4.1: Definition of the "ptr" and "list" data types.

Apart from the linked-list arrays, some additional parameters shown in Listing 4.2 have been employed. These local DB parameters are the total number of closest locations inside each local DB, dbnrec_gp, a logical variable lgpupdate which holds the value false but will become true every t_{large} so the code knows when to update each local DB and the GWP number, num_gp, to inform the code which DB to access. All these parameters are global variables which are stored in a separate module that only contains variable definitions and initialisations.

In terms of the Quantics code, the advantage of the local DB approach is

twofold. During the integration steps the computational effort is remarkably less and thus the DD-vMCG method can be used for more complex processes, and also a higher number of GWPs to describe the wavefunction can be used. Further, the local DBs are all independent so the code can be efficiently parallelised.

```
integer, dimension(nGWP), save   :: dbnrec_gp
logical, dimension(nGWP), save   :: lgpupdate = .false.
integer, save                    :: num_gp
```

Listing 4.2: Definition of the parameters employed for the local DB version of DD-vMCG.

Distance Criterion

Following the concept of the modified Shepard interpolation presented in section 4.2, in the DD-vMCG implementation two different parameters are employed for this step which are both user defined. The first one, n_{db}, as has been mentioned above is the number of closest points inside the full QC database which are going to be included in the local DB for each GWP. Further, the confidence radius is defined as the n_{conf} closest point inside the local DB. The n_{conf} number has to be less than or equal to n_{db} and both are numbers based on the distribution of the data points in the DB. At the moment, both local DB parameters depend on the molecule under investigation and require some initial test calculations so that the best combination can be chosen.

The local DB development accompanied with the implementation of the modified Shepard interpolation scheme yielded a more efficient way with respect to the computational time but not an energetically conserved system. After carefully testing various parts of the original Quantics code with different molecules an error in the distance criterion was discovered.

Since the quantum chemistry calculation is one of the most expensive tasks during a DD-vMCG calculation, whenever the centre of the GWP reaches a new point in the configuration space that is far away from all the other known points in the DB, it must be checked that no other GWPs are close to this point at

the same propagation time. This is very important to avoid calculation of the potential multiple times which would significantly decrease the efficiency of the execution. Previously, to overcome this obstacle the distance between the GWPs was calculated by employing the following code (Listing 4.3).

```
  integer                                  :: e,e1
! lrddb = if true do not calculate the point for this GWP.
  logical, dimension(nGWP)       :: lrddb
! ndofddpes = number of degrees of freedom for direct dynamics PES
! xgp = geometry of the GWPs
  real, dimension(ndofddpes,nGWP)      :: xgp
! gwpdist = distance between the GWPs
  real, dimension(nGWP,nGWP)           :: gwpdist
! dbmin = if a geometry is greater than dbmin from any point in
   the DB a new point is created
rea                                    :: dbmin
! distgwp = gets the distances between a set of GWPs
 call distgwp(xgp,gwpdist,nGWP)
    do e=2,nGWP
       do e1=1,e-1
          if (gwpdist(e1,e) .lt. dbmin) lrddb(e) = .true.
       enddo
    enddo
```

Listing 4.3: Code to calculate the distance between the GWPs centres.

This approach was really efficient but as thorough testing of code showed, it was not accurate and led to significant instabilities. As depicted in Fig. 4.4, where for illustration purposes a problem with four GWPs is employed, if the distance for the first two GWPs was less than *dbmin* then for the second GWP the program would not compute any new point. It would then check the distance between the second and the third and again if the distance is less compared to *dbmin*, the program would not compute any new point for the third GWP. This way a chain of GWPs can be created where one GWP is close to another but not close to the point which will be computed or close to any existing point in the DB.

Similarly to most computational accuracy errors occurring during the development of a program, it was much harder to locate and understand the source of the error than writing a piece of code to correct the error. Thus, an if statement was added to check that when a GWP is close to another, the logical variable for the

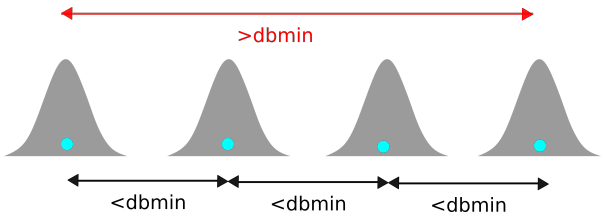

Fig. 4.4: Distance criterion for calculating a new point.

one has to be true and false for the other one to avoid the chain problem described above (Listing 4.4).

```
  integer                                  :: e,e1
! lrddb = if true do not calculate the point for this GWP
  logical, dimension(nGWP)                 :: lrddb
! ndofddpes = number of degrees of freedom for direct dynamics PES
! xgp = geometry of the GWPs
  real, dimension(ndofddpes,nGWP)          :: xgp
! gwpdist = distance between the GWPs
  real, dimension(nGWP,nGWP)               :: gwpdist
    real, dimension(nGWP,nGWP)               :: gwpdist
! dbmin = if a geometry is greater than dbmin from any point in
   the DB a new point is created
! distgwp = gets the distances between a set of GWPs
 call distgwp(xgp,gwpdist,nGWP)
    do e=2,nGWP
       do e1=1,e-1
         if (lrddb(e1)) cycleGWP
           if (gwpdist(e1,e) .lt. dbmin) lrddb(e) = .true.
       enddo
    enddo
```

Listing 4.4: New code to calculate the distance between the GWPs centres.

This important correction lead to better energy conservation and a faster and more stable integration. Together with the local DB approach it resulted in a competitive, efficient, and accurate DD-vMCG method for serial operation. Thus, the next step was to focus on the parallel operation of the code dealing with the DB to further speed-up the code.

4.4 Parallelisation

4.4.1 Parallel Environments in High Performance Computing

In various applications and especially large programs such as the Quantics package, limiting the execution to a single processor increases the total time of the computation. Further, employing a single processor is a waste of resources as nowadays all computer systems contain many cores. To build a powerful and efficient code, either a shared memory system like Open Multi-Processing (OpenMP) or a distributed memory system like Message Passing Interface (MPI) has to be employed to benefit from a simultaneous use of multiple processors.[127]

OpenMP is a multi-threading system where the shared memory architecture is employed, allowing sections of a code to be run simultaneously on different parallel threads. As depicted in Fig. 4.5, in lieu of sequential sections, parallel sections are introduced which are split by forks, then the jobs in each section are executed and finally recombined at joins[128].

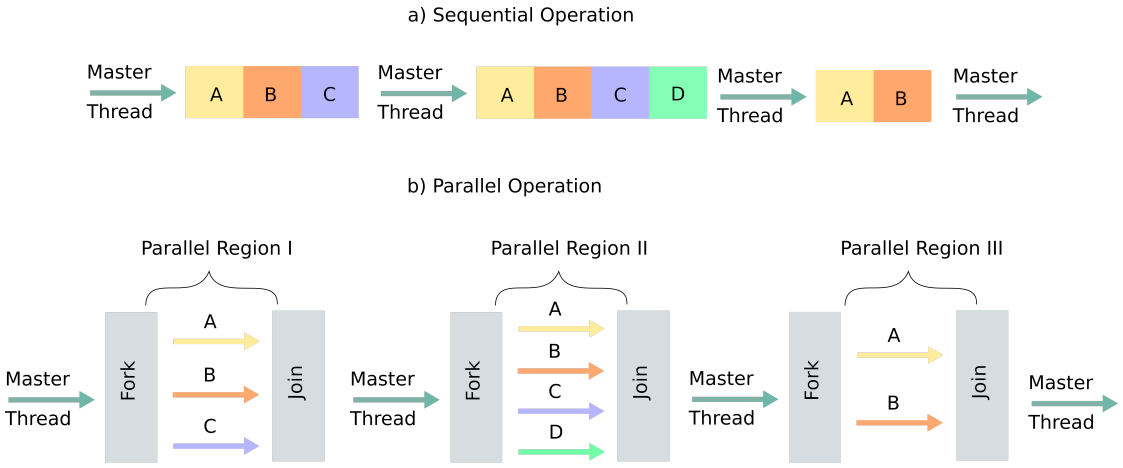

Fig. 4.5: Illustration of a) a sequential program in comparison with b) a program using the fork/join parallel function of OpenMP.

There is no need for communication among the threads, meaning that the execution of each thread is independent of the rest. Certainly, if a number of jobs are depending on each other then this part has to be sequential or parallelised in

an outer layer. Hence, most of the large programs, especially the ones that were originally written for serial operation, have both sequential and parallel regions.

As illustrated in Fig. 4.6, in the shared memory architecture employed by OpenMP the processors assigned for an execution are all attached to the same physical memory chip. This is a key feature of OpenMP as the cache for multiple processors can have a copy of data from the same memory address and hence various processing threads can use these data without needing message passing. The former feature together with the independent nature of the parallel threads in OpenMP leads to a parallel environment with little overhead.[128,129]

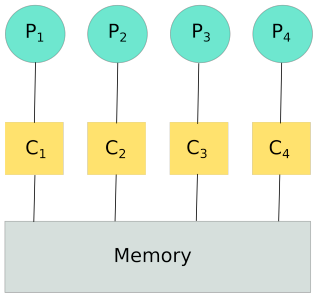

Fig. 4.6: Schematic of a single shared memory multiple processor node where C_i denotes the corresponding cache and P_i a processor.

However, if a program needs to perform a large number of parallel calculations, OpenMP is not suitable since the number of parallel operations cannot be larger than the number of logical processors sharing the memory chip. In these cases, a distributed memory system such as MPI is a far better approach. MPI employs a system where the communication between separate processes in a code is achieved by explicit messages. This requires the existence of a master process that distributes data to the slave processes. The latter then perform calculations, regularly interacting, and yield an outcome.

As depicted in Fig. 4.7, when MPI is employed, the restrictions coming from the single physical memory block are eliminated which is very beneficial for the code. Hence, the communication between the local cache memory of a single

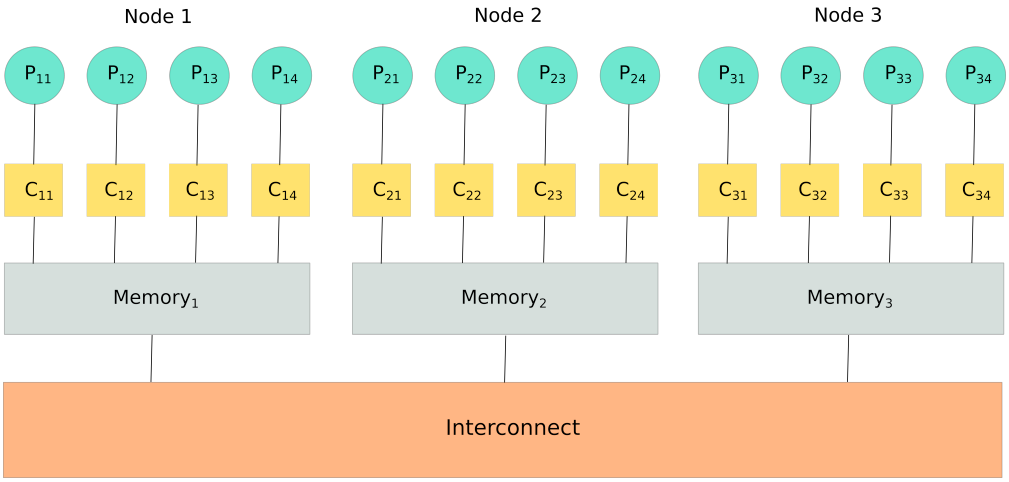

Fig. 4.7: Schematic of a cluster computer with multiple nodes, where C_{ii} denotes the cache assigned to the P_{ii} processor.

processor and a memory address having a location in a physical memory block on a separate node is feasible through the interconnect which exists between the nodes. For instance, the outcome of a calculation from the P_{22} processor can be passed to the P_{14} processor in the form of a message through the interconnect.

4.4.2 Running Quantics on Parallel Architectures

Quantics is a program that was originally written for serial operations and for relatively small chemical systems. The natural extension to larger systems created the need for parallel execution to respond to the more demanding calculations. In parallel computing, granularity or grain size of a process measures the amount of computational work performed by that process. Three categories exist regarding granularity. In fine-grained parallelism, a code is split into a high number of smaller processes which are allocated individually to many processors. The amount of work assigned to a parallel process is low and the computation is evenly spread between the processors. In coarse-grained parallelism, the code is broken down to large processes. Hence, a large amount of work occurs in the processors. This may lead to load imbalance and also most of the computational work operates sequentially. This approach benefits from synchronization overhead and low communication.

The definition of the last category, medium-grained parallelism, can be found in between fine-grained and coarse-grained parallelism where the communication time and task size are lower compared to coarse-grained parallelism and greater than fine-grained parallelism.[130,131]

The structure of the Quantics code does not allow the application of fine-grain parallelisation. As an example, for some integration schemes employed by Quantics, as for instance the Runge-Kutta, parallelisation is not possible in any accurate and sensible way since every calculation depends on the previous one and hence independent processes or threads cannot be constructed. Moreover, another impediment to parallelisation is due to the matrix operations where basic linear algebra subprograms (matrix-vector) operations are used. These operations even with the parallel basic linear algebra subprograms do not show a lot of improvement except for significantly large matrices. Therefore, coarse-grain parallelisation is applied to the Quantics code.

The Quantics code can be compiled to run on multiple processors using either the OpenMP or MPI protocols. It is important to note that parallelisation in the code is made over terms in the Hamiltonian, thus it is only efficient if the Hamiltonian has a long expansion.[132] During all the parallel developments conducted in this research project, the OpenMP approach was employed to parallelise various sections of the code dealing with the DB. For that parallelisation to be efficient, load balancing is critical. Thus, the efficient task distribution is based on the number of the Gaussian wavepackets. The local DB concept was to use as few variables as possible that do not rely on each other so that OpenMP can be successfully applied. The local DB approach is designed to speed up both the serial and the parallel calculations and a demonstration of its efficiency and capabilities is presented in the following section.

4.5 Test Cases

In this section, benchmark calculations on three model systems, butatriene, allene and formamide are presented. The aim is to test the accuracy, efficiency and generality of the newly developed DD-vMCG version. At the beginning, a comparison between the original DD-vMCG implementation and the developed version is conducted by exploring the PESs, the state population and energy conservation. The efficiency of the developed code is further examined by testing the total elapsed time for the propagation when using the full quantum chemistry (QC) database and the local DB versions to perform the same direct dynamics calculations in sequential operation. The parallel performance for the local DB version is also examined.

4.5.1 Butatriene Cation

Introduction

Butatriene ($C_4H_4^+$) is a linear planar molecule belonging to the D_{2h} point group at the neutral ground state equilibrium geometry as depicted in Fig. 4.8. It has 18 normal vibrational modes that are classified by the following irreducible representations

$$\Gamma = 4A_g + A_u + 3B_{2g} + 2B_{3g} + 3B_{1u} + 2B_{2u} + 3B_{3u} \tag{4.8}$$

The electronic ground state of the singly charged butatriene cation is denoted as X^2B_{2g} and has a B_{2g} symmetry while the first excited state has a B_{2u} symmetry and is represented as A^2B_{2u}. In an early research work,[133] due to different choice of the main axis these two states were labeled as B_{3g} and B_{3u}. In this study, the contemporary standard notation is employed. Considering that the energy separation between these two (X^2B_{2g} and A^2B_{2u}) lowest energy states and the next ionic state (B^2B_{3u}) is significant, the investigation and testing on butatriene can be reduced to a two-state problem.[134]

Moreover, the dominant electronic configurations of the ground and first excited state are $b_{2u}^2 b_{2g}^1$ and $b_{2u}^1 b_{2g}^2$, respectively. The formation of the first two electronic states is a result of the removal of an electron from the two highest-occupied orbitals, b_{2g} and b_{2u}. Torsional motion around the carbon axis has A_u symmetry and leads to vibronic coupling between these two ionic states. Thus, due to symmetry the possible candidates for the formation of a conical intersection are the totally symmetric modes. Apart from the central C-C stretching mode that is excited significantly, the other three totally symmetric modes are excited very weakly.[133] Butatriene was the first example of propagation diabatisation,[109] and thus it is always used as a standard test in DD-vMCG. It is an ideal test case due to its clearly defined conical intersection between the ground and first excited states.[106,112]

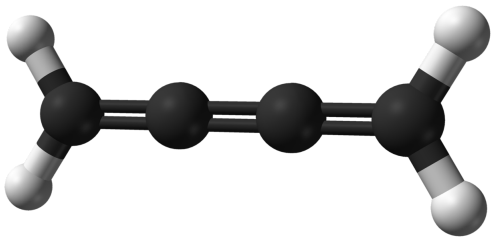

Fig. 4.8: The equilibrium ground state structure of butatriene.

Results and Discussion

Prior to the direct dynamics calculation, it is important to obtain the electronic structure of the molecule under investigation. In this case, calculations were conducted by using the GAUSSIAN 03 package.[135] The normal modes were evaluated at the neutral ground state geometry employing the state-averaged complete active space self-consistent field (CASSCF) method with 6 electrons in 6 orbitals covering the π-system, where each state was weighted equally. For all the calculations presented for the butatriene cation the 3-21G* basis set was selected for speed. The potential energies, gradients and Hessian matrices of the cation were obtained

applying the former level of theory by only including 5 electrons in 6 orbitals. The direct dynamics calculations were then conducted on the ground and first excited state of the cation. The wavefunction was centered initially at the Franck-Condon point and placed on the potential energy surface of the first excited state. The ground state normal modes of the molecules were used for the propagation with the frequencies defining the widths of the Gaussian wavepackets. The dynamics were then run for 100 fs with data output every 0.5 fs. For comparison purposes the number of GWPs and the dbmin parameter, which controls how often new electronic structure calculations are performed, were varied. The n_{conf} and n_{db} parameters are kept in most calculations equal to 4 and are stated if altered at any point during the study of the butatriene cation.

Fig. 4.9 shows the adiabatic and diabatic potential surfaces obtained employing both the previous DD-vMCG implementation and the developed version. For both versions, the crucial conical intersection is located at the same geometry and the shapes of the adiabatic surfaces are basically the same. However, the diabatic surfaces generated using the previous DD-vMCG implementation show points of discontinuity in the vicinity of the conical intersection. This issue is overcome while generating the diabatic surfaces with the developed version.

To verify that the actual nuclear dynamics are also reasonable, the normalised wavepacket population of the two diabatic states for DD-vMCG using both the original and developed versions is shown in Fig. 4.10. Starting from the fully populated first excited state (yellow line), for the first 10 fs both plots follow similar behaviour where an extremely fast depopulation is occurring. Here, the wavepacket moves to the ground states by passing the surface crossing seam. The DD-vMCG calculation using the original code shows a less clear structure of increasing and decreasing populations, especially during the first 40 fs, compared to the local DB version. Moreover, Fig. 4.10(b) is in a good agreement with other studies of the

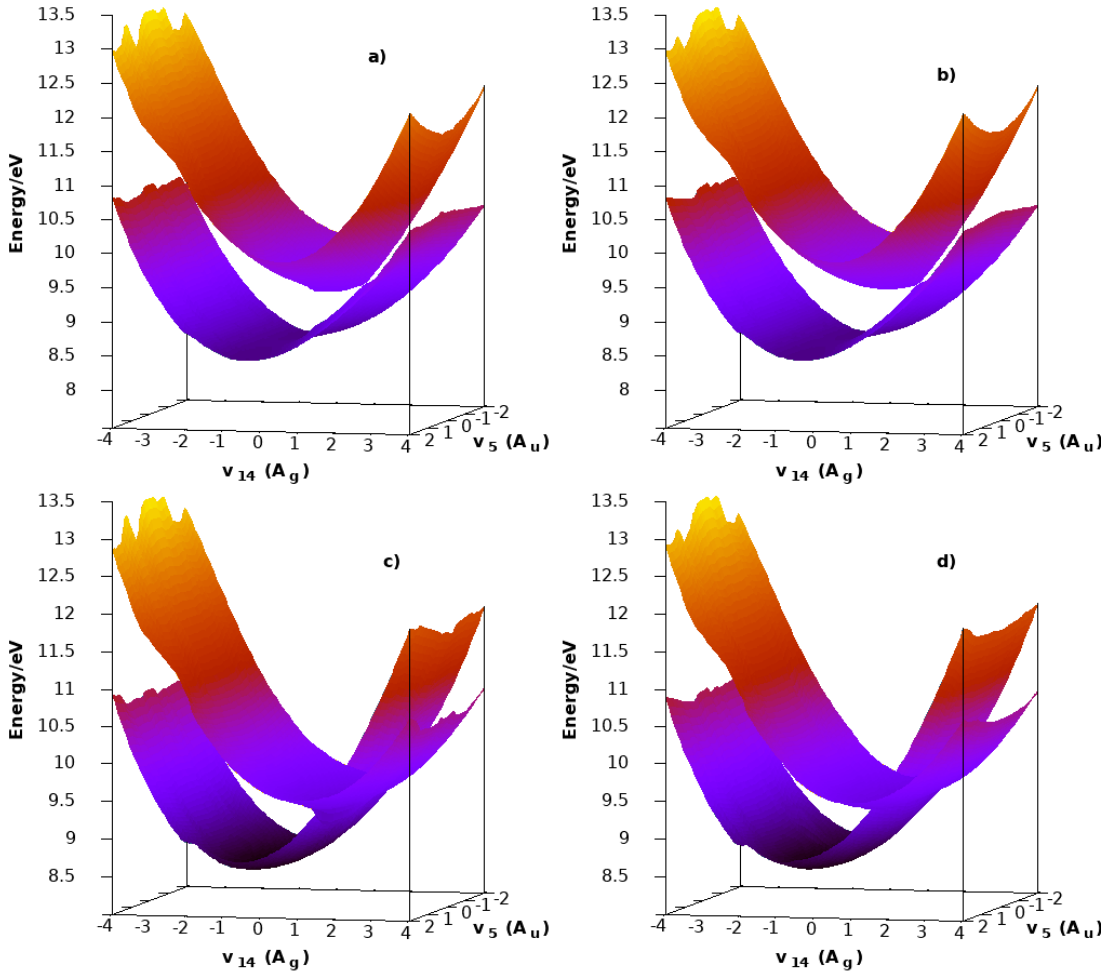

Fig. 4.9: Two-dimensional cuts through the a) adiabatic and c) diabatic potential energy surfaces employing the original DD-vMCG version, and the b) adiabatic and d) diabatic potential energy surfaces employing the developed DD-vMCG version for butatriene cation along the $\nu_5(B_1)$ and $\nu_{11}(B_2)$ normal modes.

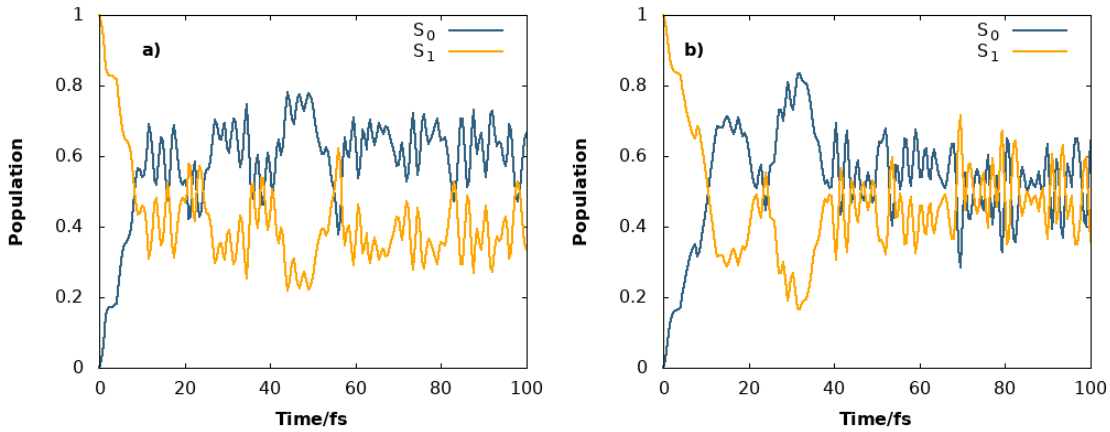

Fig. 4.10: Normalised diabatic state population from DD-vMCG simulations of butatriene cation using a) the original DD-vMCG version and b) the developed local DB DD-vMCG version.

butatriene cation.[106,134]

Further, a comparison of the total energy of the system during direct dynamics with the original and the developed local DB version is presented in Fig. 4.11. The results are impressive with respect to the energy conservation since using the local DB version leads to a totally energetically conserved system. This significant change in total energy conservation is related mostly with the correction of the distance criterion error and the implementation of the new interpolation scheme.

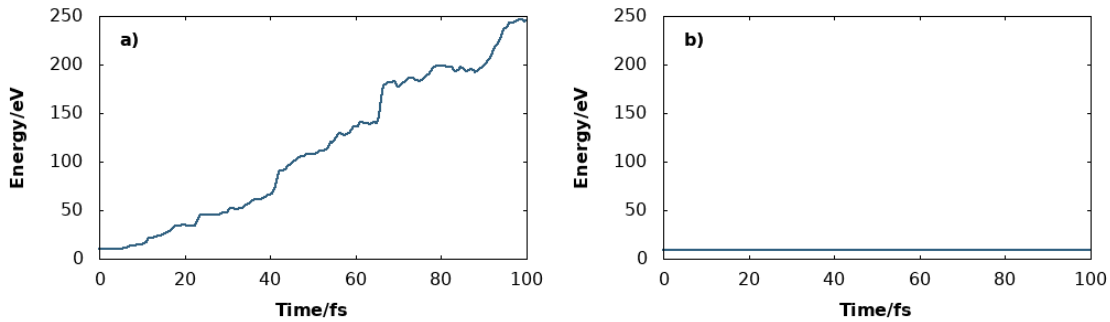

Fig. 4.11: Total energy for butatriene as a function of time using a) the original and b) the improved interpolation scheme for direct dynamics.

To explore the speed-up and the performance of the new code in comparison with the full QC database a series of calculations have been conducted. The speedup is defined as the ratio of the serial runtime of the full QC database to the serial runtime of the local DB to perform the same direct dynamics calculation.

Our aim was to create DBs with an increasing number of total data points so that the comparison offers a clear picture of the speed improvement. Initially, a set of calculations with decreasing dbmin value was conducted where the code performed only QC calculations at each step and results were stored in the DB. Since the dbmin parameter, the distance criterion for adding new structures to the QC database, controls how often a QC calculation is performed, decreasing its value leads to databases with a higher number of data points. For each of these databases created from the aforementioned step, serial calculations employing both the full QC database and the local DB implementation were performed. In these calculations, the code only reads the DB, calculates the PES from the DB and does not perform further QC calculations. During all these serial calculations most of the variables, such as the number of GWPs (10), the total propagation time (200 fs) and the interpolation confidence radius n_{conf} (6) have been kept constant. The number of points in the local databases, the n_{db} parameter, is affected by dbmin as when dbmin is reduced more points are needed to cover the space required for the interpolation. Hence, the various dbmin values together with the suitable n_{db} parameter are listed in Table 4.2.

As Table 4.2 demonstrates, the total elapsed time needed for all calculations regardless of the version employed increases when the number of points in the DB increases. In all cases the local DB code is faster than the full QC database code. In the case of the large database with 4907 points the local DB version is 40 times faster than employing the full QC database which validates the idea and the successful implementation of this local DB. Moreover, another advantage of the local DB approach is that the time needed for the same calculation is almost independent of the total number of points in the DB since the total wall times for the calculations using the local DB version are fairly similar. However, when the full QC database version is employed the total time required for the

Table 4.2: The total elapsed time for serial DD calculations for the local DB and the full QC database when varying the number of points in the full QC database by using different distance criteria (dbmin values). For all calculations the n_{conf} parameter was equal to 6.

Distance criterion	0.25	0.20	0.15	0.10	0.05
n_{db}	10	10	20	20	40
			Number of Data points		
	86	115	458	1242	4907
Full QC DB (sec)	2012	2819	6292	15222	124941
Local DB (sec)	1548	1566	1573	2003	3108
Speedup	1.3	1.8	4.0	7.6	40.2

same calculation drastically changes as the DB evolves which indicates the impact of dealing with the full QC database on the total calculation time. Moreover, it is important to note that using the local DBs has an additional advantage of quicker convergence during the propagation which results in fewer integration steps. Hence, the total amount of time needed for a full propagation is further reduced compared to the one when the full QC database approach is employed.

At the same time, the choice of the parameter n_{db} is potentially crucial as, in addition to the time and efficiency, it will also affect the dynamics and hence the accuracy of the calculation. To further understand the impact of n_{db} on the dynamics, the second example of the DD-vMCG calculation from Table 4.2 (dbmin = 0.2, 115 points) was employed as a starting point. Serial calculations where no new points are added in the DB but only the existing ones are read were then performed using local databases with different values of n_{db}. Additionally, a similar calculation only reading the current database was conducted employing the full QC DB version. As Fig. 4.12 shows, changing the number of points does not significantly change the population over time. Identical results with those employing the full DB, Fig. 4.12(a), can be achieved with local databases containing 10 points, as depicted in Fig. 4.12(d). As explained above, the number of points inside the local DB affects the interpolation and thus the integration

of the DD-vMCG calculation which explains the behaviour in Fig. 4.12(b) and (c) where the population is somewhat different compared to the full QC database calculation. Since for the allene cation a quite small n_{db} can be used as shown in Fig. 4.12, altering the n_{conf} parameter did not have any impact on the results. Potentially, for molecules that require more points in the local DBs and thus a larger n_{db} value, changing n_{conf} will also affect the dynamics.

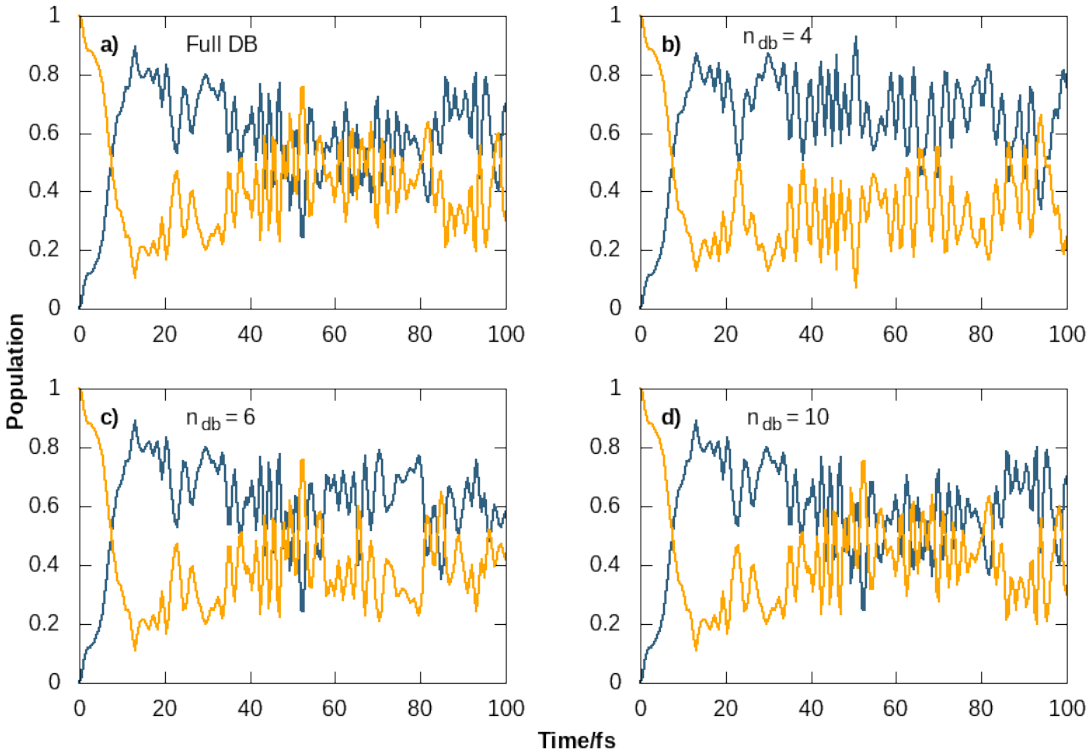

Fig. 4.12: The population of S_0 (blue line) and S_1 (orange line) states for the same DD-vMCG calculation of butatriene cation employing a) the full DB with 115 points and the local DB with b) 4 points, c) 6 points and d) 10 points .

The most accurate method of evaluating parallel performance is to run the same problem on 1 CPU and on n CPUs, and compare the total elapsed time for the iteration. The aim is to explore how scalable the parallel algorithm is, as a way to assess its capacity to efficiently use increasingly more processors. Thus, the parallel speed-up and efficiency of the new code is examined. The definition of Amdahl's law[129] was employed for the speedup ratio which is determined as the ratio of the total sequential time for finding the solution to a given problem to the

Table 4.3: The total wall-clock time for a parallel implementation of DD-vMCG using local DBs, with different number of cores[1] for butatriene cation.

	Number of Processors				
	1	5	10	15	20
4097 DB points - 10 GWPs					
Total Calculation					
Total Time (sec)	3108	1243	1072	1295	1351
Parallel Speedup	1.0	2.5	2.9	2.4	2.3
Database code					
Total Time (sec)	2067	559	369	422	440
Parallel Speedup	1.0	3.7	5.6	4.9	4.7
Efficiency	1.0	0.7	0.6	0.3	0.2
7847 DB points - 20 GWPs					
Total Calculation					
Total Time (sec)	12432	4440	4010	3657	3099
Parallel Speedup	1.0	2.8	3.1	3.4	4.0
Database code					
Total Time (sec)	6403	1779	1423	1164	736
Parallel Speedup	1.0	3.6	4.5	5.5	8.7
Efficiency	1.0	0.7	0.5	0.4	0.4

[1] Performed on a single node with 2 x 10 core Xeon 2.3GHz CPUs

time the parallel algorithm needs on n processors for the same problem.

Test calculations were carried out using the newly developed algorithm for the butatriene system. The computational cost for the local DB approach employing different number of processors is summarised in Table 4.3. Since the main coding development was focused on the DB, separate time data accompanied with the parallel speedup and efficiency are presented for both the part of the code that deals with the DB and for the total calculation. Comparison of the data only for the parallel code that deals with the DB reveals that in both examples the speedup increases with the number of processors, showing that the new local DB approach has a great impact on the efficiency of the method. For the second example (20 GWPs) a parallel process run on 20 processors was almost 9 times faster, which reveals a very good parallel performance even though for this example the advantage of a parallel calculation is quite small. The parallel speedup seems

to follow a similar pattern for both cases and a linear scaling with the number of cores is achieved which is in accordance with Amdahl's law.

Parallel efficiency is defined as the ratio of speedup to the number of processors. In this way a good estimate of the fraction of time for which a processor is usefully utilized can be determined. A program that scales linearly has parallel efficiency close to 1. Usually a task-parallel program is more efficient than a data-parallel program. Parallel codes can - more rarely - achieve super linear behaviour as a result of an efficient cache usage per worker. The overall efficiency of the parallel program decreases as the number of processors increases for the same problem. This is the case for all parallel programs. Moving to more complex calculations the efficiency will increase, as shown in Table 4.3 where the second test with more GWPs and more data points has a better performance.

Moving to the comparison of the total calculation, Table 4.3 shows that the speedup for the two parallel calculations of the butatriene cation follows Amdahl's law, achieving a speedup of 3 (10 GWPs) and 4 (20 GWPs) in the case where the number of nodes matches the number of GWPs. Further, for the first sets of calculations with 10 GWPs the speedup for both the total calculation and the DB code decreases when the number of processors exceeds the number of GWPs. This might seem odd, but it is in fact an expected behaviour as the part of the code dealing with the DB is parallelised based on the number of GWPs. The communication of the extra processors is causing more delays so it is better to keep the number of processors always less or equal to the number of GWPs.

As the total wall-clock time demonstrates, the largest memory and disc spaces are required for dealing with the DB when the number of data points is large as in these examples. The improvement of the parallelisation in the case of the total calculation will be moderated by the performance of the hardware communication subsystem and the overhead of the parallel process, which explains why the total

gain from serial to parallel is not massive. Additionally, it must be noted that only some bits of the total code are parallelised which also indicates that the speedup for the parallel calculations of butatriene cation will not be so substantial but may be for the calculations of much larger molecules. In general, if the parallelisable component of a code is 90% of total computation time the highest possible speedup is ten with many workers. The speedup drops to two for a 50% parallelisable code.[136]

4.5.2 Allene Radical Cation

Introduction

Moving towards more complex molecules to test the performance of the new code, the allene radical cation is chosen ($C_3H_4^+$). The equilibrium structure of neutral allene belongs to the point group D_{2d} as shown in Fig. 4.13. It has 15 normal vibrational modes which are classified by their irreducible representations

$$\Gamma = 3A_1 + B_1 + 3B_2 + 4E \tag{4.9}$$

The allene cation can be considered as a quite complex system resulting from the electronic ground state which is doubly degenerate at the Franck-Condon point, denoted by $\tilde{X}^2E$ and provides a representative example of the $E \otimes \beta$ Jahn-Teller effect, where the symmetry of the state is lowered by coupling to pairs of modes with B_1 and B_2 symmetry. Theoretical work on the Jahn-Teller effect in the allene cation by Cederbaum *et al.*[137] showed that the only modes that strongly couple the components of the ionic ground state are the $\nu_5(B_1)$ torsional and $\nu_{11}(B_2)$ antisymmetric $C-C$ stretching mode. The conical intersection formed by these two modes takes place exactly at the Franck-Condon point. In the area around that point the next energetically higher electronic states are well separated. Thus, as a starting point the investigation of the allene cation can be reduced to a system involving only two modes and two states.

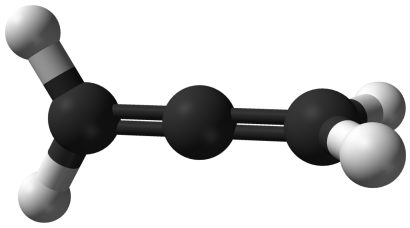

Fig. 4.13: The equilibrium ground state structure of allene.

Woywod and Domcke[138] reproduced the lower energetic part of the $\tilde{X}^2E$ - $\tilde{A}^2E$ states including the Jahn–Teller effect by employing a two-state four-mode linear vibronic coupling model Hamiltonian. Later, more precisely conducted studies were presented by Mahapatra *et al.*[139] and Worth *et al.*[140] on the higher lying $\tilde{A}^2E$ - $\tilde{B}^2B_2$ manifold where a three-state fifteen-modes Hamiltonian model was applied within the linear vibronic coupling scheme.

Results and Discussion

DD-vMCG nuclear dynamics were performed on the degenerate ground state of the ionic allene molecule including all degrees of freedom. The electronic structure calculations on the allene cation were performed using MOLPRO 2015.1[141] at a CASSCF(4,3)/6-31G* level of theory. The normal modes were obtained from a CASSCF(4,4)/6-31G* calculation at the neutral ground state geometry.

The GWPs used for the basis functions have a width $1/\sqrt{2}$ along all normal coordinates. In the mass-frequency scaled coordinate system used, this is the width of the neutral ground-state vibrational eigenfunction in the harmonic approximation. To form the desired initial wavepacket, one of these functions is placed at the Franck-Condon point with zero momentum and a coefficient of 1.0 for the configuration including the second state. All other GWPs are then displaced in phase space and given coefficients of 0.0, i.e. the initial wavepacket is an exact representation of the neutral ground-state eigenfunction placed vertically into the ion manifold.

To circumvent numerical problems coming from excitation into a point of degeneracy, the initial reference geometry for the DB was defined by a displacement of 0.4 units along the antisymmetric $C-C$ stretching mode, where the states are close to the conical intersection but not degenerate. Moreover, properties of the D_{2d} point group were applied to guarantee the correct symmetry of the potential energy surfaces.[142] The simulation was then carried out using 15 GWPs and a running time of 100 fs with data output every 0.5 fs.

Similarly to the first test system of butatriene, a comparison between the developed version and the previous DD-vMCG implementation is presented. The adiabatic and diabatic potential energy surfaces in the ν_5, ν_{11} branching space of the allene cation generated from the direct dynamics calculation are shown in Fig. 4.14. Employing the previous DD-vMCG version, both adiabatic (Fig. 4.14(a)) and diabatic (Fig. 4.14(c)) surfaces are not smoothly varying in the locality of the conical intersection, showing a lot of discontinuities. On the other hand, both the adiabatic (Fig. 4.14(b)) and diabatic (Fig. 4.14(d)) surfaces using the new developed version are perfectly smoothly varying along the two important modes. Moreover, the adiabatic surfaces feature a very well defined conical intersection at the Franck-Condon point as a result of the development work accompanied with a new diabatisation scheme employed for DD-vMCG.[143]

The normalised diabatic state populations, using both DD-vMCG versions are shown in Fig. 4.15. Employing the local DB version shows clearly defined periods of increasing and decreasing population over the entire time period in contrast to the initial calculations. As displayed in Fig. 4.15(b), an extremely fast decrease of the excited state population (yellow line) during the first few femtoseconds is followed by a rapid depopulation over the next 20 fs. That immediate population transfer is a result of the Franck-Condon point exactly meeting the CoI seam.

A key feature of an accurate simulation is that the energy and norm are con-

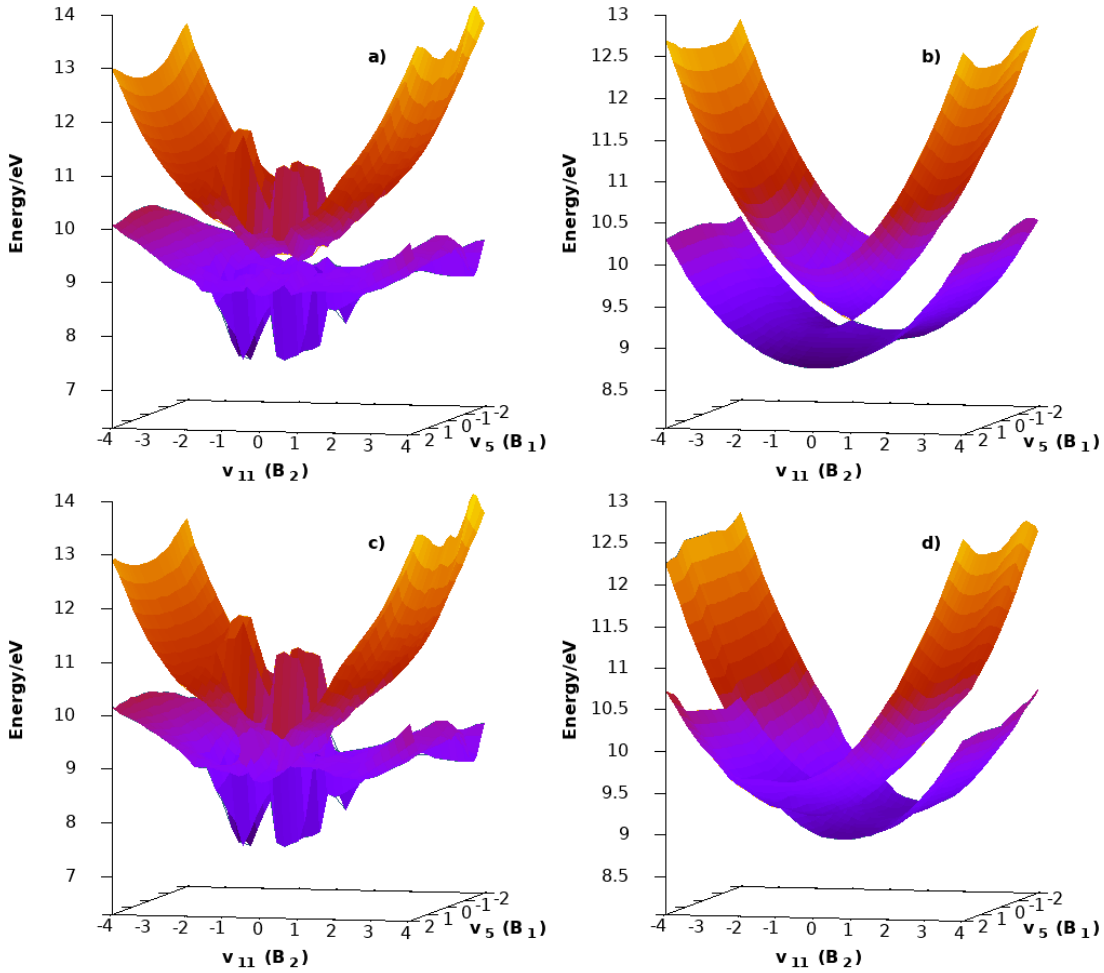

Fig. 4.14: Two-dimensional cuts through the a) adiabatic and c) diabatic potential energy surfaces employing the old DD-vMCG version, and the b) adiabatic and d) diabatic potential energy surfaces employing the new DD-vMCG version for allene cation along the $\nu_5(B_1)$ and $\nu_{11}(B_2)$ normal modes.

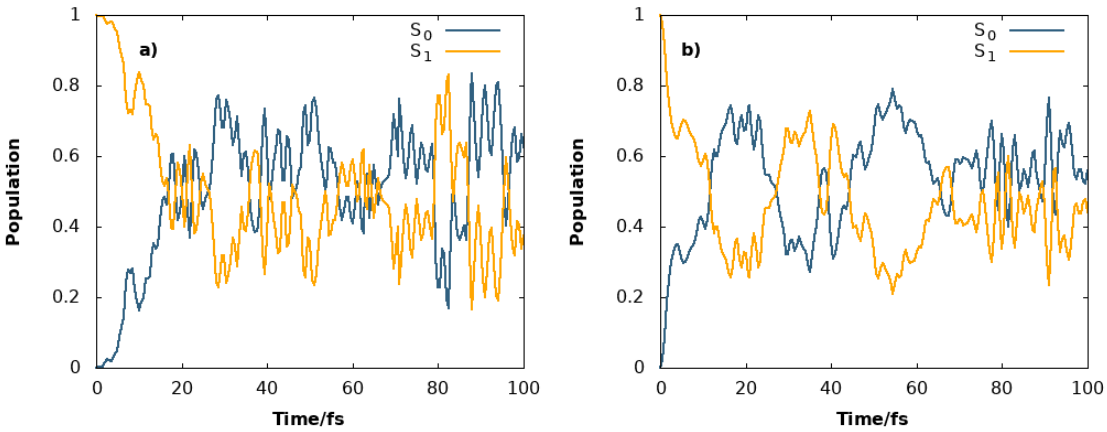

Fig. 4.15: Normalised diabatic state populations from DD-vMCG simulations of allene cation using a) the original and b) the developed DD-vMCG version

served. The total energy over the simulation is shown in Fig. 4.16 for both versions. The energy conservation for the previous version is very poor immediately after the calculation has started reaching a 200 eV energy difference around 50 fs. In contrast, during the simulation with the local DB version the energy is totally conserved throughout the calculation.

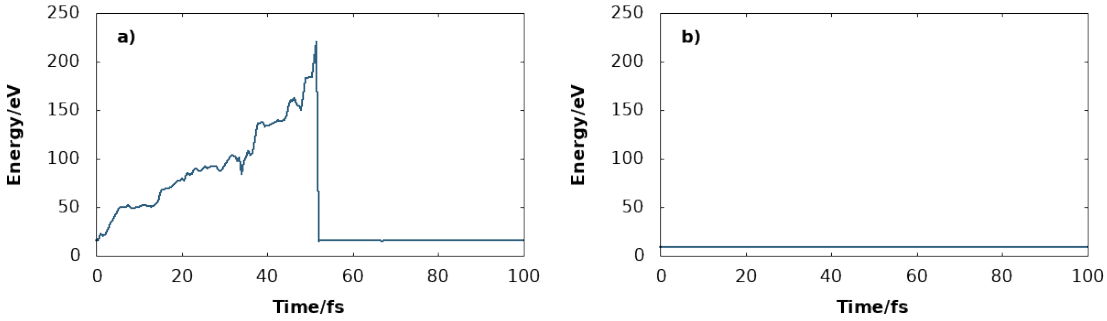

Fig. 4.16: Total energy for allene cation as a function of time using a) the original and b) the improved interpolation scheme for direct dynamics.

Moreover, to explore the speed-up and the performance of the new code in comparison with the full QC DB a series of calculations have been conducted. During these serial calculations all the variables, such as the number of GWPs (10), the total propagation time (200 fs) and the n_{conf} parameter (6) have been kept constant. Again, the n_{db} parameter is altered as presented in Table 4.4.

In Table 4.4, the total elapsed time for all calculations is listed along with

Table 4.4: The total elapsed time for serial DD-vMCG calculations with 10 GWPs using the full QC database and local databases, varying the number of points in the QC database by using different distance criteria (dbmin values). For all calculations the n_{conf} parameter was equal to 6.

Distance criterion	0.25	0.20	0.15	0.10	0.05
n_{db}	10	10	20	20	40
			Number of Data points		
	215	317	665	1292	5094
Full QC DB (sec)	3033	3226	4613	18833	125374
Local DBs (sec)	2766	2771	2756	3196	4723
Speedup	1.1	1.2	1.7	5.9	26.5

the speedup. It can be seen that the time required for a calculation is greater when the number of points in the QC database increases. Moreover, using local DB is always faster compared to using the full QC database and in the last case, with 5094 points, using the local database is 27 times faster. This confirms the idea that larger systems can be successfully treated with DD-vMCG. Another interesting result is that the total time needed for the local DBs when the number of data points are similar, e.g. 215, 317 and 665 points, is almost constant in contrast with the full QC database, breaking the negative dependence between the total propagation time and the number of points in the DB occurring during a full QC database calculation.

Similarly with the approach followed for the butatriene cation, the role of n_{db} is further explored for the allene cation. Here, the second example of the DD-vMCG calculation from Table 4.4 (dbmin = 0.2, 317 points) was employed as a starting point. As Fig. 4.17 depicts, serial calculations of the allene cation employing 20 GWPs show that the number of points (n_{db}) does not considerably change the population over time. Identical results with those of employing the full DB, Fig. 4.17(a), could be achieved with a 10 points local DB as depicted in Fig. 4.17(d). For all calculations n_{conf} was equal to 6.

Next, the parallel performance of the developed local DB algorithm is evaluated by running direct dynamics propagations using serial (1 CPU) and parallel

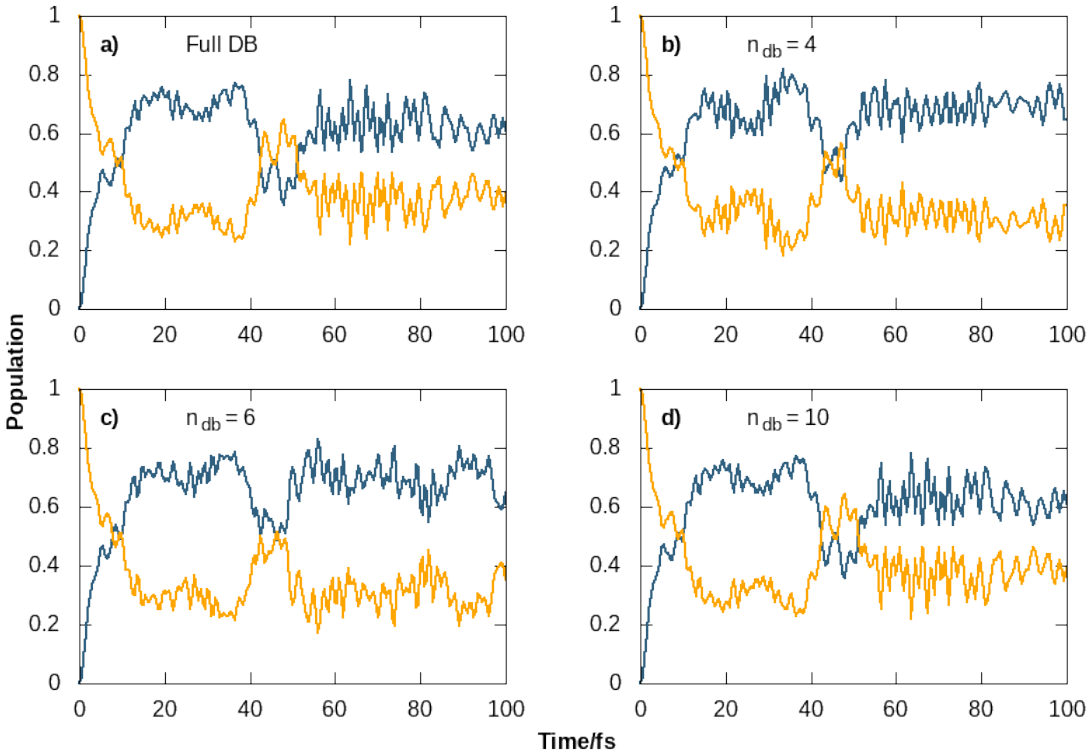

Fig. 4.17: The population of S_0 (blue line) and S_1 (orange line) states for the same DD-vMCG calculation of allene cation employing a) the full DB with 317 points and the local DB with b) 4 points, c) 6 points and d) 10 points.

(n CPUs) operation, and comparing the total elapsed time for the iteration in all cases. Benchmark calculations on the allene cation are shown in Table 4.5. Once more, considering that the main coding development was focused on the DB, separate time data accompanied with the parallel speedup and efficiency are presented for both the part of the code that deals with the DB and for the total calculation. The total propagation time (200 fs), the interpolation confidence radius n_{conf} (6) and the total number of points in the local databases, $n_{\text{db}} = 40$, have been kept constant.

Comparing initially the timings for the DB code, for both examples with 10 and 20 GWPs, the speedup increases with the number of processors. This validates the results using the butatriene cation and shows clearly that irrespective of the molecule under investigation, the new local DB approach has a great impact on the efficiency of the method. For the second example (20 GWP) a parallel process run

Table 4.5: The total wall-clock time for a parallel implementation of DD-vMCG using local DBs, with different number of cores.[1]

	Number of Cores				
	1	5	10	15	20
5094 DB points - 10 GWPs					
Total Calculation					
Total Time (sec)	4723	2050	1511	1599	1623
Parallel Speedup	1.0	2.3	3.2	3.0	2.9
Database code					
Total Time (sec)	3724	1033	587	598	604
Parallel Speedup	1.0	3.6	6.3	6.2	6.2
Efficiency	1.0	0.7	0.6	0.4	0.3
9797 DB points - 20 GWPs					
Total Calculation					
Total Time (sec)	18016	8903	5459	5004	4504
Parallel Speedup	1.0	2.0	3.3	3.6	4.0
Database code					
Total Time (sec)	11120	2926	1544	1463	1112
Parallel Speedup	1.0	3.8	7.1	7.6	10.0
Efficiency	1.0	0.8	0.7	0.5	0.5

[1] Performed on a single node with 2 x 10 core Xeon 2.3GHz CPUs

on 20 processors was 10 times faster which reveals a very good parallel performance. The parallel speedup seems to follow a similar pattern for both cases and a linear scaling is achieved which is in accordance with Amdahl's law. The efficiency of the parallel operation decreases as expected with the number of processors. However, for the second example where 20 GWPs are employed, the efficiency is higher. The efficiency will increase when moving to more complex calculations; this also applies here, as shown in Table 4.5, where the second test with more GWPs and more data points has a better performance.

The parallel performance of the total calculation follows the same pattern as with butatriene since a parallel speedup greater than two is achieved in both cases. As mentioned above the architecture of the main code does not allow a greater parallel performance of the total calculation. However, taking into account that for a DB containing around 5000 points, the speedup using the local DB algorithm is 27 (Table 4.4) and the speedup using the local DB algorithm in parallel operation

on n number of processors that matches the number of GWPs is 3 (Table 4.5), thus the total speedup is 81 which is a significant improvement.

4.5.3 Formamide

Introduction

Formamide (CH_3NO), also known as methanamide, is an amide derived from formic acid (Fig. 4.18). The water-assisted tautomerization of formamide to formamidic acid has attracted a lot of scientific attention from both experimentalists and theoreticians.[144–151] The NCO backbone of the formamide molecule can be found in DNA bases, and especially in thymine, cytosine and guanine. Thus, it can be used as a model for tautomerization in DNA bases.

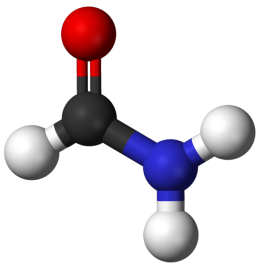

Fig. 4.18: The equilibrium ground state structure of formamide.

Theoretical investigation of formamide[80] using quantum dynamics simulations showed that the minimum ground state structure is non-planar and thus, formamide does not belong to any non-trivial symmetry point group. Since molecular symmetries can often be used to simplify quantum chemistry calculations, the planar structure was selected as the initial reference geometry in both electronic structure and direct dynamics calculations considering that the energy difference between the planar and non-planar geometry is small enough to be neglected. The planar formamide molecule possesses the identity operation E and a mirror plane σ, in which the C-N bond lies, as symmetry elements and thus belongs to the C_s point group. Its 12 normal vibrational modes can consequently be classified by

two irreducible representations, A' and A'', where properties symmetric to both symmetry elements correspond to A' and the rest corresponds to A''.

Results and Discussion

DD-vMCG nuclear dynamics simulations on formamide were conducted including eight electronic states and the ground state normal modes of the planar molecule, treated at a CASSCF(10,8)/6-31G* level of theory. The dynamics calculations were then propagated using 8 GWPs, a dbmin value of 0.1 and a running time of 150 fs with data output every femtosecond. These initial conditions match the ones used during the work of Spinlove et al.[80] with the original DD-vMCG implementation. The aim is to use the new developed version to compare with the results from Spinlove et al.[80] extracted with the original direct dynamics version.

Fig. 4.19 shows one-dimensional cuts through the adiabatic and diabatic potential energy surfaces along the ν_{11} symmetric (a and b) and the ν_{12} antisymmetric (c and d) N-H_2 stretching mode generated using the original DD-vMCG implementation. The main product channel, namely the NH dissociation, is provided by a combination of these two modes. In Fig. 4.19(a) and (b), it can be seen that a dissociative channel exists along the ν_{11} mode. Besides, in the vicinity of the Franck-Condon point along the ν_{12} mode in Fig. 4.19(c) and (d), the second (light blue) and third (orange) excited state are very close in energy and surface crossing occurs.

The recalculation of this particular system with the developed scheme indeed leads to much smoother surfaces (Fig. 4.20). The surface crossings of the third excited state (orange) along both modes, which are crucial for the NH dissociation channel, are still located at very similar displacements to the previous ones. However, the energy barrier of the dissociative channel along the ν_{11} mode is significantly higher than predicted before. Moreover, as a consequence of the larger energy barrier, seen in Fig. 4.20(a) and (b), the NH dissociation channel is less

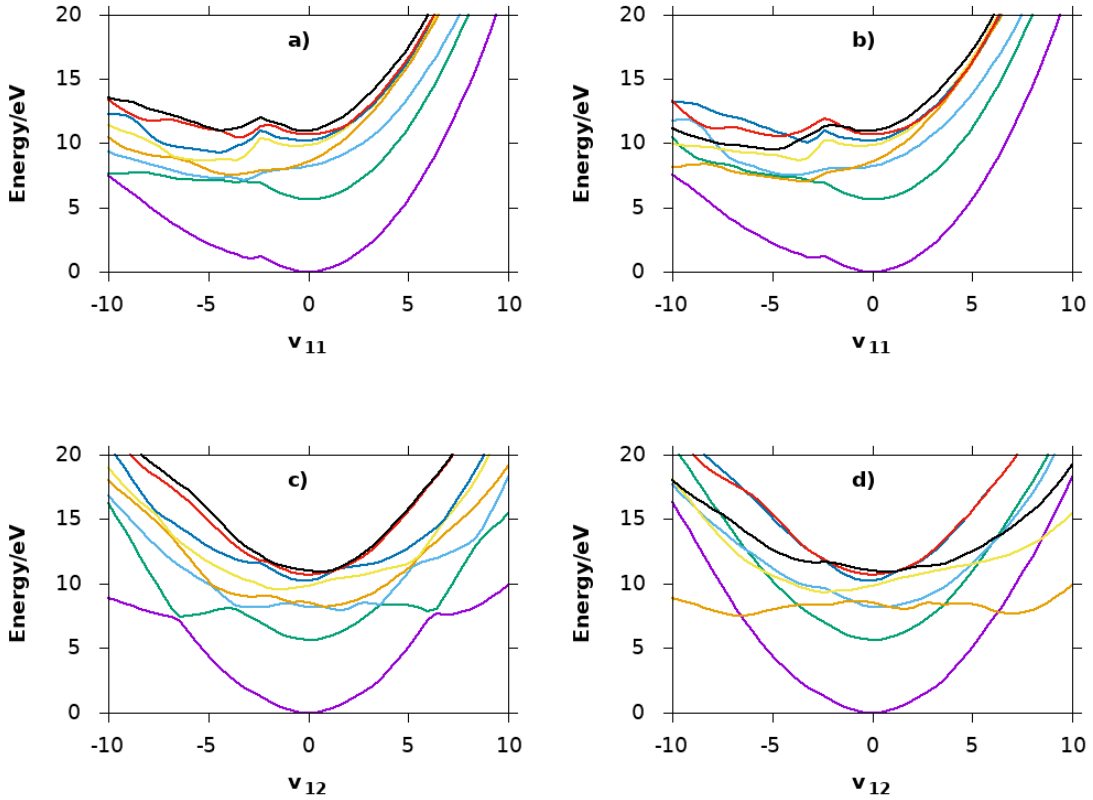

Fig. 4.19: One-dimensional cuts through a) the adiabatic and b) the diabatic potential energy surfaces of formamide along the ν_{11} N-H_2 symmetric stretching mode, and c) adiabatic and d) diabatic potential energy surfaces along the ν_{12} N-H_2 antisymmetric stretching mode employing the original DD-vMCG implementation.

probable than previously predicted from Fig. 4.19(a) and (b). An important difference relies on the dissociation occurring along the ν_{11} symmetric stretching mode, which is visible in Figs. 4.19(a) and (b), and not in Figs. 4.20(a) and (b) where the new developed DD-vMCG implementation was employed. This is more attributable to the way vMCG works and is not connected with the different implementations used for this comparison. Areas that are not sampled with vMCG give harmonic surfaces which explains why we do not get flatter asymptotic surfaces as expected from the ones reproduced from the Spinlove et al.[152] paper. In this paper different calculations starting on S_1, S_2 and S_3 states and with varying GWPs were performed, and the various databases created from these calculations

were then merged to a final one. Thus, larger areas were explored which explains the better description of the dissociation.

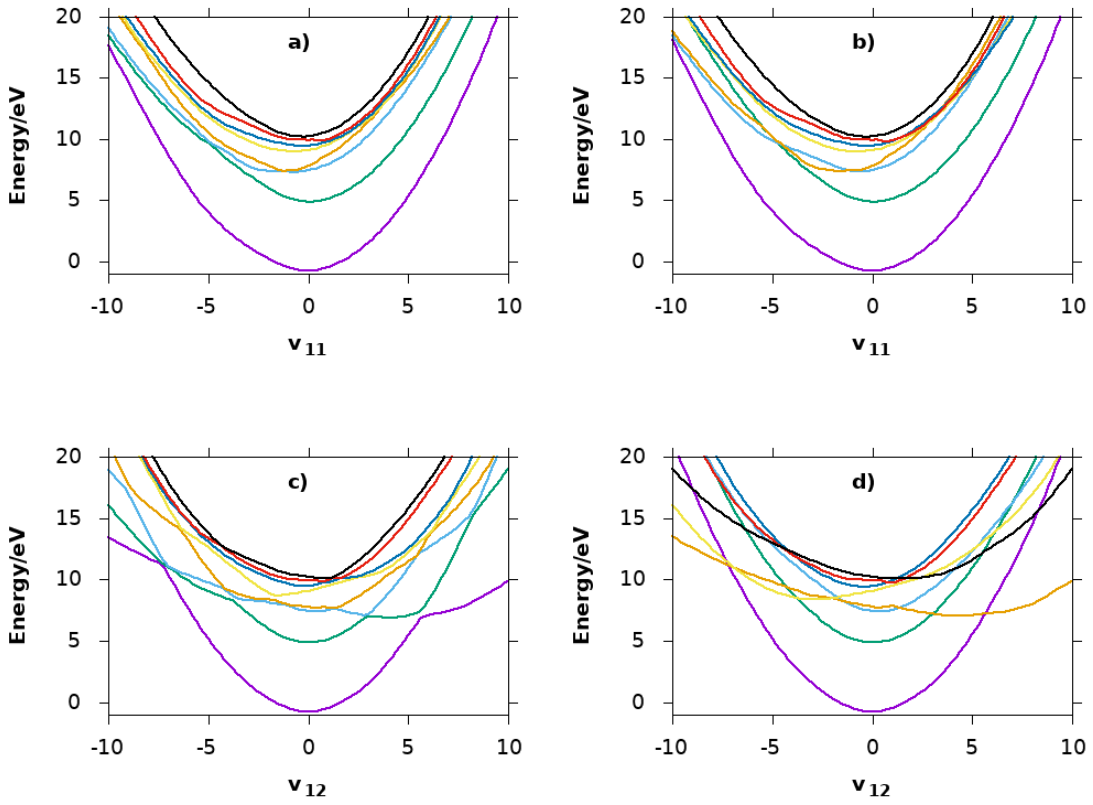

Fig. 4.20: One-dimensional cuts through a) the adiabatic and b) the diabatic potential energy surfaces of formamide along the ν_{11} N-H_2 symmetric stretching mode and c) adiabatic and d) diabatic potential energy surfaces along the ν_{12} N-H_2 antisymmetric stretching mode employing the new developed DD-vMCG implementation.

The normalised diabatic state population as a function of time after excitation into the first excited state S_1 from direct dynamics calculations using both DD-vMCG versions is shown in Fig. 4.21. Employing the local DB the timescale for the decay is faster and compared to the original DD-vMCG implementation where even after 30 fs the higher percentage of the population is still in the S_1 state which is the fully populated first excited state. It is also apparent that the population transfer is quite uniformly distributed across the excited electronic states in the calculation in the case of the original DD-vMCG implementation. However, as seen

in Fig. 4.21(b), at the end of the propagation approximately around 15% of the population has been transferred to the S_3 state in the case of the new DD-vMCG implementation.

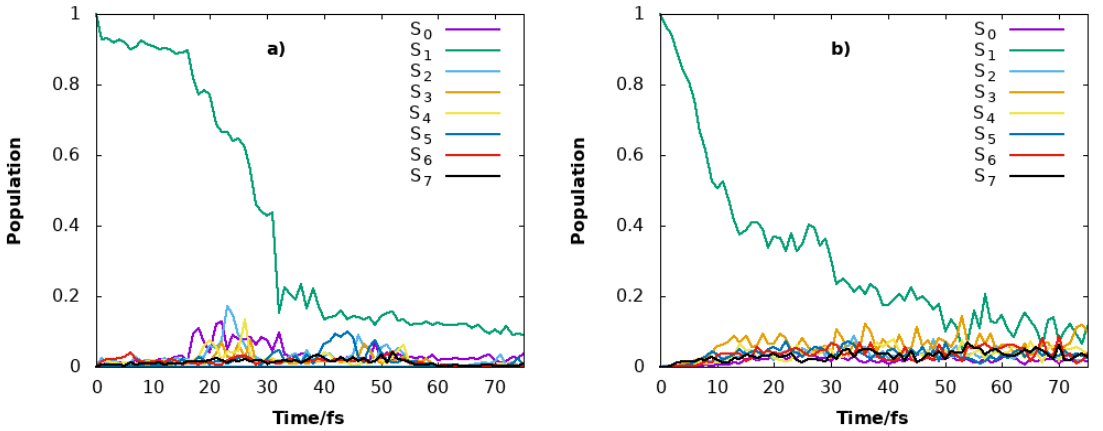

Fig. 4.21: Normalised diabatic state population from DD-vMCG simulations of formamide using a) the original and b) the developed DD-vMCG version: S0: purple; S1: green; S2: light blue; S3: orange; S4: yellow; S5: dark blue; S6: red; S7: black.

To examine the accuracy of the simulation the energy conservation is plotted for formamide for both the original and developed direct dynamics implementations as illustrated in Fig. 4.22. The energy for the original DD-vMCG version is again very poor immediately after the calculation has started and can be attributed to the previously applied interpolation scheme in DD-vMCG. However, as Fig. 4.22(b) depicts, the energy is totally conserved throughout the calculation using the developed interpolation scheme.

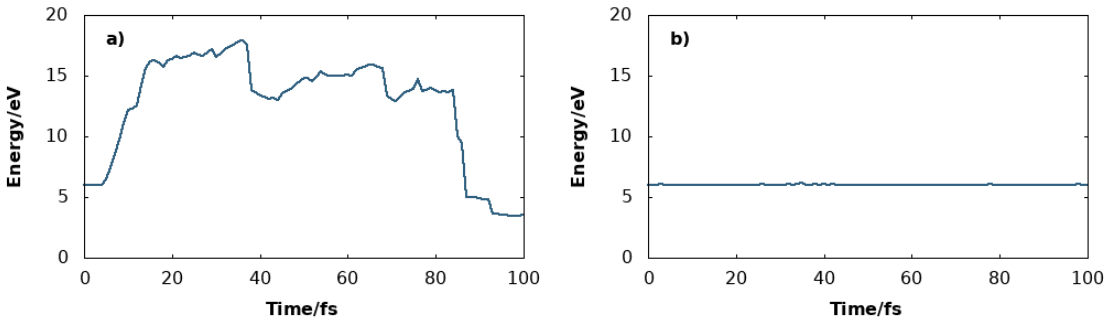

Fig. 4.22: Total energy for formamide as a function of time using a) the original and b) the improved interpolation scheme for direct dynamics.

As with previous test cases, a performance comparison between the local DB

and the full QC database has been conducted where the speedup is examined. During these serial calculations all the variables, such as the number of GWPs (10), the total propagation time, (100 fs) and the n_{conf} (6) have been kept constant. For this example molecule finding the appropriate values for the n_{db} and n_{conf} parameters was not straightforward. Thus, multiple tests that are relatively quick have been conducted to determine the best combination that works for both versions allowing a sensible comparison. For instance, if the number of points included in the local DB are not enough to cover the movements of the GWPs' centres in the configuration space, then the points that will be included in the interpolation will be quite far apart leading to significant integration instabilities, as the integrator takes a large number of t_{small} steps every t_{large}. Therefore, the program will need more time for the same execution than with the full QC database and in some cases will even terminate unexpectedly. Hence, the various dbmin values together with the suitable n_{db} parameter for each case are listed in Table 4.6.

The efficiency results shown in Table 4.6, follow similar patterns to the ones from butatriene and allene cations. Thus, the total elapsed time for all calculations regarding both the local DB and the full QC database versions increases with the number of points in the DB. Moreover, the local database approach is always more efficient compared to the full QC database reaching a speedup of 24 in the last example with 6021 points. Again, the different times needed for a full propagation with various total data points are relatively close to each other when using the local DB. On the other hand, in the case of the full QC database it is again confirmed that dealing with the database dominates the calculation when no new points are added. Additionally, the speedups for formamide are lower compared to the ones from the two previous test molecules. This variation can be explained by considering the higher value of the n_{db} parameter and also the larger full DBs.

Next, direct dynamics calculations were conducted on formamide employing the

Table 4.6: The total elapsed time for serial DD-vMCG calculations with 10 GWPs using the full QC database and local databases, varying the number of points in the QC DB by using different distance criteria (dbmin values). For all calculations the n_{conf} parameter was equal to 6.

Distance criterion	0.25	0.20	0.15	0.10	0.05
n_{db}	20	20	40	40	60
			Number of Data points		
	267	442	715	1496	6021
Full QC DB (sec)	3601	6919	7376	16201	126139
Local DBs (sec)	3001	3145	3207	3522	5234
Speedup	1.2	2.2	2.3	4.6	24.1

local DB approach aiming to compare the sequential with the parallel operation for different numbers of processors. Table 4.7 demonstrates the outcomes for 10 and 20 GWPs focusing on the total time for the calculation and also the time for the code dealing with the DB. The total propagation time, (200 fs), the interpolation confidence radius n_{conf} (6) and the total number of points in the local DBs, $n_{\text{db}} = 60$, have been kept constant.

For both examples with 10 and 20 GWPs the speedup values of the total calculation and the DB code accelerate when switching to parallel operation and with the number of processors, following the same pattern as in the other two test cases. As stated above, the higher value of the n_{db} parameter affects the integration and the dynamics, resulting in similar timing outcomes. In essence, the parallel speedup seems to follow a similar pattern for both examples and a linear scaling is achieved which is in accordance with Amdahl's law.

In this case an effort to better understand the correlation of the DB and the time needed for a full propagation has been made, hence a quite large DB (13516) has been employed for the second case (20 GWPs). Dealing with a very large DB implies that even for the local DB approach some time delays will occur as the refresh of the local DBs for each GWP will take significantly more time than with a smaller total DB. However, it is important to note that still the parallel performance is very efficient since for the 20 GWPs example the parallel operation

Table 4.7: The total wall-clock time for a parallel implementation of DD-vMCG using local DBs, with different number of cores.[1]

	Number of Cores				
	1	5	10	15	20
6021 DB points - 10 GWPs					
Total Calculation					
Total Time (sec)	5234	2492	1377	1414	1416
Parallel Speedup	1.0	2.1	3.8	3.7	3.7
Database code					
Total Time (sec)	3778	1672	990	1000	1001
Parallel Speedup	1.0	2.3	3.8	3.8	3.8
Efficiency	1.0	0.5	0.4	0.3	0.2
13516 DB points - 20 GWPs					
Total Calculation					
Total Time (sec)	22436	9755	7011	6063	4233
Parallel Speedup	1.0	2.3	3.2	3.7	5.3
Database code					
Total Time (sec)	17345	7541	5256	4447	2891
Parallel Speedup	1.0	2.3	3.3	3.9	6.0
Efficiency	1.0	0.5	0.3	0.3	0.3

[1] Performed on a single node with 2 x 10 core Xeon 2.3GHz CPUs

on 20 processors was 6 times faster. For the 10 GWPs case when the number of processors is greater than the number of GWPs the speedup goes down as expected. The efficiency of the parallel operation when treating the same problem decreases with the number of processors as expected but seems to follow a more stable behaviour compared to butatriene and allene.

4.6 Summary

Within this Chapter the conceptual development and its implementation to the direct dynamics variational multi-configurational Gaussian method were presented along with benchmark calculations on three chemical systems. Initially, the interpolation scheme was updated aiming to improve both the efficiency and accuracy of the code.

A parallel algorithm has also been established leading to a developed DD-vMCG method. A detailed comparison between the new developed DD-vMCG

and the original implementation on butatriene cation, allene cation and formamide reveal smoother adiabatic and diabatic potential energy surfaces, better defined population transfers and total energy conservation for all investigated molecules.

Further, the efficiency is examined by performing test calculations employing both the local DB and the full quantum chemistry DB approaches. Outcomes on the three aforementioned molecules showed that the local DB implementation is always significantly faster regardless of the molecule and the initial conditions which overcomes the main bottleneck that DD-vMCG was encountering when treating complex chemical systems. Additionally, the parallel performance is very efficient and particularly when more GWPs were employed the speedups were higher.

On a final note, the newly developed DD-vMCG method has been proved to be a very accurate, efficient and general method to employ in order to perform full-dimensional dynamics calculations on different molecules and it is very promising to move further to higher dimensional investigations.

Chapter 5

Applying DD-vMCG to Study the Photodissociation of Phenol

The work in this study has been submitted for publication in Phys. Chem. Chem. Phys. The electronic structure calculations reported in section 5.4 were conducted by Thierry Tran.

5.1 Introduction

In this chapter, the developed efficient algorithm for the direct dynamics variational multi-configurational Gaussian (DD-vMCG) method (Chapter 4) has been used to describe the multidimensional photodissociation dynamics of phenol including all degrees of freedom. Full-dimensional quantum dynamic calculations including for the first time six electronic states ($^1\pi\pi$, $1^1\pi\pi^*$, $1^1\pi\sigma^*$, $2^1\pi\sigma^*$, $2^1\pi\pi^*$, $3^1\pi\pi^*$) along with a detailed comparison with the existing 4-state model for the potential energy surfaces are presented. The scope of this chapter is twofold. First to explore the applicability of the improved DD-vMCG method which was presented in Chapter 4, and also to add new insights into the photochemistry of phenol.

Initially, a review of the relevant literature on the phenol molecule including the most recent research studies is presented. Exploring the dynamics of phenol with DD-vMCG requires the employment of quantum chemistry programs developed in different studies, as one of the goals is to compare our work with other

research studies. Hence, a new interface that enables the employment of any external molecular potential program by DD-vMCG to calculate the energy and the gradients is described along with an implementation for calculating the Hessian matrix. An in-depth comparison of the different methods and the quantum chemistry programs is also included.

Aiming to investigate the photodissociation, electronic structure calculations were firstly performed, followed by a detailed computational design and testing of the different parameters and initial conditions which should be employed for the chosen methods. DD-vMCG was employed for all the calculations to obtain potential energy surfaces, state populations and dissociation flux.

5.2 Phenol

Amino acids are among the most essential biomolecules. Aromatic amino acids such as phenylalanine, tryptophan and tyrosine have broad UV absorption cross sections. Nevertheless, the fluorescence quantum yield produced from these molecules is quite small. The existence of fast non-radiative processes, that effectively quench the fluorescence is indicated in the literature.[153–156] Other research studies suggested that the non-radiative process is ultrafast internal conversion where the electronic energy turns into vibrational energy.[154–157] Immediately after the internal conversion, through intermolecular energy transfer this vibrational energy is rapidly dissipated from the highly vibrationally excited molecules to the surrounding molecules prior to chemical reactions occurring. The prevention of photochemical reactions upon UV radiation is known as photostability.

Phenol C_6H_5OH is an aromatic organic compound where subject to the orientation and arrangement of the C-$\hat{O}$-H bond with respect to the benzene ring which is planar, phenol demonstrates the following three point group symmetries (Figure 5.1 shows the atom numbering) :

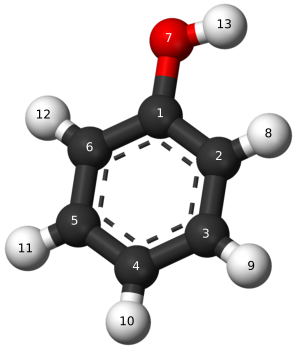

Fig. 5.1: The equilibrium ground state structure of phenol.

- C_{2v} when C1O7H13 is collinear with the C4C1 axis
- $C_{s-planar}$ when C1O7H13 is planar and in the benzene plane
- $C_{s-bijct}$ when C1O7H13 is planar, in a plane perpendicular to the benzene ring and including the C4C1 axis

Phenol is the chromophore of the amino acid tyrosine and a major component of green fluorescent protein chromophores.[158] It has thus been extensively studied from both experimentalists[159–162] and theoreticians.[163–165] The delocalised electrons in the benzene ring interact with one of the oxygen lone pairs, affecting the properties of both the ring and the -OH group. This interaction, effectively a donation of the oxygen lone pair into the ring system, leads to an increase of the electron density around the ring making it much more reactive than in benzene itself. It also results in the hydrogen of the -OH group being a lot more acidic than it is in alcohols. This will be investigated further in the electronic structure section.

Despite the fact that this research study is a purely computational approach, it is important to understand both the role of experimental work and their combination with *ab initio* electronic-structure calculations of excited states and their potential energy surfaces in order to study the photodynamics of phenol in depth. As experimental results and computational quantum chemistry calculations indi-

cate, phenol has a low fluorescence quantum yield attributable to the dissociative character of the electronic excited state potential energy surface, rather than internal conversion to the electronic ground state.[164,166,167] Also, the important coordinates which are fundamentally involved in the dynamics are the O-H distance, the C-Ô-C bond angle and the CCOH torsion angle.

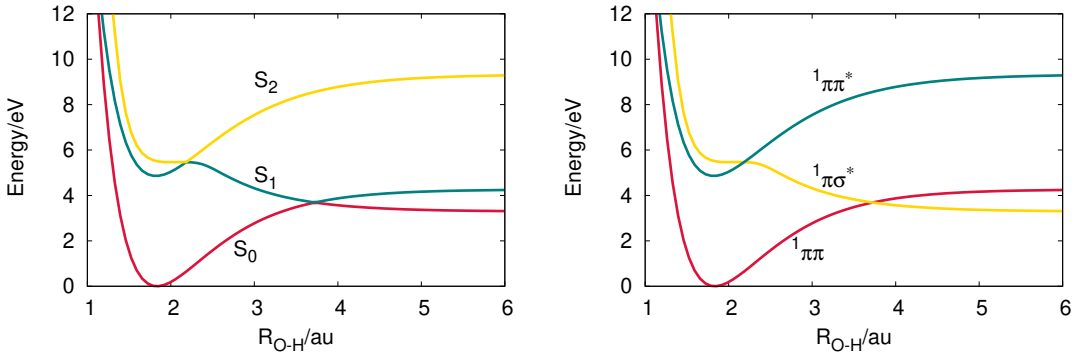

(a) (b)

Fig. 5.2: Potential energy curves of the (a) adiabatic and (b) diabatic picture for the ground and excited singlet states as a function of R, the O-H bond distance.

Furthermore, the PESs change as the O-H bond stretch increases. As shown in Figure 5.2, two conical intersections are observed for the potential energy surfaces of phenol in which the $^1\pi\sigma^*$ state which is a dark repulsive state is involved: one with the $^1\pi\pi^*$ strongly absorbing bound state, and the other with the $^1\pi\pi$ ground state. These conical intersections govern the photodissociation dynamics, determining the reaction pathway and the branching rates of photodissociation products as a function of UV wavelength (λ). The photodissociation dynamics of phenol have been experimentally studied through the relative kinetic energy distribution of photofragments, using techniques such as high-resolution H Rydberg atom translational spectroscopy, multimass ion imaging and time-resolved velocity map ion imaging.[159,160,162,168–172]

The relative kinetic energy distribution of photofragments is bimodal for excitation in the range $279.145 \geq \lambda \geq 193$ nm. Clear resolved peaks with a maximum

at $\sim$ 6000 cm^{-1} can be observed for λ =275.113 nm, attributed by researchers to two possible mechanisms. One is internal conversion to excited vibronic levels of the $^1\pi\pi$ state with the O-H bond stretch as the main accepting mode, followed by dissociation through the $^1\pi\pi/^1\pi\sigma^*$ conical intersection. A quite popular approach suggests the H tunnelling under the $^1\pi\pi^*/^1\pi\sigma^*$ CoI to the $^1\pi\sigma^*$ state is a dissociation pathway for phenol.[173] This is supported by analysis of kinetic energy spectra for excitations of certain vibrational modes of the $^2B_1$ phenoxyl radical.[159–161] The observed active modes, and especially the ν_{16a} ring torsional mode, were deemed responsible for enabling the coupling between the $^1\pi\pi^*$ and $^1\pi\sigma^*$ states. As a result, the energy of S_1 state decreases, making the system more adiabatic and facilitating tunnelling through the barrier on the S_1 surface.[160,174]

On excitation to $\lambda < 248$ nm, the vibrational structures at $\sim$ 6,000 cm^{-1} gradually diminish as the wavelength decreases, while a new set of resolved peaks grows in a region centred around 12,000 cm^{-1}.[173,175] The latter was linked to the very fast dissociation through the $^1\pi\sigma^*$ state which follows passing via the $^1\pi\pi^*$ / $^1\pi\sigma^*$ conical intersection. Moreover, the centre of this set of peaks does not shift as λ is further reduced, but the structure becomes broader and gradually disappears.

An unresolved component is observed in the kinetic energy spectra at lower frequencies (centred at $\sim$ 1,500-2,000 cm^{-1}) and does not significantly change with wavelength.[160,176] This feature arises from unimolecular decay of the S_0 state to H atoms and phenoxyl $^2B_1$ ground state radicals after internal conversion, and from multiphoton processes.[165]

The dissociation lifetime of a molecule like phenol with many vibrational degrees of freedom can span from several hundred nanoseconds to sub second.[177–179] For instance, a dissociation lifetime of 62 μs was experimentally determined[180] for vibrationally excited phenol in the electronic S_0 state, produced by internal conversion after excitation to the first excited state band origin. Increasing the

pumping photon energies leads to a decreased overall lifetime of S_1 at the excited Franck-Condon window (which contains modes orthogonal to the O-H stretch), since the ability for the $S_1 \rightarrow S_0^*$ internal conversion increases. However, an analogous increase of the O-H fission rate is absent for the H transients. Since these only depend on the decay along S_2, there is a strong suggestion that the $S_1 \rightarrow S_0^* \rightarrow S_2 \rightarrow C_6H_5O(\tilde{X}) + H$ dissociation mechanism is inactive.[159]

Employing theoretical methods, Sobolewski and Domcke[181] were the first to introduce the phenol nonadiabatic dissociation pathways. Their innovative work disclosed that since the $^1\pi\sigma^*$ character state, a dark and strongly repulsive state, crosses both the S_1 and S_2 states, the dissociation from the $^1\pi\pi^*$ character state involves two seams of conical intersections. Recently, significant efforts have been made to map out the full-dimensional potential energy surfaces for this system. Three full-dimensional coupled potential energy surfaces were reported[174] employing the anchor-points reactive potential (ARPR) method to a large number of points determined using multi-configuration quasi-degenerate perturbation theory. Moreover, full-dimensional coupled PESs based on multi-reference CISD excitation expansions have been also reported by Zhu, Yarkony and co-workers.[163,182,183] It is worth indicating that atomic tunnelling in molecular systems such as phenol is frequently treated within the BO approximation, defined by a barrier on an adiabatic PES.

5.3 External Molecular Potential Program

Direct dynamics employs various known quantum chemistry programs such as Gaussian09[81] to run either HF or CASSCF calculations, Molpro[141] and Molcas[184] to compute the energies, gradients and Hessian matrices at each point reached by GWPs. However, it is important for DD-vMCG to be a flexible method that gives the opportunity to the user to explore any molecule with any available external

program and also offers unlimited customisation where the user can create a new program or modify an existing one to fit the needs of the molecule under investigation. Hence, the primary step was to develop the existing code by creating a new interface so that the Quantics package can call any available external programs that calculates the energies and gradients for any molecule under investigation and store all the data.

If the Hessians are not provided by the external program they need to be calculated; a flexible method, which can be used for any external program, was developed to determine the Hessian matrix from known gradients. The following proof in which the development of the existing programs was based on to calculate the Hessian is written for simplicity for a three-dimensional system but can be easily extended to higher dimensions.

Let f be a continuous and infinitely differentiable function in some open neighbourhood around $\vec{a} = (x_a, y_a, z_a)$

$$\begin{aligned} f(x,y,z) =& f(x_a,y_a,z_a) + (x-x_a)f_x + (y-y_a)f_y + (z-z_a)f_z + \\ & \frac{1}{2}(x-x_a)^2 f_{xx} + \frac{1}{2}(y-y_a)^2 f_{yy} + \frac{1}{2}(z-z_a)^2 f_{zz} + \\ & (x-x_a)(y-y_a)f_{xy} + (x-x_a)(z-z_a)f_{xz} + (y-y_a)(z-z_a)f_{yz} + ... \end{aligned} \tag{5.1}$$

where

$$f_x = \left.\frac{\partial f}{\partial x}\right|_a \quad , \quad f_{xx} = \left.\frac{\partial^2 f}{\partial x^2}\right|_a \quad \text{and} \quad f_{xy} = \left.\frac{\partial^2 f}{\partial x \partial y}\right|_a = f_{yx} \tag{5.2}$$

likewise f_y, f_z, f_{xz} and f_{yz} can be defined.

The first derivative of function f from Eq. 5.1 with respect to x, y and z can be written as follows

$$\frac{\partial f(x,y,z)}{\partial x} = f_x + (x-x_a)f_{xx} + (y-y_a)f_{xy} + (z-z_a)f_{xz} + ... \tag{5.3}$$

$$\frac{\partial f(x,y,z)}{\partial y} = f_y + (y-y_a)f_{yy} + (x-x_a)f_{xy} + (z-z_a)f_{yz} + ... \tag{5.4}$$

$$\frac{\partial f(x,y,z)}{\partial z} = f_z + (z-z_a)f_{zz} + (y-y_a)f_{zy} + (x-x_a)f_{yz} + ... \tag{5.5}$$

Taking Eq. 5.3 about the points $(x_a + h, y_a, z_a)$ and $(x_a - h, y_a, z_a)$ where h is a real step

$$\frac{\partial f(x_a + h, y_a, z_a)}{\partial x} = f_x + h f_{xx} + O(h) \tag{5.6}$$

$$\frac{\partial f(x_a - h, y_a, z_a)}{\partial x} = f_x - h f_{xx} + O(h) \tag{5.7}$$

where O(h) is the truncation error and the subtractive cancellation error that affect these derivative approximations. Then if we subtract Eq. 5.6 and Eq. 5.7

$$f_{xx} = \frac{1}{2}\left[\frac{\partial f(x_a + h, y_a, z_a)}{\partial x} - \frac{\partial f(x_a - h, y_a, z_a)}{\partial x}\right] + O(h^2) \tag{5.8}$$

$O(h^2)$ is again the error of the approximation but in this case has a smaller value. Likewise f_{yy} and f_{zz} can be defined.

$$f_{yy} = \frac{1}{2}\left[\frac{\partial f(x_a, y_a + h, z_a)}{\partial y} - \frac{\partial f(x_a, y_a - h, z_a)}{\partial y}\right] + O(h^2) \tag{5.9}$$

$$f_{zz} = \frac{1}{2}\left[\frac{\partial f(x_a, y_a, z_a + h)}{\partial z} - \frac{\partial f(x_a, y_a, z_a - h)}{\partial z}\right] + O(h^2) \tag{5.10}$$

If we take again Eq. 5.3 but now about the point $(x_a, y_a + h, z_a)$ and $(x_a, y_a - h, z_a)$

$$\frac{\partial f(x_a, y_a + h, z_a)}{\partial x} = f_x + h f_{xy} + O(h) \tag{5.11}$$

$$\frac{\partial f(x_a, y_a - h, z_a)}{\partial x} = f_x - h f_{xy} + O(h) \tag{5.12}$$

Then by subtracting 5.11 and Eq. 5.12

$$f_{xy} = \frac{1}{2}\left[\frac{\partial f(x_a, y_a + h, z_a)}{\partial x} - \frac{\partial f(x_a, y_a - h, z_a)}{\partial x}\right] + O(h^2) \tag{5.13}$$

In the same way

$$f_{xz} = \frac{1}{2}\left[\frac{\partial f(x_a, y_a, z_a + h)}{\partial x} - \frac{\partial f(x_a, y_a, z_a - h)}{\partial x}\right] + O(h^2) \tag{5.14}$$

$$f_{yz} = \frac{1}{2}\left[\frac{\partial f(x_a, y_a + h, z_a)}{\partial z} - \frac{\partial f(x_a, y_a - h, z_a)}{\partial z}\right] + O(h^2) \tag{5.15}$$

Therefore all the second derivatives, Hessians, can be obtained if first derivatives can be calculated at the required points. This scheme to obtain Hessians

was tested in different functions with known derivatives for various points and it was proved accurate. It has been found that setting $h = 1 \times 10^{-5}$ yields the best results.

5.4 Electronic structure and geometry optimisations

For the definition of the normal mode displacement, the optimization of the ground state S_0 geometry and the frequency calculation were carried out with state-average CASSCF/6-311+G** level of theory with an active space of 10 electrons in 10 orbitals as depicted in Fig. 5.3. The active space comprises of the one oxygen lone pair, three π, three π^*, one $3s$ and the O-H σ and σ^* orbitals. The choice of CASSCF was based on several criteria. Firstly, the need to be able to calculate energies at ground and excited states, and be applicable to scans along normal modes to create PESs. Given the non-adiabaticity observed in the excited states, a method with multireference description is desirable. This is even more essential if the surfaces cross. The analytical energy gradients available for CASSCF allow crossing points to be located and derivative couplings to be calculated. CASSCF provides qualitatively correct energies and allows a reasonable model to be built without the need to resort to more demanding levels of theory. All electronic structure calculations were run using the OpenMolcas program.[184]

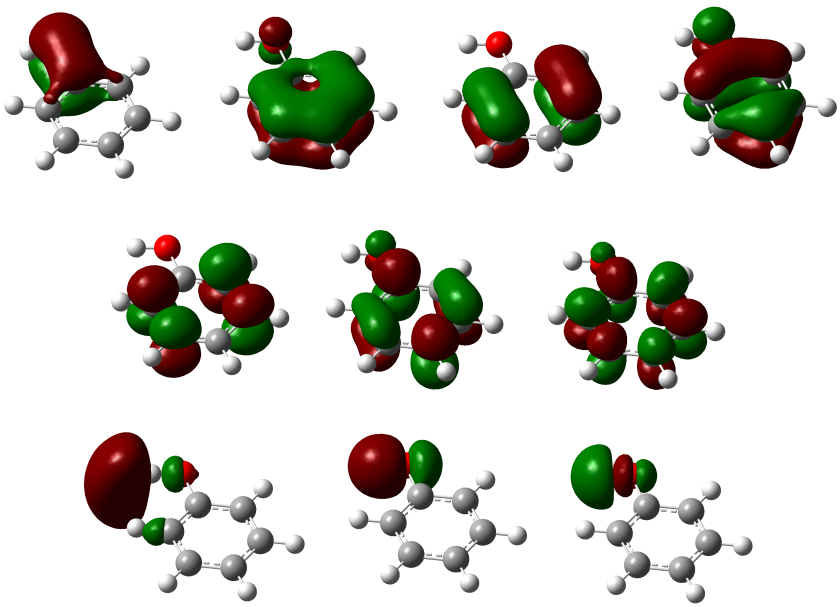

Fig. 5.3: Molecular orbitals used for the CASSCF calculation with phenol for the 10 electrons in 10 orbitals.

5.5 Computational Details

5.5.1 DD-vMCG Protocol

All the nuclear dynamics calculations were carried out using the DD-vMCG implementation in the QUANTICS package.[21] To investigate the phenol molecule, potential energy surfaces were generated where the calculations were performed for a state-average of up to 6 states with the ground (S_0) and the first excited states (S_1 - S_5), including all degrees of freedom. For all the calculations OpenMolcas[184] at a CASSCF(10,10)/6-311+Gpp level of theory was employed as the external quantum chemistry program. The initial wavepacket was a Gaussian function of width $1/\sqrt{2}$ along all normal coordinates. An initial calculation was conducted with a vertical excitation to the first excited state using 20 Gaussian basis functions, with a propagation time of 200 fs with data output every 0.5 fs.

In addition, direct dynamics calculations were also carried out employing the potential energy surface model for phenol from Zhu and Yarkony[163,182,183] (PES_{ZY}) which is a full dimensional four states scheme and also the Xu, Zheng, Yang and

Truhlar[174,185,186] model (PES_{XZYT}) which incorporates three states, as external molecular potential programs. For dynamics employing the PESzy external program, the molecule geometry had to be re-optimized by aligning the molecule in the XZ plane employing the state average CASSCF(10,10)/6-311+G(pp) level of theory with three states. In this research work, four full-dimensional coupled PESs based on multi-reference configuration interaction single and double CISD excitation expansions are reported. The various parameters used in these DD-vMCG calculations along with the level of theory have been kept the same as before with the OpenMolcas propagation and therefore a sensible comparison can be made.

Initially, for all the calculations presented here, a direct dynamics run was conducted with an empty database and then a second propagation with the same initial conditions but with the database from the first propagation was carried out. Considering a direct dynamics propagation with only one GWP that reaches multiple times the same point in the configuration space, each time the database is different as it is built *on-the-fly* and therefore the extrapolated potential will not be the same. Hence, to get the best representation of the dynamics, multiple propagations were performed until no new points were added to the database. The former process of re-running a calculation aiming to add more points in the database is a key feature of DD-vMCG. As a next step, the final propagation will use this database to read all required information, energy, gradients and Hessian at each step which requires less computational effort than running expensive quantum chemistry calculations. For all the aforementioned re-runs of the same DD-vMCG calculation the new efficient algorithm of Chapter 4 was employed which uses a local dynamic version of the full database for each GWP each time the code needs to read, sort and analyse the database. In the following analysis the results of this final set of calculations were employed.

5.5.2 Complex Absorbing Potential (CAP) and Flux Operator

After analysis of the initial phenol results, complex absorbing potentials (CAPs) were selected and employed. In grid based methods like MCTDH, a CAP is defined as a negative, imaginary potential which absorbs the parts of the wavepacket reaching the end of the grid and hence the reflection of the wavepacket is avoided.[187,188] In DD-vMCG, CAPs are used as a cut-off point to the dissociative motion along normal mode coordinates. More specifically, upon a rapid dissociation, the dissociating atom obtains momentum as it moves further apart from the molecule. As a result, the integrator will quickly decrease the size of the time step that enables an accurate description of the overall system. These rapidly changing geometries will additionally lead into the need for electronic structure calculations for substantially more points. These calculations, at widely spaced geometries, will require much more time, and may eventually fail. The CAPs are defined as

$$-i\eta W(x) = -i\eta(k(x-x_0))^n\Theta(x-x_0) \tag{5.16}$$

where W(x) denotes a real low order monomial, η is the strength, n is the order, $k = \pm 1$ denotes the direction (positive or negative) of the CAP positioned at x_0 along a normal mode coordinate and Θ is a step function. The modification of the Hamiltonian in this way means that it is non-Hermitian and the norm is not conserved, i.e. the norm will decrease upon the entrance of the wavefunction in the CAP region. The dependence of the norm on the Hamiltonian can be expressed as follows

$$\begin{aligned}\frac{d}{dt}\left\|\Psi\right\|^2 = \frac{d}{dt}\left\langle\Psi|\Psi\right\rangle = \left\langle\dot{\Psi}|\Psi\right\rangle = \left\langle\Psi|\dot{\Psi}\right\rangle \\ = \left\langle -iH\Psi|\Psi\right\rangle + \left\langle\Psi| - iH\Psi\right\rangle = i\left\langle\Psi|H^\dagger - H|\Psi\right\rangle\end{aligned} \tag{5.17}$$

when $\hat{H}$ is Hermitian, the norm is conserved, but when $\hat{H} = \hat{H}_0 - i\eta W(x)$

$$\frac{d}{dt}\left\|\Psi\right\|^2 = 2\left\|\Psi\right\| \cdot \frac{d}{dt}\left\|\Psi\right\| = -2\eta\left\langle\Psi|W|\Psi\right\rangle \tag{5.18}$$

Thus

$$\frac{d}{dt}\|\Psi\| = -\eta\frac{\langle\Psi|W|\Psi\rangle}{\|\Psi\|} \tag{5.19}$$

with the more compact solution

$$\|\Psi(t)\| \propto e^{-\eta W}\|\Psi(0)\| \tag{5.20}$$

Once the CAP is reached by the Gaussian, the motion is set to continue classically and stops when the population of the Gaussian becomes zero. For this study, the values of $x_0 = 10$, $\eta = 0.1$, $n = 3$, $k = 1$ were selected along the ν_{33} which is the O-H stretch mode.

Moreover, the flux operator is also calculated to evaluate the probability density change rate over some arbitrary subspace. If Θ denotes a Heaviside step function projecting onto the sub-space of interest, then the flux has the following form

$$\begin{aligned}\hat{F} &= \frac{\partial}{\partial t}\langle\Psi|\Theta|\Psi\rangle = \left\langle\Psi|\Theta|\dot{\Psi}\right\rangle + \left\langle\dot{\Psi}|\Theta|\Psi\right\rangle \\ &= -i\langle\Psi|\Theta H|\Psi\rangle + i\langle\Psi|H\Theta|\Psi\rangle = i\langle\Psi|[H,\Theta]|\Psi\rangle\end{aligned} \tag{5.21}$$

The flux through a channel for a Hamiltonian with a CAP determining the channel can be obtained as follows

$$\hat{F} = i[H,\Theta] = i[H_0 - iW,\Theta] = i(H_0\Theta - \Theta H_0) + 2W \tag{5.22}$$

Thus the total flux into the channel can be written as

$$\int_0^\infty dt\left\langle\Psi|\hat{F}|\Psi\right\rangle = \int_0^\infty dti\langle\Psi|[H,\Theta]|\Psi\rangle + 2\int_0^\infty dt\langle\Psi|W|\Psi\rangle \tag{5.23}$$

Considering the following

$$\int_0^\infty dt\langle\Psi|\Theta|\Psi\rangle = \langle\Psi(\infty)|\Theta|\Psi(\infty)\rangle - \langle\Psi(0)|\Theta|\Psi(0)\rangle = 0 \tag{5.24}$$

Eq. 5.23 can be simplified and hence the total flux has the following form

$$\int_0^\infty dt\left\langle\Psi|\hat{F}|\Psi\right\rangle = 2\int_0^\infty dt\langle\Psi|W|\Psi\rangle \tag{5.25}$$

and can be obtained by integrating the expectation value of the CAP.

5.6 Quantum Dynamics Calculations

In this section, the results from the computational study of up to 6-state photodissociation of the phenol molecule by employing DD-vMCG including all degrees of freedom is presented. The diabatic and adiabatic potential energy surfaces, and also the conical intersections have been calculated and characterised along the O-H bond stretch (Fig. 5.4(a)) which corresponds to the ν_{33} vibrational mode, the C-$\hat{O}$-C bend angle which corresponds to the ν_{24} vibrational mode (Fig. 5.4(b)) and the CCOH torsion angle which corresponds to the ν_2 vibrational mode (Fig. 5.4(c)) as evaluated at a CASSCF/6-311+G** level of theory. Additionally, the diabatic state populations and the integrated flux is employed to unravel the decay pathways of phenol.

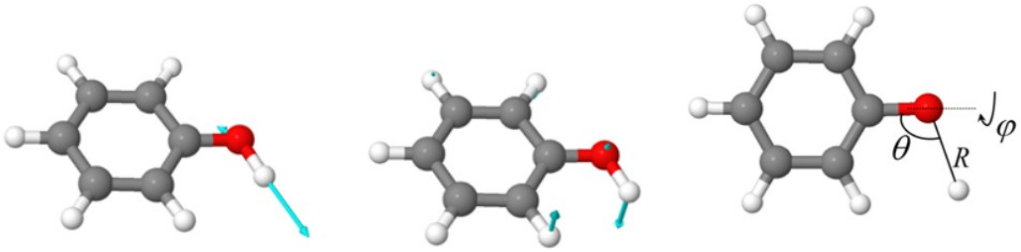

(a) O-H bond stretch (b) *C*-$\hat{O}$-*H* bend angle (c) CCOH torsion

Fig. 5.4: The three main coordinates of phenol accompanied with the associated normal modes during the DD-vMCG propagation. Reprinted with permission from Xie, C.; Ma, J.; Zhu, X.; Yarkony, D. R.; Xie, D.; Guo, H. *J. Am. Chem. Soc.* **2016**, 138, 7828–7831. Copyright 2016 American Chemical Society.

5.6.1 Potential Energy Surfaces

Initially, a computational study including three states to describe the phenol photodissociation was performed by employing the DD-vMCG method including all degrees of freedom. This is the model that has been widely and most commonly employed to study the dynamics of phenol. Here, the Xu, Zheng, Yang and Truhlar[174,185,186] scheme (PES_{XZYT}) and OpenMolcas have been employed as external programs for computing the energies, gradients and Hessians. Fig. 5.5(a) and Fig.

5.5(b) show the adiabatic and diabatic potential energy surfaces along the O-H stretching coordinate generated from the direct dynamics calculation using OpenMolcas. The 3-state model incorporates the two main conical intersections which are both experimentally and theoretically proven to be responsible for the photo-induced hydrogen elimination reaction in phenol but are not properly described. It is worth noting that it was computationally harder to run 3-state direct dynamics calculations, as it was difficult to converge and it was taking more integration steps compared to the four-state calculations.

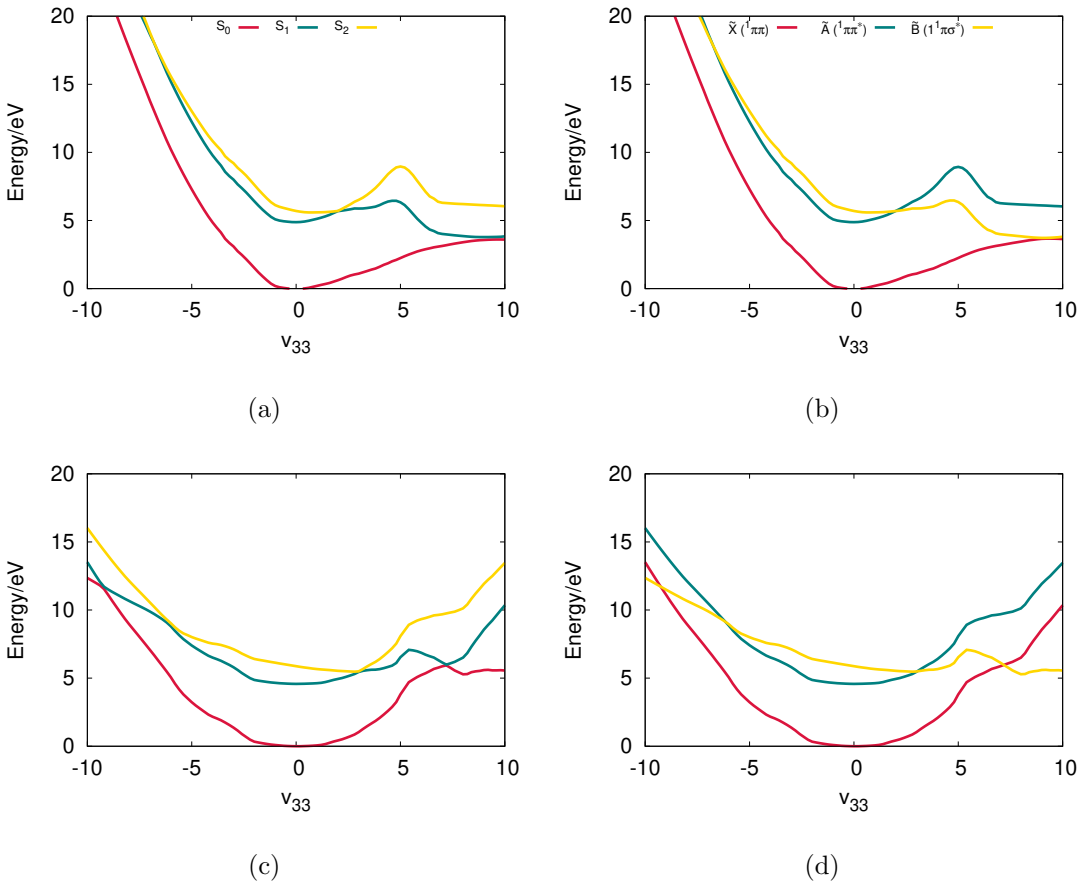

Fig. 5.5: Cuts through the potential energy surfaces of phenol obtained from a DD-vMCG simulation employing OpenMolcas with a three states averaging, (a) adiabatic and (b) diabatic, and employing the 3-state PES$_{XZYT}$ model for phenol as the external quantum chemistry program, (c) adiabatic and (d) diabatic, in the space of the O-H bond stretch, ν_{33}, normal mode. All other coordinates have a value of zero.

The diabatic potentials consist of the ground state ($\tilde{X}$) and two singlet excited states. The first singlet state ($\tilde{A}$) has a $\pi\pi^*$ character and is bound along the O-H stretching coordinate, and the second ($\tilde{B}$) state has a $\pi\sigma^*$ character and is dissociative along the O-H stretching coordinate. The corresponding diabatic potentials in Fig. 5.5(b) include two conical intersections. As expected, the first crossing is occurring when the first excited $1^1\pi\pi^*$ character state crosses the strongly repulsive with respect to the O-H bond $^1\pi\sigma^*$ state. Transfer of the population from the bright state to the dark state can be possible through this conical intersection. Furthermore, at larger O-H distance, a second conical intersection is occurring when the repulsive state, $^1\pi\sigma^*$, crosses the $^1\pi\pi$ ground state. The role of this conical intersections in the photodissociation of phenol has been extensively studied as it has a great impact on the probabilities of transitions.[186]

Moving to the surfaces of the PES$_{XZYT}$ model, again the two important conical intersections are present as described above. Despite the fact that running DD-vMCG calculations was very efficient, the PESs have some fluctuations and also the S_1 and S_2 states in the adiabatic representation (Fig. 5.5(c)), which in the diabatic representation (Fig. 5.5(d)) become the $\tilde{A}$ (green line) and $\tilde{X}$ (red line) respectively, are at high energy levels at the end of the propagation while a flatter shape such as the one of the remaining state and the ones in Figs. 5.5(a) and 5.5(b) would be expected showing the dissociation. The energy levels and the overall shape of the PESs are in good agreement with the ones presented in various papers[174,185,186] employing the PES$_{XZYT}$ model.

Taking advantage of the flexibility the DD-vMCG method offers, a 4-state problem was then selected to examine the photodissociation of phenol. During this research work the number of the excited states included in the quantum dynamical simulations is of great interest as it can reveal important information about the photochemical dissociation of phenol. In this case, the Zhu and Yarkony[163,182,183]

scheme and OpenMolcas have been employed as external programs for computing the adiabatic energies, gradients and Hessians.

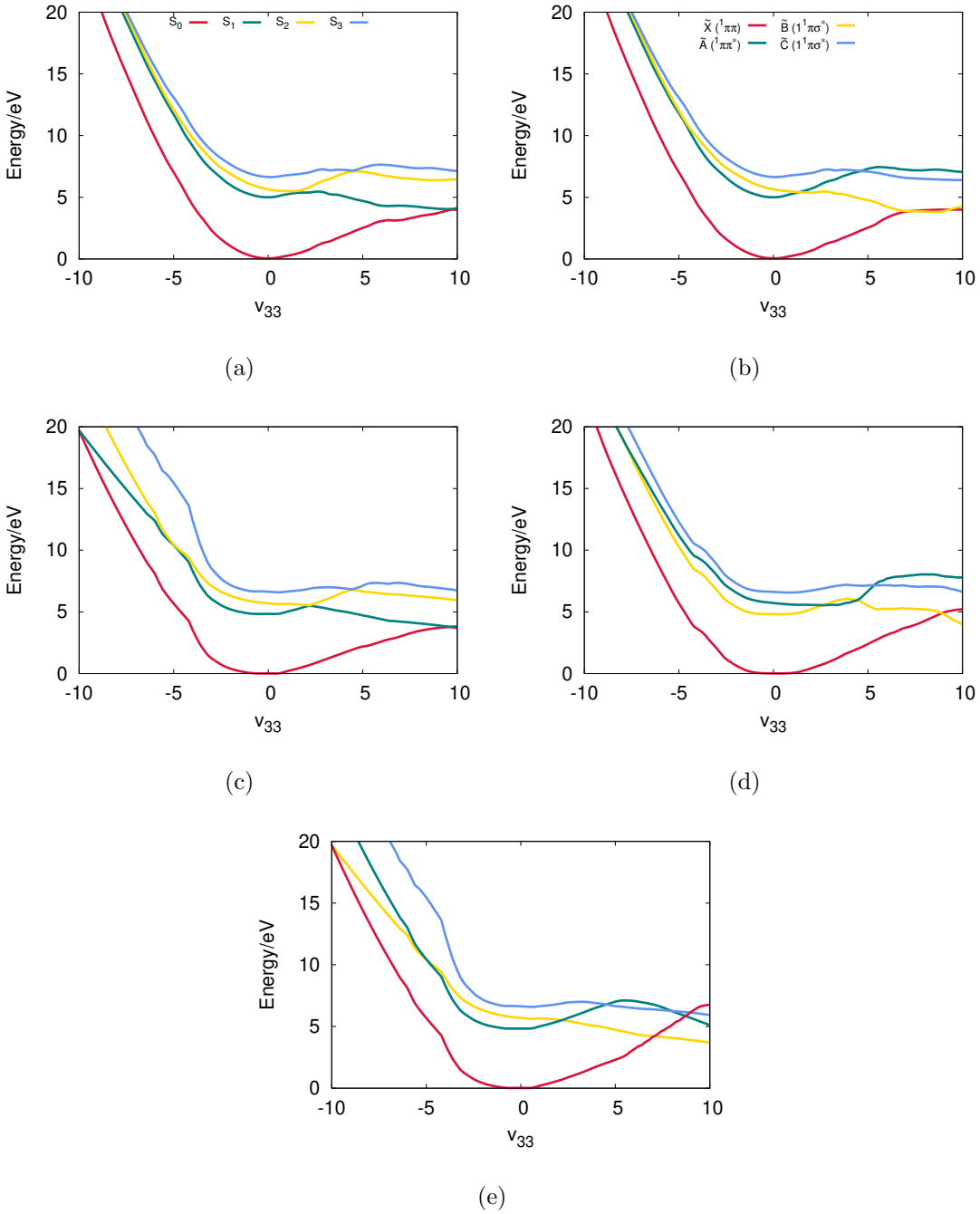

Fig. 5.6: Cuts through the potential energy surfaces of phenol obtained from a DD-vMCG simulation employing OpenMolcas with a four states averaging, (a) adiabatic and (b) diabatic, and employing the 4-state PES$_{ZY}$ program as the external program, (c) adiabatic and (d) diabatic, and obtained directly from the diabatic representation generated by the PES$_{ZY}$ program (e) diabatic, in the space of the O-H bond stretch, ν_{33}, normal mode. All other coordinates have a value of zero.

Fig. 5.6(a) and Fig. 5.6(b) show the adiabatic and diabatic potential energy surfaces along the O-H stretching coordinate generated from the direct dynamics calculation using OpenMolcas. The surfaces are very smooth with well defined CoIs. The additional third ($\tilde{C}$) state, has a $\pi\sigma^*$ character and is dissociative along the O-H stretching coordinate. The corresponding diabatic potentials in Fig. 5.6(b) include three CoIs. An additional CoI between the third repulsive excited $^1\pi\sigma^*$ state and the first $1^1\pi\pi^*$ state is taking place in this 4-state model which will be proved to be crucial for the dissociation of phenol.

Comparing these results with the ones obtained by employing the PES$_{ZY}$ model, the adiabatic surfaces as shown in Fig. 5.6(c) are a good match also to those presented in the Zhu et al.[163] paper. All the conical intersections, S_2/S_1, S_3/S_2 and S_1/S_0, are found at the same positions. However, the diabatic surfaces generated using the diabatisation scheme of the DD-vMCG method as shown in Fig. 5.6(d), are not matching the ones in the paper and thus new calculations were run where the potential energy matrix elements are obtained directly from the diabatic representation generated by the PES$_{ZY}$ program (Fig. 5.6(e)). One major difference here is that the diabatic potential energy surfaces employing the PES$_{ZY}$ model (Fig. 5.6(e)) present multiple conical intersections along the ν_{33} coordinate and especially the ground state that crosses all the excited states. The differences here depend on how the couplings are defined and connected and also on the shifting approach that has been followed in the PES$_{ZY}$ model to match experimental data. More specifically, during the construction of the analytical potential energy surfaces in the PES$_{ZY}$ model, the diabatic potential energy functions were forced to match the experimental data by shifting down in energy both the $\tilde{A}$ and $\tilde{B}$ diabatic states. DD-vMCG offers a more flexible and general picture of the PESs of phenol. Thus, employing a quantum chemistry program to address this complicated problem, is a much more efficient approach which matches the

accuracy of this well constructed analytical potential energy surfaces model for the adiabatic picture.

Including more states during direct dynamics calculations is vital not only to understand the behaviour, such as the possible conical intersections of these particular states, but also to better define the target states such as the S_0, S_1 and S_2 for the phenol molecule. The adiabatic (Fig. 5.7(c)) and diabatic (Fig. 5.7(d)) cuts of the five lowest potential energy surfaces of phenol along the ν_{33} normal mode are shown, characterised as the O-H stretching mode. Here the extra state ($\tilde{D}$) has a $\pi\pi^*$ character and is thus bound to the O-H coordinate. The target states along with their conical intersections are well defined, yet the S_4 state unexpectedly crosses both the S_3 and S_2 multiple times. As a final step and to better understand the effect of the fifth state, another state has been added ($\tilde{E}$) with a $\pi\pi^*$ character which is again bound to the O-H coordinate (Figs. 5.7(a) and 5.7(b)). Smooth potential energy surfaces are observed, with the diabatic states crossing between states as expected. We can observe here that the shape of the lower three states is affected by adding more states.

Fig. 5.8 shows the adiabatic and diabatic potential energy surfaces in terms of the vibrational mode closest to the C-Ô-C bond angle. Comparing both the adiabatic (Figs. 5.8(g), 5.8(e), 5.8(c) and 5.8(a)) and the diabatic (Figs. 5.8(h), 5.8(f), 5.9(d) and 5.8(b)) potential energy surfaces of the ν_{24} normal mode, it can be noted that the surfaces are quite smooth apart from the 5-state model. However, the 6-state approach is the smoothest with very well defined conical intersections. It is, however, difficult to unravel the role of the C-Ô-C bond angle in the dissociation of phenol via the S_1/S_2 conical intersection in these calculations as it can be associated to more than one mode where also activity from other parts of the molecule is involved.

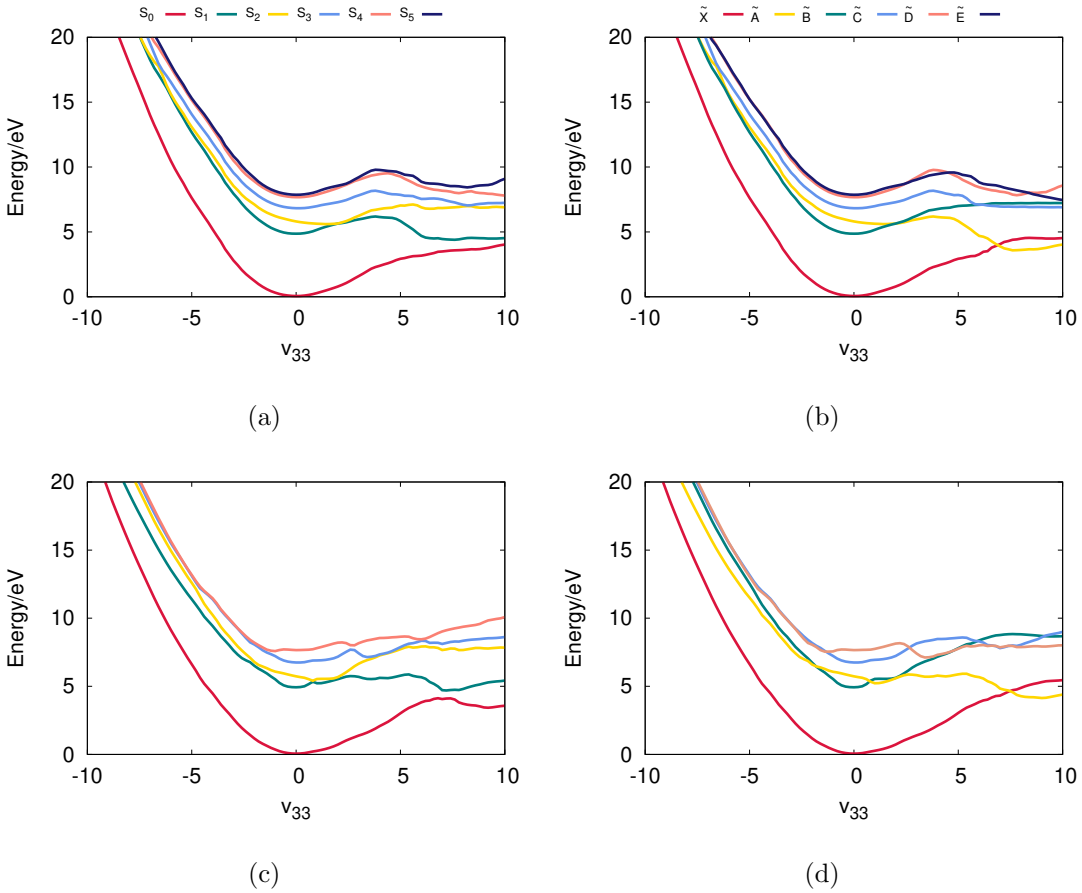

Fig. 5.7: Cuts through the (a,c) adiabatic and (b,d) diabatic 6- and 5-state potential energy surfaces, in the space of the O-H bond stretch, ν_{33}, normal mode employing DD-vMCG method with OpenMolcas. All other coordinates have a value of zero.

In the case of the CCOH torsion coordinate, the ν_2 mode describes a linear approximation to the rotation of the bond, thus the PESs are expected to be symmetrical. As depicted in Fig. 5.9, by employing the different state models, PESs are reasonably symmetrical apart from the case of the 5-state model where again in the PESs a lot of fluctuations are seen. Furthermore, it is important to note that the ν_2 mode does not follow the expected behaviour of a torsional mode where the torsional potential, due to the rotation of bonds is periodic. The explanation lies in the strong coupling between the torsional mode with the stretching mode which also explains the very high and steep potential for the ν_2 mode.

Again, as depicted in Fig. 5.6, when only three states were used to describe the dynamics of phenol, quite poor results were generated with only a narrow well.

Table 5.1: Summary of state characters and symmetries (in C_s) and comparison of experimental and theoretical excitation energy (in eV) with those obtained by employing a CASSCF(10,10)/6-311+Gpp level of theory at the Franck–Condon point and for different state-averaging.

St. Ave.	St.	Char.	Sym.	ΔE	Exp.	Theo.
3 states	S_1	$\pi\pi^*$	A'	4.90	4.51[189]/4.58[190]	4.82[191]/4.85[192] /4.86[161]
	S_2	$\pi\sigma^*$	A"	5.72	5.12[189]	5.37[161]/5.48[192] /5.70[191]
4 states	S_1	$\pi\pi^*$	A'	4.95	4.51/4.58	4.82-4.86
	S_2	$\pi\sigma^*$	A"	5.59	5.12	5.37-5.70
	S_3	$\pi\sigma^*$	A"	6.59	6.42[193]	
5 states	S_1	$\pi\pi^*$	A'	4.86	4.51/4.58	4.82-4.86
	S_2	$\pi\sigma^*$	A"	5.74	5.12	5.37-5.70
	S_3	$\pi\sigma^*$	A"	6.68	6.42	
	S_4	$\pi\pi^*$	A'	7.59		
6 states	S_1	$\pi\pi^*$	A'	4.80	4.51/4.58	4.82-4.86
	S_2	$\pi\sigma^*$	A"	5.67	5.12	5.37-5.70
	S_3	$\pi\sigma^*$	A"	6.56	6.42	
	S_4	$\pi\pi^*$	A'	7.61		
	S_5	$\pi\pi^*$	A'	7.80		

Overall, from a practical perspective both Fig. 5.8 and Fig. 5.9 offer a chance to compare the different state models that have been employed during this study and also to further examine the accuracy of the DD-vMCG propagation when a more complex molecule like phenol is used.

Finally, a comparison of the vertical excitation energies obtained in this study by employing a CASSCF(10,10)/6-311+Gpp level of theory at the Franck–Condon point and for different state-averaging with those in prior experimental[189,190] and theoretical studies[161,191–193] is presented in Table 5.1. The calculated energies are in agreement with the theoretical results and a quite good match with the experimental values. Theoretical results that have a better agreement with experimental can be achieved with energy optimisation.[161] For the different state models presented

in this comparison, the 6-state model yields the closest values to the experimental data available.

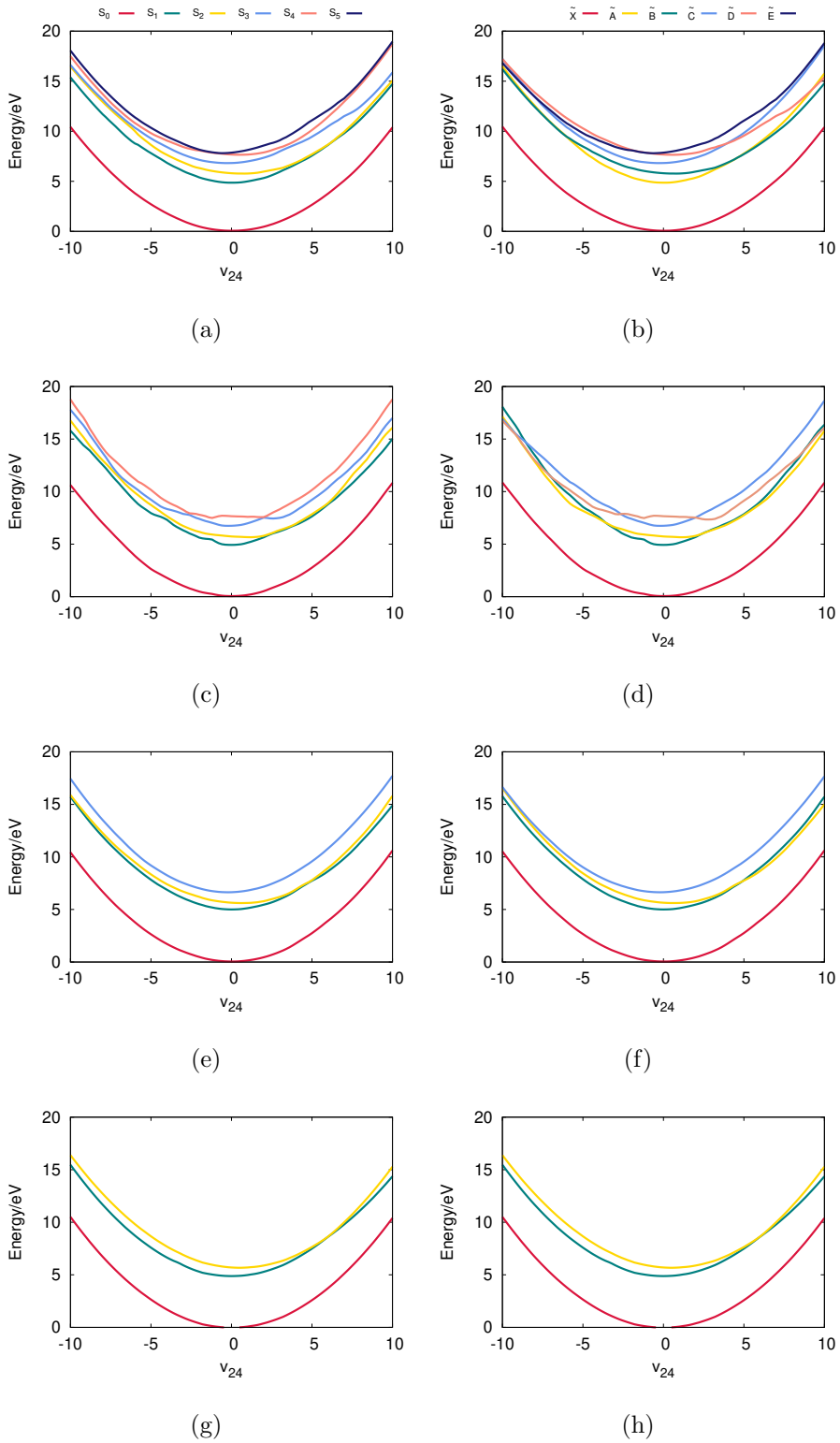

Fig. 5.8: Cuts through the (a,c,e,g) adiabatic and (b,d,f,h) diabatic 6-, 5-, 4- and 3-state potential energy surfaces, in the space of the C-Ô-C bond angle, ν_{24}, normal mode employing DD-vMCG with OpenMolcas. All other coordinates have a value of zero.

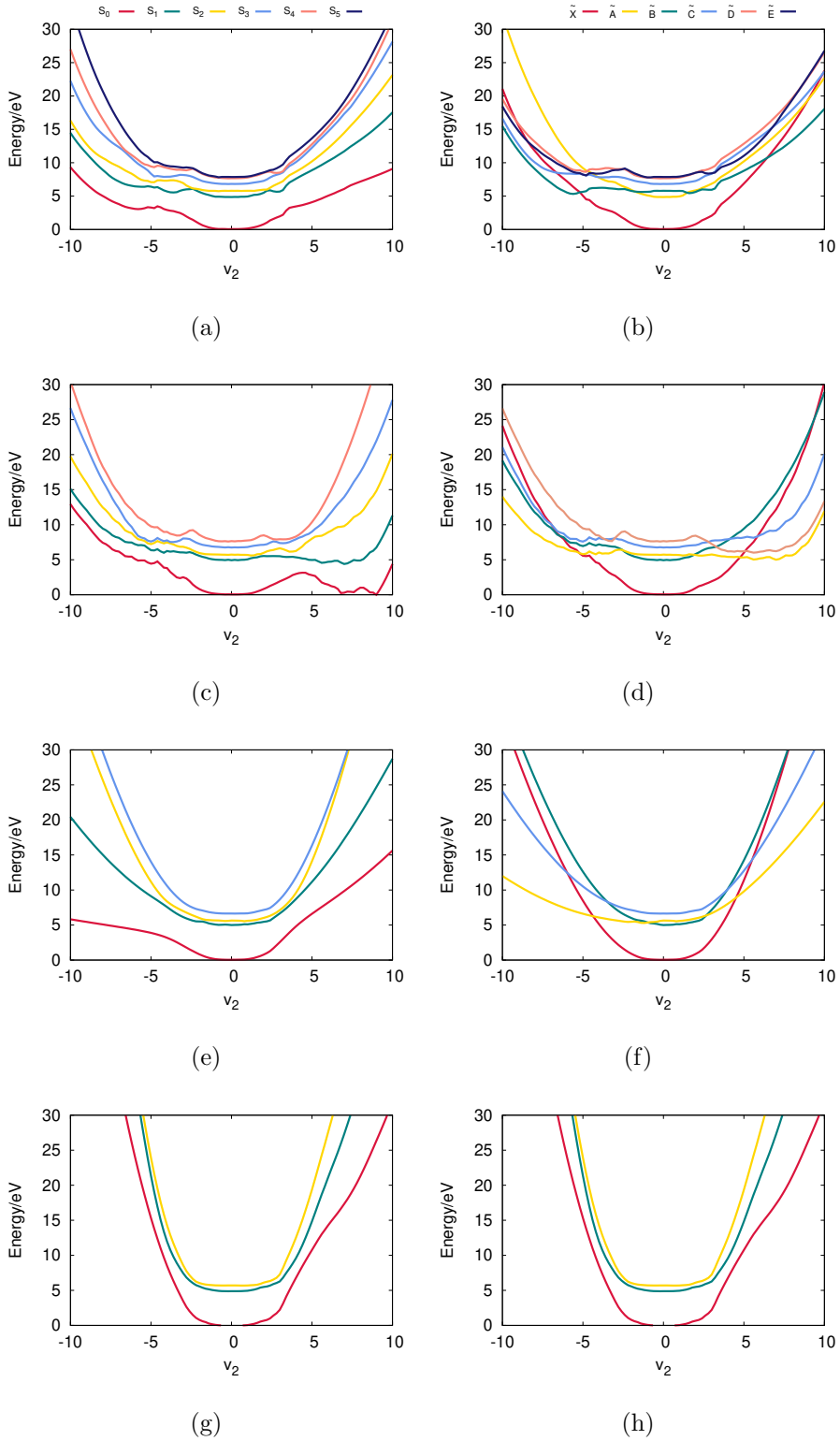

Fig. 5.9: Cuts through the (a,c,e,g) adiabatic and (b,d,f,h) diabatic 6-, 5-, 4- and 3-state potential energy surfaces, in the space of the CCOH torsion, ν_2, normal mode employing DD-vMCG with OpenMolcas. All other coordinates have a value of zero.

5.6.2 State Population Analysis

Studying the state populations sheds light on how the total wavepacket is distributed, into the different states included in the calculation during the propagation period. Here, the diabatic state populations as a function of time for the phenol molecule are presented, after vertical excitation to the $\tilde{A}$, $\tilde{B}$, $\tilde{C}$, $\tilde{D}$ and $\tilde{E}$ states for the 3-, 4-, 5- and 6-state models. The thick black line in all the population figures corresponds to the total density which reveals the percentage of the dissociation. Also, the strong dissociative behaviour of the $\pi\sigma^*$ state is displayed in all the different state averaging models used in this study for phenol apart from the 3-state model.

The populations for the 3-state model after excitation to the $\tilde{A}$ (Fig. 5.10(a)) and to the $\tilde{B}$ (Fig. 5.10(b)) show a small amount of population transfer but no dissociation. The diabatic population results for the 3-state model are in agreement with the PESs, confirming our initial impression that this 3-state model cannot successfully describe the photodissociation dynamics of phenol and thus more states should be included.

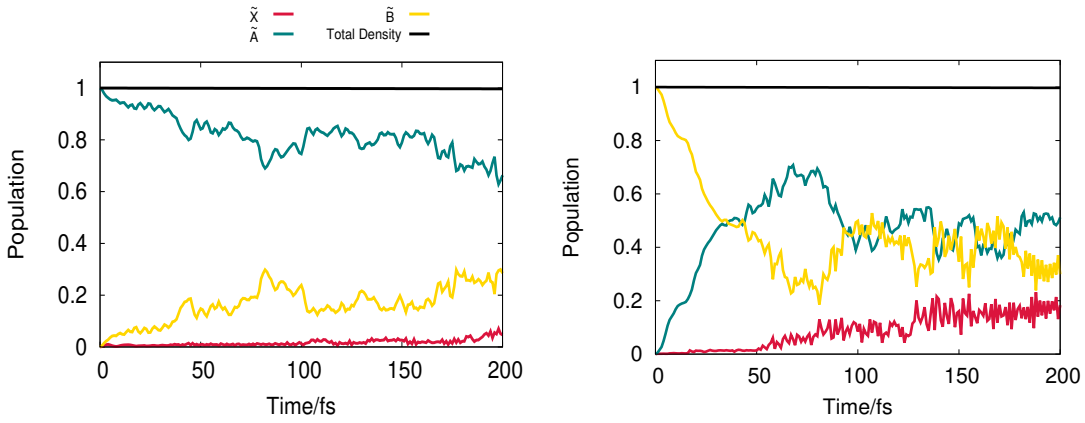

(a) $\tilde{A}$ (b) $\tilde{B}$

Fig. 5.10: Diabatic state populations from DD-vMCG simulations of phenol starting with a vertical excitation to $\tilde{A}$ and $\tilde{B}$ states for the 3-state model.

Fig. 5.11 shows that when employing a 4-state model the diabatic population dynamics are quite different from the 3-state model and that including more states

than the target ones has a significant effect on the population transfer and the percentage of dissociation as they have both considerably increased. Fig. 5.11(a) depicts the diabatic state populations for the 4-state model after excitation to the $\tilde{A}$ state. The population transfer starts immediately and mostly to the $\tilde{B}$ state and approximately 30% of the population remains in the $\tilde{A}$ state at the end of the propagation. The population transfer occurring to the rest of the states is relatively small. The population decay starts at 10 fs and is complete by around 140 fs. Moreover, for excitation to the $\tilde{B}$ state (Fig. 5.11(b)), a fast population transfer mostly to the $\tilde{A}$ state is observed, but also a small amount to the $\tilde{C}$ state. Density begins to flow into the CAPs after around 10 fs and a steady dissociation continues until the end of the propagation. For excitation to the $\tilde{C}$ state (Fig. 5.11(c)), the rate of the population transfer is considerably slower compared to the two other states. As it is also depicted, the population transfer is evenly distributed across all of the remaining states. Following the same pattern the amount of dissociation is much less compared with Figs. 5.11(a) and 5.11(b).

In the 5-state model, relaxation from the $\tilde{A}$ state (Fig. 5.12(a)) shows a similar behaviour with the 4-state model while here the presence of the $\tilde{D}$ state increases the total transfer to $\tilde{B}$ and also to $\tilde{C}$. In Fig. 5.12(b) again the principal population transfer from the $\tilde{B}$ state is occurring immediately into the $\tilde{A}$ state. After around 140 fs about 15% of the population has been transferred to the $\tilde{A}$ state, with around 10% of the population being transferred to the $\tilde{C}$ and $\tilde{D}$ states. Fig. 5.12(c) shows that after excitation to the $\tilde{C}$ state almost immediately the population is transferred mostly to the $\tilde{D}$ state while 60% of the initial population remains in the $\tilde{C}$ state when the end of the propagation is reached. A similar pattern can be noticed in Fig. 5.12(d) where a greater amount of population transfer takes place going from the $\tilde{D}$ to $\tilde{C}$ state. The decrease in total density after excitation to the $\tilde{A}$ state (Fig. 5.12(a)) and $\tilde{C}$ state (Fig. 5.12(c)) takes more time to start

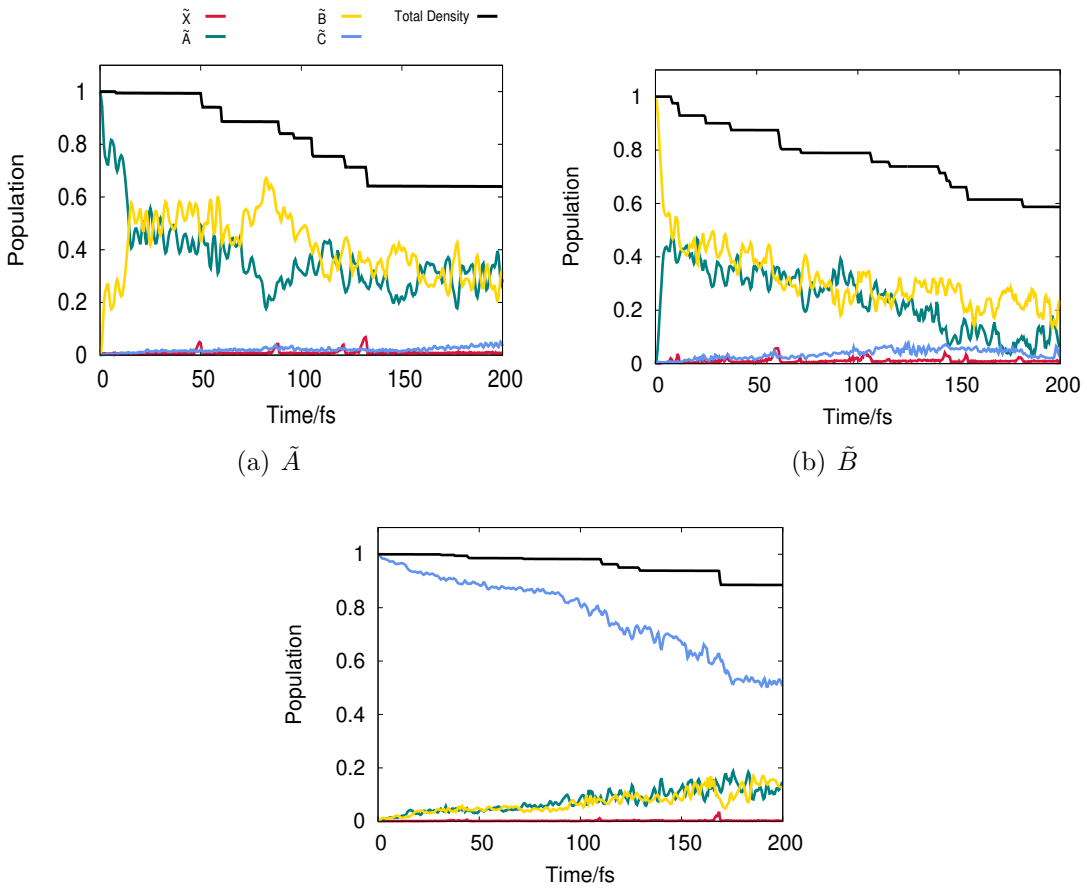

(a) $\tilde{A}$ (b) $\tilde{B}$

(c) $\tilde{C}$

Fig. 5.11: Diabatic state populations from DD-vMCG simulations of phenol starting with a vertical excitation to $\tilde{A}$, $\tilde{B}$ and $\tilde{C}$ states for the 4-state model.

compared to the other two states for which it is taking place in the first 20 fs (Figs. 5.12(b) and 5.12(d)). The amount of total dissociation is greater for excitation to the $\tilde{A}(25\%)$ and $\tilde{B}(40\%)$ states compared to excitation to the $\tilde{C}(10\%)$ and $\tilde{D}(15\%)$ states.

Moving to the 6-state model, the rate of population transfer is slower compared to the 4- and 5-state models for propagation after vertical excitation both in the $\tilde{A}$ and $\tilde{B}$ state. Apart from the slower relaxation from $\tilde{A}$ (Fig. 5.13(a)), including $\tilde{E}$ results in a significant reduction in the amount of dissociation that is now close to 10%, which is in accordance with experimental results.[162,172,173,194–196] In particular, all the figures in Fig. 5.13 follow the same trend where more time is needed for the density to begin to flow in the CAPs as we move to a higher initial

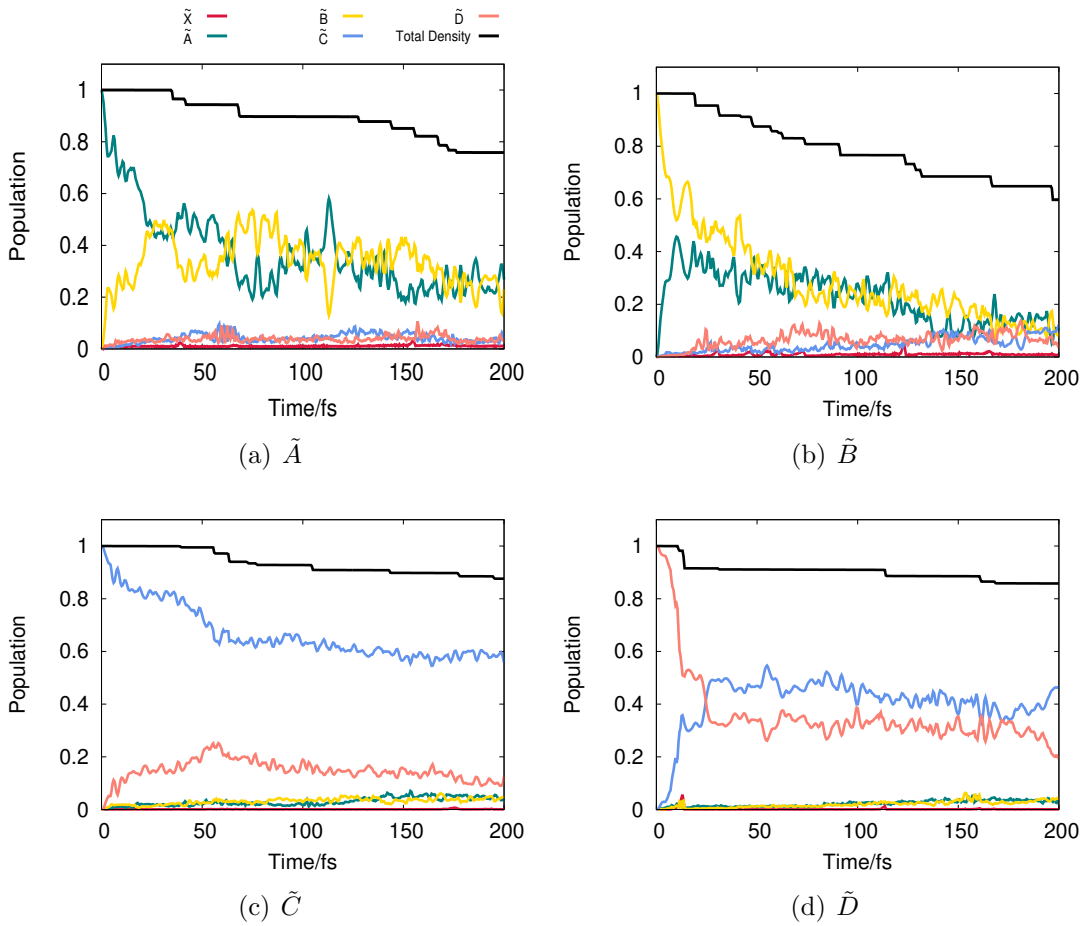

(a) $\tilde{A}$ (b) $\tilde{B}$

(c) $\tilde{C}$ (d) $\tilde{D}$

Fig. 5.12: Diabatic state populations from DD-vMCG simulations of phenol starting with a vertical excitation to $\tilde{A}$, $\tilde{B}$, $\tilde{C}$ and $\tilde{D}$ states for the 5-state model.

excitation state, notwithstanding that $\tilde{E}$ in Fig. 5.13(e) seems to slightly diverge. In Fig. 5.13(c), it appears that the population is relatively evenly distributed across all of the excited states and almost 40% of the population is still in the $\tilde{C}$ state. The strong $\tilde{D}$-$\tilde{E}$ coupling has affected the populations in both Fig. 5.13(d) and Fig. 5.13(e) where the main population transfer is occurring between these two states and is more clearly illustrated in the $\tilde{E}$ example.

The 6-state model shows that the inclusion of the $\tilde{D}$ and $\tilde{E}$ led to a better realisation of the couplings between the states and thus the population transfer and the rates of the dissociation. The 5-state model gives a poor description while the 6-state model is more like the 4-state model. The strong $\tilde{D}$-$\tilde{E}$ coupling that is seen in the 6-state model, cannot be reproduced by the 5-state and eventually

leads to a spurious $\tilde{C}$-$\tilde{D}$ coupling. This poor description of the couplings also caused the incorrect CoIs at the PESs as depicted at Figs. 5.7(c) and 5.7(d). The above results showed the importance of conducting further analysis besides the PESs in order to understand the complex dissociative behaviour of phenol.

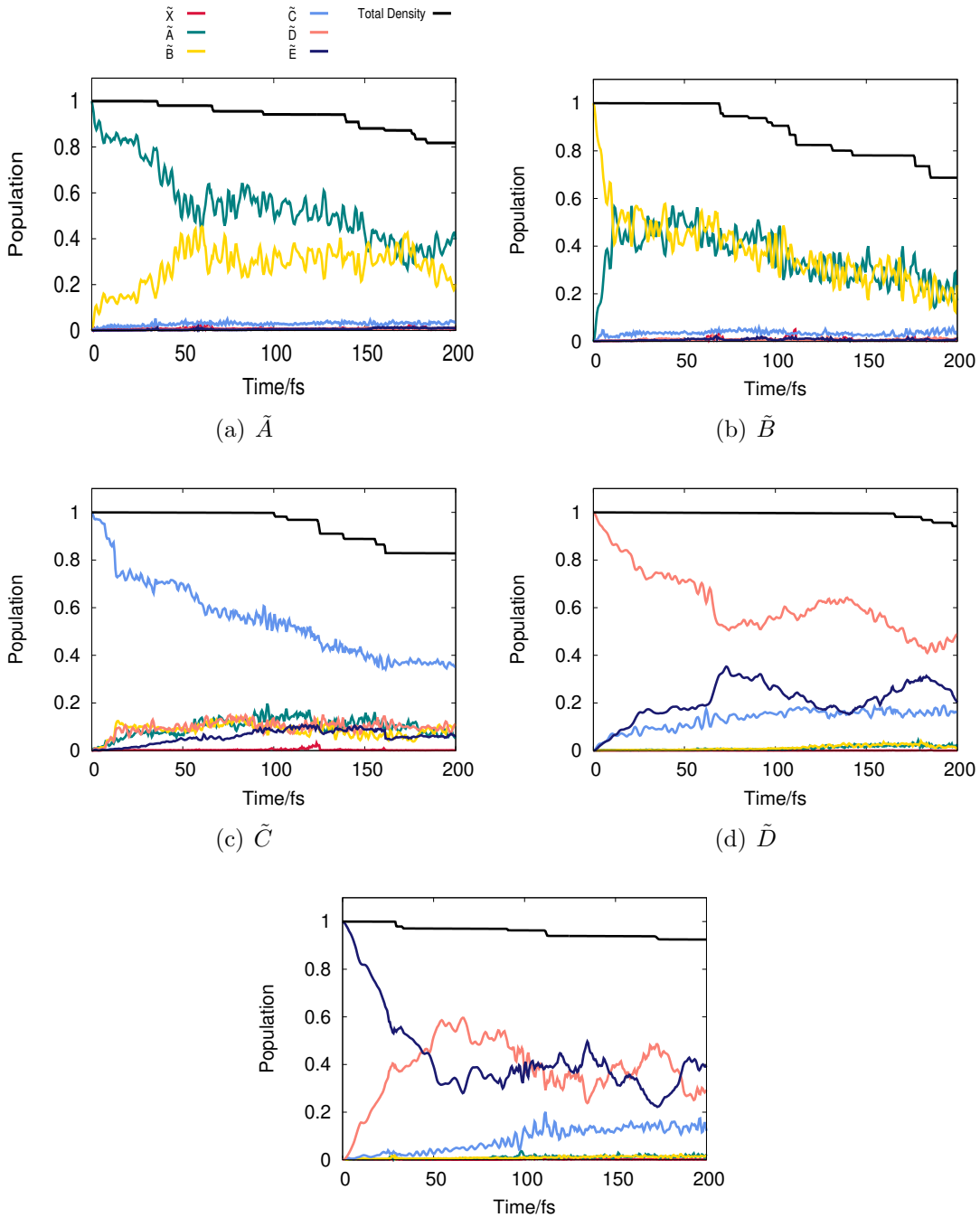

(a) $\tilde{A}$ (b) $\tilde{B}$

(c) $\tilde{C}$ (d) $\tilde{D}$

(e) $\tilde{E}$

Fig. 5.13: Diabatic state populations from DD-vMCG simulations of phenol starting with a vertical excitation to $\tilde{A}$, $\tilde{B}$, $\tilde{C}$, $\tilde{D}$ and $\tilde{E}$ states for the 6-state model.

5.6.3 Flux Analysis

A computational analysis of the PESs together with the state populations gives a very good description of the dissociative behaviour of the different states, the connection between these states and more importantly the significance of including more states for the description of the dynamics for phenol. Moreover, it is important to unravel the probability of the different decay pathways in order to understand the dynamic mechanisms of the photodissociation of phenol. To this end, the integral of the flux into each dissociation channel was analysed. It is obtained using Eq. 5.25 by integrating the expectation value of the CAP using the density projected onto each state to give the probability of decay via that channel as a function of time. It is important to note that considering the outcomes of Fig. 5.10 - Fig. 5.13 only the integrated flux for the 4- and 6-state models was plotted for the $\tilde{X}$, $\tilde{A}$ and $\tilde{B}$ states as flux was very close to zero for the rest of the states.

Fig. 5.14 shows that the flux across dissociation channels ($\tilde{X}$ and $\tilde{B}$) increases significantly for both the 4- and 6-state models and the dissociation occurs after 50 fs. After excitation to $\tilde{A}$ for the 4-state model, Fig. 5.14(a), a first significant rise on the $\tilde{B}$ state is taking place around 100 fs and then the majority of the flux is going into the $\tilde{X}$ state at around 125 fs. For the 6-state model (Fig. 5.14(c)), the flux follows the same pattern while the flux distribution into $\tilde{B}$ is about double the one to $\tilde{X}$, and also the proportion of the flux going into the $\tilde{A}$ state is increased.

In the case of excitation to $\tilde{B}$, in both Figs. 5.14(b) and 5.14(d) the flux distribution into the three target states follows a very similar pattern. The amount of flux in both $\tilde{X}$ and $\tilde{B}$ gradually increases with an analogous rate, while in the case of the 6-state model the amount of flux into $\tilde{B}$ after 175 fs is greater compared to the one into $\tilde{X}$. It can be noted that after excitation to the $\tilde{B}$ state for the 4-state model, there is more energy and thus more dissociation in the $\tilde{A}$ state is possible. Fig. 5.14(b) shows that the percentage of the total flux going out of $\tilde{A}$

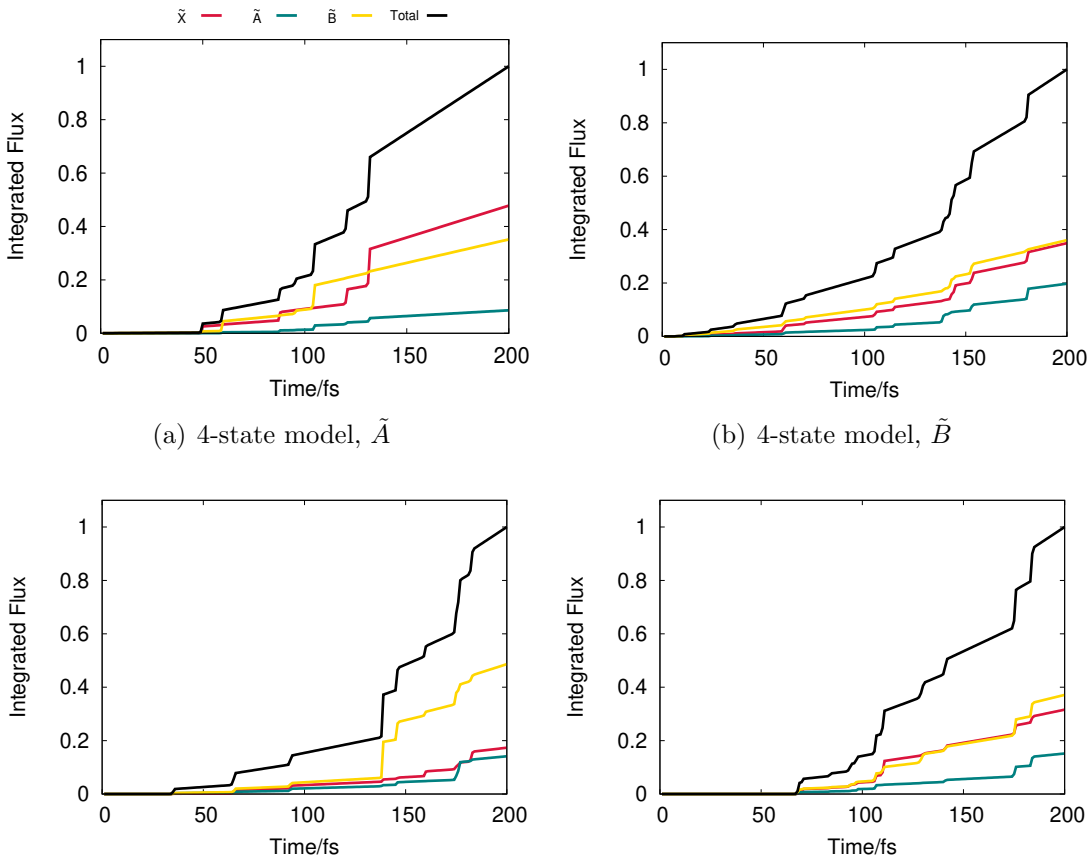

(a) 4-state model, $\tilde{A}$

(b) 4-state model, $\tilde{B}$

(c) 6-state model, $\tilde{A}$

(d) 6-state model, $\tilde{B}$

Fig. 5.14: Normalised integrated flux as a function of time from DD-vMCG simulations of phenol starting with a vertical excitation to $\tilde{A}$ and $\tilde{B}$ states for the 4- and 6-state models.

has been doubled compared to Fig. 5.14(a). In the case of the 6-state model the in which state the excitation is conducted does not seem to affect the results since the percentage of the total flux going out of $\tilde{A}$ stays almost constant.

As literature shows the dissociation mechanism of phenol is a controversial subject. In some research studies it is indicated that an ultrafast internal conversion from the bright $^1\pi\pi^*$ state to the dark $^1\pi\sigma^*$ state through their CoI seam, leading to the formation of the phenoxyl radical after hydrogen dissociation is the main dissociation mechanism.[173,192] In this study, as all the above outcomes suggest, the timescales are probably too short for the O-H dissociation through hydrogen tunnelling as in all cases the lower $\tilde{X}$-$\tilde{B}$ channel is more favorable. Thus, the conical intersection between the $^1\pi\sigma^*$ and the $\tilde{X}$ state which provides an alter-

native pathway of rapid relaxation to the electronic ground state is suggested to be the primarily dissociation pathway. This outcome is strongly supported by experimental studies.[159,160]

5.7 Discussion

In this Chapter, the improved algorithm for DD-vMCG[197] has made possible the successful study of the full dimensional photo-dissociation dynamics of phenol. Thus the goal was twofold, firstly to unravel the complicated full dimensional dissociation dynamics of phenol and especially the decay pathways and further to test the efficiency and accuracy of the new DD-vMCG algorithm in a more complex chemical system such as phenol. Initially the development of the existing code by creating a new interface so that Quantics can call any available external program to compute the energies, gradients and Hessians of a given molecular system and then store all the data in the quantum chemistry database was presented. An electronic structure analysis was then conducted at a CASSCF/6-311+G** level of theory with an active space of 10 electrons in 10 orbitals. All electronic structure calculations were done with the OpenMolcas program. The DD-vMCG protocol was then established, including the number of states, GWPs and the total propagation time along with the strategy followed to converge the database. Finally, the theory around using a CAP to calculate the dissociation flux was presented.

The results of DD-vMCG calculations were analysed by plotting the PESs, the diabatic state populations and the integrated flux. The potential energy surfaces were firstly presented for the 3-, 4-, 5- and 6-state models. The 4-state and 6-state models where the ones with the smoothest PESs and well defined conical intersections between the ground state and the first three excited states. At the same time, the 5-state model could not successfully describe the dynamics of phenol as not including $\tilde{E}$, which is strongly coupled with the $\tilde{D}$ state, lead to meaningless conical

intersections and fluctuations in the PESs. Finally, the 3-state model was quite computationally hard to run direct dynamics calculations and also to converge even compared to the 6-state model which obviously is a harder computational problem. This theoretical study by including for the first time five excited states showed the importance of designing models with more states than the target ones in order to have a better description for the molecule under investigation. It has been shown that for phenol the 3-state model has to be completely abandoned and even the 4-state model that clearly offers a significantly better description of the dynamics is still not enough to match the experimental findings. This outcome is especially important for the dynamics of molecules which are strongly affected by conical intersections.

A direct dynamics comparison analysis was also presented by employing the 3-state model with OpenMolcas and the PES_{XZYT} model and also the 4-state model with OpenMolcas and the PES_{ZY} model for phenol. The comparison results not only suggested that DD-vMCG with OpenMolcas can reproduce the PESs obtained analytically in the aforementioned studies but also to generate smoother surfaces with better defined states and conical intersections between them. Additionally, the advantage of using DD-vMCG over analytically calculated PESs to study the molecular dynamics of a compound has been proved relying on the less computational effort, the higher accuracy and the significant flexibility.

Additionally, a comparison of the vertical excitation energies obtained in this study for different state-averaging with those in prior experimental and theoretical studies showed that the calculated energies are in agreement with the theoretical results and a quite good match with the experimental values and the 6-state model yields the closest values to the experimental data available.

The state population analysis showed that both the 4-state and the 6-state model can accurately describe the state population transfer. However, the 6-state

model after excitation to the $\tilde{A}$ state best describes the population transfer and distribution between the states which matches experimental findings. Here, the reason behind the poor description of the PESs when the 5-state model is employed becomes more clear. The strong $\tilde{D}$-$\tilde{E}$ coupling that is seen in the 6-state model, but cannot be reproduced, is leading to a spurious $\tilde{C}$-$\tilde{D}$ coupling. The populations for the 3-state model showed a small amount of population transfer but no dissociation regardless of the initial excitation state which again confirms the idea that more states should be included for the description of phenol. Important conclusions regarding the decay mechanism have also been presented by computing the flux distribution into the different states. It is clear that the dissociation pathway provided by the conical intersection between the $1^1\pi\sigma^*$ and the $^1\pi\pi$ state is more favourable during the phenol dynamics by offering a rapid relaxation to the ground state.

Beyond the successful description of the photodissociation of phenol, this study illustrates the possibilities of the DD-vMCG method as it is capable of capturing the complete quantum picture of the coupled nuclear and electronic motions after photo-excitation into multiple states for a molecule like phenol with 33 vibrational modes. A natural extension of this work will be to perform quantum dynamics simulations with DD-vMCG to the phenoxyl radical in order to further unravel the photodissociation dynamics of phenol.

Chapter 6

Direct Dynamics using Gaussian Process Regression

6.1 Introduction

After dealing with the main bottleneck besides quantum chemistry calculations that DD-vMCG was encountering, namely the time needed to reread, sort and analyse the database as presented in Chapter 4, it is appropriate to check for other possible sources of errors and time time consuming tasks. As discussed in Chapter 3, solving the time-dependent Schrödinger equation for DD-vMCG by employing a linear combination of Gaussian wavepackets (GWPs), a computationally expensive evaluation of integrals is needed to compute the potential energy surfaces of the target molecule. The computational tractability of direct dynamics led to a standard approach which was a Taylor expansion to the second order.[18,112,117,121] The aforementioned expansion of the PES is known as local harmonic approximation (LHA). The fact that the potential energy matrix elements are expanded to the second order limits the range over which the interpolation may be considered as accurate enough for quantum chemistry simulations. Additionally, it is computationally very expensive to calculate the electronic gradients and Hessians at the centre of each Gaussian wavepacket at every time-step of the propagation.

A successful solution to various problems in Quantum Chemistry (QC) has been found by employing machine learning ML algorithms. As depicted in Fig.

6.1, machine learning can be used as a powerful prediction tool, subject to certain conditions, such as good machine learning algorithms and training data. The advantages of machine learning techniques in quantum chemistry rely on the speed which is comparable to molecular mechanics and on the accuracy when predicting the required property. Thus, having a tool that offers significantly quicker and more accurate performance than traditional quantum chemistry methods is a great advantage and can be very beneficial both in improving existing and developing new methods and also in unraveling the behaviour of different molecular systems.

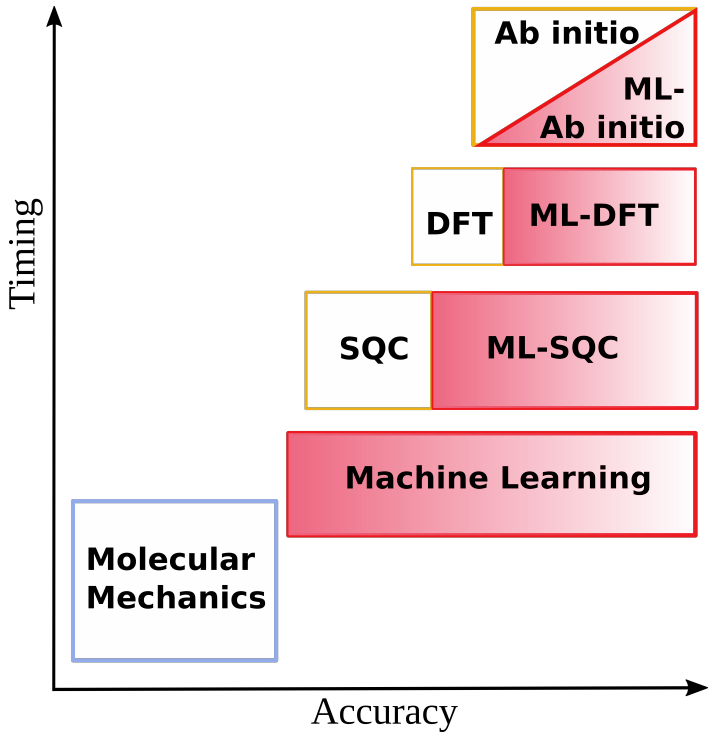

Fig. 6.1: Schematic representation of accuracy of different quantum chemistry methods and machine learning approximations as a function of timing (computational cost). SQC denotes the semiempirical quantum chemistry methods. Adapted with permission from ref. 198.

In this chapter, a different approach for approximating the potential energy surface matrix elements relying on PES interpolation employing machine learning is described and compared to LHA. More specifically, a nonparametric, Bayesian approach to regression that has received considerable attention in the area of machine learning is employed which is known as Gaussian process regression (GPR).[199] In

this machine learning method, in each time-step, solely single-point evaluations of the potential energy surfaces at a finite number of configurations are required. Thus, there is no need for performing expensive evaluations of gradients and Hessians. Benchmark calculations have been performed on the ozone molecule employing both DD-vMCG and DD-vMCG using Gaussian-approximation potentials, called GAP-vMCG,[200] to directly compare these two methods. The advantages of GPR over LHA are examined and discussed in detail along with a future work section where the possibility for further developments of GAP-vMCG are highlighted.

6.2 Local Harmonic Approximation

In this section, the second order Taylor expansion is described in more detail, which together with the Shepard interpolation[201] constitutes the foundation of the local harmonic approximation as used in DD-vMCG. The Shepard interpolation scheme employed by direct dynamics and its theory have been extensively discussed in section 4.2.

For an f-dimensional system, the GWPs in Heller form have the following form

$$g_i(\mathbf{q},t) = \prod_{k=1}^{f} \left(\frac{2a_i^k}{\pi}\right)^{1/4} e^{-a_i^k(\hat{q}^k - q_i^k(t))^2 + ip_i^k(t)(\hat{q}^k - q_i^k(t))} \tag{6.1}$$

where the parameters of the GWPs for each DOF are q which denotes the position and thus $\hat{q}$ is the position operator, p the momentum and α the width parameter. As mentioned before, in DD-vMCG the width parameters are fixed since "frozen" GWPs are employed. Hence, the potential energy matrix elements for the $g_i(\mathbf{q},t)$ and $g_j(\mathbf{q},t)$ basis functions can be written as

$$V_{ij} = \int d\mathbf{q}\; g_i^*(\mathbf{q},t)\widehat{V} g_j(\mathbf{q},t) \tag{6.2}$$

Integration is over all the space dimensions (f) of the target molecule. However, it is generally impossible to exactly evaluate this integral unless a simple analytical

form of the PES is available. This applies to on-the-fly methods such as DD-vMCG where the evolution of the time dependent Schrödinger equation is linked to the PES evaluation by employing *ab initio* electronic structure calculations. In these cases where the analytical PES is not available, the most widely used approach for the calculation of PES matrix elements, V_{ij}, is to employ a Taylor expansion. Usually, this expansion is taken around either the position of the GWP calculated from the product of the two separate GWPs or the position $\mathbf{q}$ of one of the GWPs. For DD-vMCG, the second-order Taylor expansion requires the evaluation of energies, gradients and Hessians.

One of the most prominent and broadly used properties of Gaussian basis functions is that the product of two of them is again a Gaussian function. Thus, in the GWPs case, applying Eq. 6.1, the product of two GWPs where the one is defined as the complex conjugate can be written as

$$g_i^*(\mathbf{q})g_j(\mathbf{q}) = \prod_{k=1}^{f}\left(\frac{4a_i^k a_j^k}{\pi^2}\right)^{1/4} e^{-a_i^k+a_j^k(\hat{q}^k-\bar{q}^k)^2+i(p_i^k-p_j^k)\hat{q}^k+ip_i^kq_i^k-ip_j^kq_j^k-a_i^k(q_i^k)^2-a_j^k(q_j^k)^2} \tag{6.3}$$

which is a complex Gaussian function centred at

$$\bar{q}^k = \frac{a_i^k q_i^k + a_j^k q_j^k}{a_i^k + a_j^k} \tag{6.4}$$

For frozen GWPs with equal widths,[202] the mean value of the two constituent GWPs coordinates is equal to the product centre $\bar{q}^k$.

Since the Gaussian wavepacket products in Eq. 6.2 are localised around $\bar{q} = (\bar{q}^1, \bar{q}^2, ..., \bar{q}^f)$, major progress can be achieved in evaluating PES matrix elements employing a Taylor expansion around $\bar{q}$

$$V(\mathbf{q}) \simeq V(\bar{\mathbf{q}}) + \sum_{k=1}^{f}(\hat{q}^k - \bar{q}^k)\frac{\partial V}{\partial q^k} + \frac{1}{2}\sum_{k,\mu=1}^{f}(\hat{q}^k - \bar{q}^k)\frac{\partial^2 V}{\partial q^k \partial q^\mu}(\hat{q}^\mu - \bar{q}^\mu) \tag{6.5}$$

where the gradients and the Hessians are computed at $\bar{q}$. By substituting Eq. 6.5

into Eq. 6.2, the PES takes the following form

$$V_{ij} = \left\langle g_i \left| \widehat{V} \right| g_j \right\rangle \simeq V(\bar{\mathbf{q}}) S_{ij} + \sum_{k=1}^{f} (\left\langle q^k \right\rangle_{ij} - \bar{q}^k S_{ij}) \frac{\partial V}{\partial q^k} + \frac{1}{2} \sum_{k,\mu=1}^{f} \left[\left\langle q^k q^\mu \right\rangle_{ij} - \bar{q}^k \left\langle q^\mu \right\rangle_{ij} - \bar{q}^\mu \left\langle q^k \right\rangle_{ij} + \bar{q}^k \bar{q}^\mu S_{ij} \right] \frac{\partial^2 V}{\partial q^k \partial q^\mu} \tag{6.6}$$

where

$$\left\langle q^k \right\rangle_{ij} = \left\langle g_i \left| \widehat{q}^k \right| g_j \right\rangle \tag{6.7}$$

and

$$\left\langle q^k q^\mu \right\rangle_{ij} = \left\langle g_i \left| \widehat{q}^k \widehat{q}^\mu \right| g_j \right\rangle \tag{6.8}$$

Alternatively to the aforementioned mid-point Taylor expansion method, a Taylor expansion around one of the GWP basis functions can be considered which is the approach employed by DD-vMCG. Moving the centre of the Taylor expansion to $q_i(t)$, and once again truncating up to the second-order results in three additional potential energy surface approximation methods, Gaussian-based Taylor expansion to the zeroth order

$$V_{ij} \simeq V(\mathbf{q_i}) S_{ij} \tag{6.9}$$

where S_{ij} is the overlap matrix

$$S_{ij} = \langle g_i | g_j \rangle \tag{6.10}$$

Gaussian-based Taylor expansion to the first order

$$V_{ij} \simeq V(\mathbf{q}_i) S_{ij} + \sum_{k=1}^{f} (\left\langle q^k \right\rangle_{ij} - q_i^k S_{ij}) \frac{\partial V}{\partial q_i^k} \tag{6.11}$$

Gaussian-based Taylor expansion to the second order

$$V_{ij} \simeq V(\mathbf{q}_i) S_{ij} + \sum_{k=1}^{f} (\left\langle q^k \right\rangle_{ij} - q_i^k S_{ij}) \frac{\partial V}{\partial q_i^k} + \frac{1}{2} \sum_{k,\mu=1}^{f} \left[\left\langle q^k q^\mu \right\rangle_{ij} - \bar{q}^k \left\langle q^\mu \right\rangle_{ij} - q_i^\mu \left\langle q^k \right\rangle_{ij} + q_i^k \bar{q}^\mu S_{ij} \right] \frac{\partial^2 V}{\partial q_i^k \partial q_i^\mu} \tag{6.12}$$

The zero-order approximation is known as the saddle-point approximation and it is employed in AIMS. If the second-order Taylor expansion is used like in vMCG, then the energy, gradients and Hessian matrix have to be computed at each point. The second-order approximation requires n evaluations of the potential for n GWPs rather than n(n+1)/2 that the midpoint approach needs. Also, it is essential for the "CX" formalism which enables the division of the equations of motion into "classical" and "non-classical" parts.

Although this is a very beneficial approach that takes advantage of the locality of GWPs, it faces some bottlenecks. For instance, the computational effort needed for the calculation of the Hessians using *ab initio* methods is quite demanding. As previously discussed in 3.3.3, in direct dynamics a Hessian update approach is applied which has the risk of introducing more inaccuracies and cost in our calculations. However, the main disadvantage of employing LHA is that vMCG does not converge on the exact result.

6.3 Gaussian Process Regression

6.3.1 Introduction

The use of machine learning techniques to fit molecular potential energy surfaces has been steadily gaining interest; such a technique is Gaussian process regression[199,203–206] which is sufficiently simple and robust to be a viable alternative to artificial neural networks[207] (ANNs) for solving general problems. Applications of GPR on small molecular systems have demonstrated that high quality PESs can be achieved with a remarkably small number of data points and that this number scales almost linearly with the size of the system.[208–211] It remains to be seen if larger and more complex systems still show this scaling. Also, strategies for training points selection still need to be optimised.

Gaussian process regression is a machine learning technique which is based on

statistical learning theory and Bayesian theory. It is highly adaptable and can be easily generalised to solve complicated regression and classification problems, such as high dimensions, small samples, and non-linearity problems.[207] Successful applications of GPR are varied and include dynamic system model identification,[212] time series prediction analysis,[213] system control[214] and quantum chemistry.[215] There are however some drawbacks to GPR such as the limitation of the Gaussian noise distribution hypothesis and the need to use all the available data in order to perform the required prediction. Additionally, the performance of GPR is heavily dependent on how the hyperparameters are selected. The number of GPR learning iterations is reduced and the accuracy of the fitting and the ability of the model to be general are enhanced if suitable hyperparameter values are selected. Therefore, a crucial topic in machine learning is hyperparameter optimization.[216,217]

Koch and Zhang[218] were the first to report the use of machine learned potentials for on-the-fly GWP-based molecular dynamics simulations; they obtained analytic potential energy matrix elements by employing multiplicative ANN to fit potential energy surfaces on-the-fly with good performance and accuracy. In a later study, the Gaussian approximation potential (GAP)[200] method was applied to direct dynamics with classically propagated GWPs. The authors reported potential energy matrix elements with higher accuracy when compared with LHA and based on these findings proposed that GPR should replace LHA in direct quantum dynamics. Hyperparameters for GPR were not optimised in this work, making its predictions analogous to kernel ridge regression (KRR).[219] Subsequently, the same GPR technique was successfully employed with the MCTDH method by Richings and Habershon,[220,221] establishing this approach as a direct dynamics MCTDH without the need for a global PES to be pre-fitted. Moreover, GAP-vMCG was firstly introduced by Polyak et al.[222] but was limited to ground state calculations. In ref. 223, the case of the proton transfer isomerisation of salicylaldimine was

studied and it was proved that multi-dimensional direct quantum dynamics is possible with this method.

6.3.2 The General Algorithm

Gaussian process (GP) which is also termed as normal stochastic process, is a probabilistic kernel machine that is based on the statistical learning theory and the Bayesian theory.[199] In terms of function space, GP corresponds to any set of finite random variables with a joint Gaussian distribution, such as $Q = [\mathbf{q}_1, \mathbf{q}_2, \cdots, \mathbf{q}_n]^T$, whose properties are defined through the mean function $\mu(\mathbf{q})$ and covariance function $a(\mathbf{q}, \mathbf{q}')$. GP is thus defined as follows

$$f(\mathbf{q}) \sim GP(\mu(\mathbf{q}), a(\mathbf{q}, \mathbf{q}')) \tag{6.13}$$

where $\mathbf{q}, \mathbf{q}' \in \mathbb{R}^d$ refer to two stochastic variables. Normally, the mean value of sample data is originally set to zero. The standard linear regression model with Gaussian white noise is then given by

$$\mathbf{y} = f(\mathbf{q}) + \boldsymbol{\varepsilon}\ , \quad f(\mathbf{q}) = \mathbf{q}^T \cdot \mathbf{w} \tag{6.14}$$

where, $\mathbf{q}$ refers to an input vector, $\mathbf{y}$ is the noisy output vector such as the observed value, $f(\mathbf{q})$ is the value of the objective function, $\mathbf{w}$ is the weight vector and $\boldsymbol{\varepsilon}$ is the noise which obeys a Gaussian distribution.The normal distribution is often referred to as $N(\mu, \sigma^2)$. Thus when a random variable X is normally distributed with mean μ and standard deviation σ, it can be expressed as $X \sim N(\mu, \sigma^2)$.

$$\mathbf{w} \sim N\left(\mathbf{0}, \sum\nolimits_P\right) \ (\Sigma_p \text{ is covariance}) \tag{6.15}$$

$$\boldsymbol{\varepsilon} \sim \mathrm{N}(\mathbf{0}, \boldsymbol{\sigma}_n^2) \ (\boldsymbol{\sigma}_n^2 \text{ is variance}) \tag{6.16}$$

The prior distribution of the observed values $\mathbf{y}$ can then be written as

$$\mathbf{y} \sim \mathrm{N}(\mathbf{0}, \mathbf{A}(Q, Q) + \boldsymbol{\sigma}_n^2 \mathbf{I}_n) \tag{6.17}$$

Joint distributions of the observed value $\mathbf{y}$ and the predicted value f^* are written as

$$\begin{bmatrix} \mathbf{y} \\ f^* \end{bmatrix} \sim N\left(0\,, \begin{bmatrix} \mathbf{A}(Q,Q) + \boldsymbol{\sigma}_n^2 \mathbf{I}_n & \mathbf{A}(Q,q^*) \\ \mathbf{A}(q^*,Q) & a(q^*,q^*) \end{bmatrix}\right) \tag{6.18}$$

where $\mathbf{A}(Q,Q) = \mathbf{A}_n = (a_{ij})$ is the $n \times n$ symmetric positive definite covariance matrix, $\mathbf{I}_n$ denotes the n dimensional identity matrix, $\mathbf{A}(Q,q^*)$ the $n \times 1$ order covariance matrix of the new input test points q^* and all input points set Q, $\mathbf{A}(Q,q^*) = \mathbf{A}(q^*,Q)^T$, and $a(q^*,q^*)$ is the covariance matrix of the test point q^*.

The posterior distribution of the predicted value f^* is thus obtained through regression as per Eqs. 6.19-6.21

$$f^*|Q,\mathbf{y},q^* \sim \mathrm{N}(\bar{f}^*, cov(f^*)) \tag{6.19}$$

where $\bar{f}^*$ is the mean value and $cov(f^*)$ the variance of the predicted value f^* determined as

$$\bar{f}^* = \boldsymbol{A}(q^*,Q)[\boldsymbol{A}(Q,Q) + \boldsymbol{\sigma}_n^2 \mathbf{I}_n]^{-1}\mathbf{y} \tag{6.20}$$

$$\begin{aligned} cov(f^*) =& a(q^*,q^*) - \boldsymbol{A}(q^*,Q)[\boldsymbol{A}(Q,Q) \\ &+ \boldsymbol{\sigma}_n^2 \mathbf{I}_n]^{-1}\boldsymbol{A}(Q,q^*) \end{aligned} \tag{6.21}$$

The covariance function, also known as kernel function, has various differential forms in GPR. One such form is, the heterogeneous square exponential kernel function

$$a(\mathbf{q},\mathbf{q}') = \theta \exp(-\gamma \left\|\mathbf{q}-\mathbf{q}'\right\|^2) \tag{6.22}$$

where θ and γ are the parameters of the kernel function.

Due to the introduction of noise, the variance function in GPR contains additional parameters called hyperparameters. Hyperparameters in Gaussian process regression contain the following

i. The first hyperparameter is the variance $\boldsymbol{\sigma}_n^2$ of noise $\boldsymbol{\varepsilon}$ (Eq. 6.16) and includes two hyperparameters (u, v).

ii. The second hyperparameter refers to the covariance $\sum_P$ of weight vector $\mathbf{w}$ (Eq. 6.15). Particularly, $\sum_P$ includes two hyperparameters (α, β).

iii. The third hyperparameter refers to the θ and γ parameters included in the kernel function a (Eq. 6.22).

As mentioned in section 6.3.1, using optimum hyperparameters in GPR is conducive to fitting accuracy and generalization ability.[216,217,224–227]

6.3.3 Calculation of Potential Energy Surface Matrix Elements

Employing Gaussian process regression,[200] the interpolated potential energy surface can be written as a linear combination of Gaussian terms,

$$V(\mathbf{q}) \simeq \sum_{k=1}^{M} w_k e^{-\gamma|\mathbf{q}-\mathbf{q}_k|^2} \tag{6.23}$$

where M is the number of reference configurations, where the value of PES is assumed to be calculated, and γ determines the length-scale of the Gaussian functions. The exponential term is the kernel function. Considering M values of the potential energy surface, to determine the values of M unknown weights (w_k) in the interpolated potential energy surface, M equations have to be solved simultaneously

$$\mathbf{A}\mathbf{w} = \mathbf{b} \tag{6.24}$$

where $\mathbf{A}$ denotes an $M \times M$ covariance matrix with the following elements

$$A_{ij} = e^{-\gamma|\mathbf{q}-\mathbf{q}_k|^2} + \sigma^2\delta_{ij} \tag{6.25}$$

and $\mathbf{b}$ denotes the vector of known potential energy surface values at the reference configurations

$$b_i = V(\mathbf{q}_i) \tag{6.26}$$

The hyperparameters σ and γ are considered in this work as simple variables which have fixed values during direct dynamics calculations. A better approach would be to minimise the prediction error in order to optimise them.

Applying GPR in direct dynamics, it is assumed that the GWP basis set employed is time-dependent and that at each time-step the value of the PES is calculated at the $\mathbf{q}_i(t)$ positions of the GWP centres. The data generated will work as M reference points from which the GPR interpolation surface will be constructed. In Quantics the energy is calculated at the centre of the GWP if the variance is large enough (only when using random sampling) and then at a range of points around the centre of each GWP (done when using both random or Sobol sequence sampling), again if the variance at each point is large enough.

After the weights have been evaluated (Eq. 6.24), the potential energy matrix elements are then determined employing the GPR surface

$$\begin{aligned} V_{ij} &= \int d\mathbf{q}\; g_i^*(\mathbf{q},t)\widehat{V}g_j(\mathbf{q},t) = \sum_{k=1}^{M} w_i \int d\mathbf{q}\; g_i^*(\mathbf{q},t)e^{-\gamma|\mathbf{q}-\mathbf{q}_k|^2}g_j(\mathbf{q},t) \\ &= \sum_{k=1}^{M} w_i \prod_{\kappa=1}^{f} \int dq^k (g_i^k(q^k,t))^* e^{-\gamma(q-q_k)^2}(g_j^k(q^k,t)) = \sum_{k=1}^{M} w_i \prod_{\kappa=1}^{f} I_\kappa^k \end{aligned} \tag{6.27}$$

The Gaussian terms of Eq. 6.23 and the GWPs conveniently are both a simple product of one-dimensional terms, i.e. one for each of the f DOF. For a reference point κ and DOF k, the one-dimensional Gaussian integral I can be evaluated analytically

$$I_\kappa^k = N\left(\frac{\pi}{a}\right)^{1/2} e^{\frac{(b+ic)^2}{4a}+(d+ie)} \tag{6.28}$$

the coefficients can be further expanded as follows

$$\begin{aligned} a =& a_i^k + a_j^k + \gamma \\ b =& 2a_i^k q_i^k + 2a_j^k q_j^k + 2\gamma q_\kappa^k \\ c =& p_j^k - p_i^k \\ d =& - a_i^k (q_i^k)^2 - a_j^k (q_j^k)^2 - \gamma (q_\kappa^k)^2 \\ e =& p_i^k q_i^k - p_j^k q_j^k \\ N =& \left(\frac{2a_i^k}{\pi}\right)^{1/4} \left(\frac{2a_j^k}{\pi}\right)^{1/4} \end{aligned} \tag{6.29}$$

In general, after determining the GPR weights, the entire potential energy matrix is analytically evaluated by employing the GPR approximation of Eq. 6.23. This is just a simple sum-of-product terms evaluation. GAP-vMCG employs potential energy surface evaluations at the position of the GWP centre at each time-step, builds the GPR weights and Eqs. 6.23, 6.27 and 6.28 are then employed in order to determine the full potential energy matrix. Nevertheless, this is one of the simplest ways that GPR can be implemented for quantum dynamics simulations and further possible improvements will be discussed and suggested as future work.

Moreover, the kernel employed in GPR can be expanded as a sum of lower dimensional Gaussian functions which is known as additive kernel and can be expressed as

$$a^{ADD}(\mathbf{q}, \mathbf{q}^n) = \sum_{k=1}^{f} a(q_k, q_k^n) + \sum_{k,l}^{f} a(q_k, q_k^n) a(q_l, q_l^n) + \cdots + a(\mathbf{q}, \mathbf{q}^n) \tag{6.30}$$

where a is a one-dimensional kernel function (Eq. 6.22). This is a successful approach when fitting multi-dimensional PESs. The advantage of this approximation is that each Gaussian function used in the expansion now depends on only a subset of the energy points in the database which work as the input variables.

Finally, it is worth comparing GPR with the second-order Taylor expansion and more specifically LHA as a tool to determine the potentials. The main difference

is the calculation of the gradients and Hessian matrix needed in LHA while GPR only needs the potential energy values. Additionally, apart from assuming that PES smoothly varies along the chosen coordinates, no presuppositions about the local shape of the PES are made in GPR. To sum up, GPR has a lot of advantages with respect to machine learned PESs suitable for molecular dynamics simulations. A simple question to be answered is how much better it performs relating to the accuracy and the efficiency in comparison with LHA. An attempt to address this question is made in the next section of this chapter.

6.4 Results

6.4.1 Computational Details

All the nuclear dynamics calculations were performed using the DD-vMCG implementation in the QUANTICS package.[21] To investigate the ozone molecule, direct dynamics were performed on the ground and first two excited electronic states of this molecule including all degrees of freedom as mass-frequency scaled normal modes. The electronic structure calculations were carried out employing MOLPRO 2015.1[141] at the SA-CASSCF(12,9)/6-31++G* level of theory. The initial wavepacket was a Gaussian function of width $1/\sqrt{2}$ along all normal coordinates. The GWPs were initially distributed in momentum space which is the default is vMCG. An initial calculation was conducted with a vertical excitation to the first excited state using 20 Gaussian basis functions, with a propagation time of 100 fs with data output every 0.1 fs.

Initially, a DD-vMCG run was conducted with an empty database and then multiple propagations were performed until no new points were added to the database, with the database from the previous step employed each time. Afterwards, this final database was employed by both DD-vMCG and GAP-vMCG to read all required information in order to fit the PESs. In the case of GAP-vMCG

only energies were taken from the database, while in DD-vMCG the gradients and the Hessian matrix were also used. The various common parameters used in these propagations along with the level of theory have been kept constant, thus sensible conclusions from these comparisons can be drawn.

It is worth noting that similarly with the approach followed in Chapter 4 where benchmark calculations on butatriene were conducted, here the same test molecule was initially employed to validate the accuracy and efficiency of GAP-vMCG. Since a detailed analysis for butatriene was already presented in Chapter 4, it was decided to include only the analysis of the ozone molecule in this chapter.

6.4.2 Ozone

The ozone molecule, O_3, has been proved to be vital in the life process of the upper atmosphere. Additionally, it has a wide range of applications in different scientific areas such as physics, environmental studies, synthetic biology and chemistry.[228–230] Thus, different chemical and physical properties of the ozone molecule have been examined in great detail. In this work, ozone has been used as a test molecule for benchmark calculations in order to unravel the differences and similarities in efficiency and accuracy of DD-vMCG and GAP-vMCG, and to further obtain useful conclusions from the comparison of LHA with GPR potentials.

The equilibrium structure of ozone, shown in Fig. 6.2, belongs to the C_{2v} point group. Experimental and computational studies have mostly been focused on the higher energetic triplet spin states.[231–234] Three low lying triplet states exist, $^3B_2$, $^3A_2$, and $^3B_1$, which were firstly confirmed,[235] when an absorption spectrum experiment in the 10,000-22,000 cm^{-1} band was carried out using ozone. Subsequently, the O_2+O dissociation limit and the spin–orbit interaction of these lowest excited triplet states were addressed in a theoretical study.[233] Two different studies[236,237] led to the development of a PES for the ground state ozone molecule along with its eight low lying triplet states. Finally, computational calculations

suggested that no triplet states are considered to be located below the molecular dissociation limit, thus O_2 and radical O cannot be formed.[238]

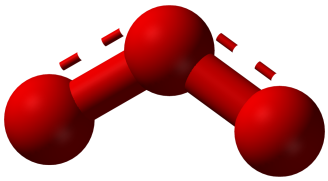

Fig. 6.2: The equilibrium ground state structure of ozone.

A number of studies on ozone have been focused on obtaining potential energy surfaces with various levels of accuracy and theory. Efforts to construct analytical PESs have been presented and also molecular dynamics simulations such as MCTDH have been used to study the dissociation and the transition process of the ozone molecule.[239] Overall, two different potential energy surface fits have been reported, one for the low-lying singlet–triplet transition and the other one for the near-equilibrium ground state of ozone molecule.[240–245]

6.4.3 Analysis

Fitted Potential Energy Surfaces

The study of the lowest three energy PESs in ozone was one of the first cases revealing that in molecules with little or no symmetry CoIs can still occur and they are known as accidental CoIs. Ozone features two minima with different symmetry which are separated by a transition state found close to the $\tilde{A}(^1A_2)$-$\tilde{B}(^1B_1)$ CoI.[246] Here, ozone is considered to have C_{2v} symmetry in the ground state. The results from the computational study employing a 3-state model with DD-vMCG and GAP-vMCG methods including all degrees of freedom are presented. The diabatic and adiabatic potential energy surfaces, and also the CoIs have been calculated and characterised along the symmetric stretching coordinate which corresponds to the ν_1 vibrational mode, the asymmetric stretching coordinate which corresponds to the ν_3 vibrational mode and the bond angle which corresponds to the ν_2 vibrational

mode as evaluated at a SA-CASSCF/6-311+G* level of theory. The PESs of ozone are quite complex, especially those of the symmetric stretching coordinate (ν_1) as changes in the symmetry can vary the position of the crossings.

Fig 6.3 shows one-dimensional cuts of the PESs along the ν_1 mode. A crossing between the $^1B_1$ and the more optically active $^1A_2$ state is taking place just before the Franck–Condon point, and can be observed both in the adiabatic and the diabatic PESs by employing the two methods under investigation. The PESs results when the GAP-vMCG method is employed, Figs. 6.3(c) and 6.3(d), are identical to those obtained when DD-vMCG is employed.

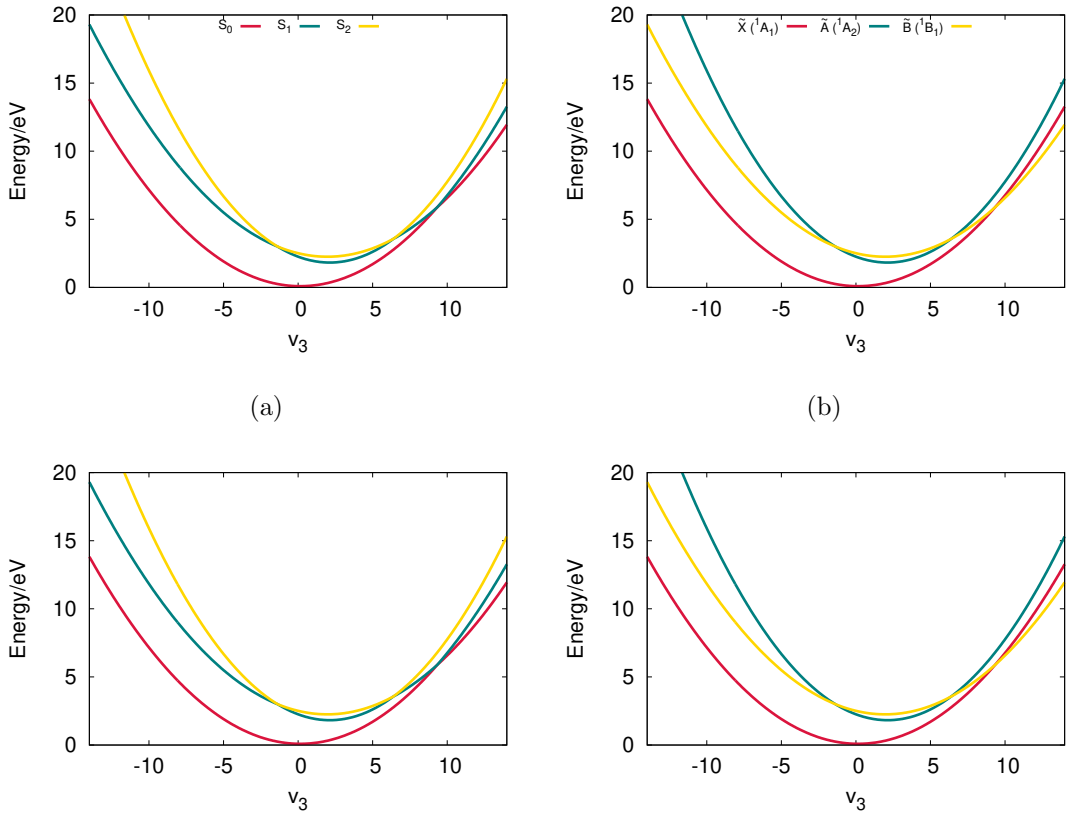

Fig. 6.3: One-dimensional cuts through the a) adiabatic and b) diabatic potential energy surfaces employing DD-vMCG, and the c) adiabatic and d) diabatic potential energy surfaces employing the GAP-vMCG method for ozone, in the space of the symmetric O-O bond stretch, ν_1, normal mode. All other coordinates have a value of 0.

It is worth noting that the symmetric mode is coupled to the asymmetric and

thus different values could affect the PESs and a possible CoI. As appeared in the work of Batista and Miller[247] the gap between the states will increase as the value of the asymmetric stretch coordinate rises. In the case where, similarly to the approach in our study, the rest of the coordinates are set equal to zero, the aforementioned CoI occurs. This is ascribed to the small coupling between the symmetric and asymmetric stretch coordinates leading to vibronic coupling between the two electronic excited states. The ground state ($1^1A'$) is quite well separated from the electronic excited states. However, in the positive displacement direction a crossing occurs at high energies and small angles according to literature.[248] Thus, here that the angle is zero some crossings that are not experimentally observed are expected.

Plotting the asymmetric coordinate ν_3 for the adiabatic picture, Figs. 6.4(a) and 6.4(c), the topology of the $^1A_2$ state is quite different compared to the $^1B_1$ state which has a shape of a double well with a barrier at the Franck–Condon point controlling the point of maximum proximity between these two electronic excited states and equilibrium positions that lead to dissociation of the molecule that are symmetrically located on both sides of the barrier, progressively farther away from the origin and further stabilized as the molecule is extended along the symmetric stretch coordinate. The equilibrium positions that can result in a possible dissociation of ozone are symmetrically located about the barrier. The adiabatic surfaces are in agreement with other computational work.[247] The diabatic PESs using both methods show the strong coupling between the two excited states. Once more the results prove that GAP-vMCG can successfully describe the dynamics of ozone. It is worth noting that similarly with the formamide example in Chapter 4, areas that are not sampled with vMCG give harmonic surfaces which explains why we do not get flat asymptotic surfaces as expected along the dissociative asymmetric coordinate.

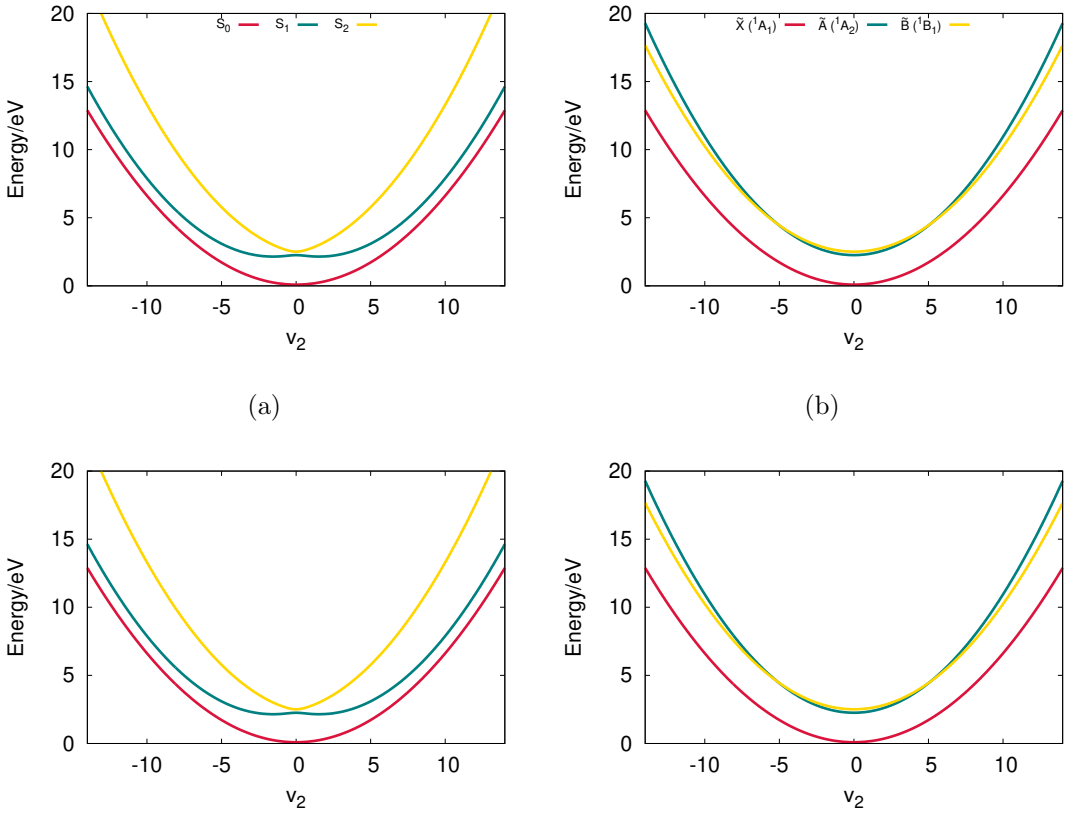

(a) (b)

(c) (d)

Fig. 6.4: One-dimensional cuts through the a) adiabatic and b) diabatic potential energy surfaces employing DD-vMCG, and the c) adiabatic and d) diabatic potential energy surfaces employing the GAP-vMCG method for ozone, in the space of the asymmetric O-O bond stretch, ν_3, normal mode. All other coordinates have a value of 0.

As it has been proved in different studies,[245–248] the bend angle coordinate does not take part in the photodissociation dynamics of ozone. The PESs along this mode are generally considered to be bound for a broad range of configurations. Comparing both the adiabatic, Figs. 6.5(a) and 6.5(c), and the diabatic, Figs. 6.5(b) and 6.5(d), potential energy surfaces it is again obvious that highly accurate results can be obtained by employing GAP-vMCG.

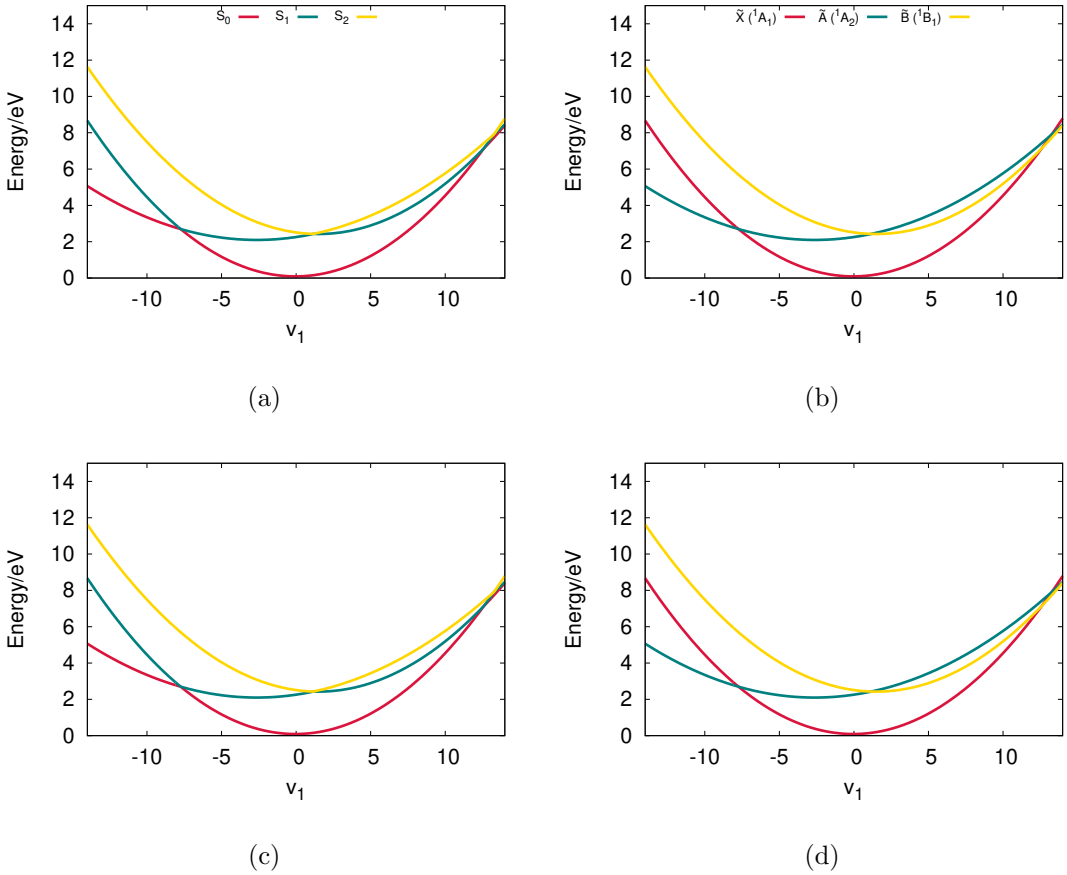

Fig. 6.5: One-dimensional cuts through the a) adiabatic and b) diabatic potential energy surfaces employing DD-vMCG, and the c) adiabatic and d) diabatic potential energy surfaces employing the GAP-vMCG method for ozone, in the space of the O-O-O bond angle, ν_2, normal mode. All other coordinates have a value of 0.

Moreover, in the available literature both in some experimental and theoretical studies, the coordinate and energy axes are limited to a small area of the PESs which makes it harder to compare results. Thus, the adiabatic PESs for the three modes and for GAP-vMCG method were plotted by employing narrower axes. As

it can be seen in Figs. 6.3 - 6.5, the two methods produce identical PESs and thus only one method was used to compare with existing results. As Fig. 6.6 shows, the results from this study agree well with an existing theoretical study[247] where a semiclassical algorithm was employed which was claimed to be able to describe a nonadiabatic process. In the aforementioned paper, ozone was considered to have a C_s symmetry and only the two first excited states were plotted. As it can be seen, the results from GAP-vMCG are in great agreement with the existing outcomes. The ground state is well separated from the two excited states and also the position and energy of the occurring CoIs are consistent with literature. Small differences, like for example the avoided crossing between the S_1 and S_2 states in Fig. 6.6(a) occurring later compared to Fig. 6.6(b), are possibly due to the difference in symmetry in the two studies, and also that in the paper the rest of the coordinates have a non-zero value while in this study all other coordinates have a value of zero. Still, the figures selected for comparison were the ones with the rest of the coordinates being almost zero so that a more meaningful comparison could be achieved. The wider picture of the PESs presented in Figs. 6.3-6.5 is not extensively explored and thus apart from comparing the two methods under investigation, this section also offers the chance to further explore the photodissociation of ozone.

State Population Analysis

The diabatic state populations after excitation to the second excited state, $\tilde{B}(^1B_1)$, have been also plotted in an effort to examine the distribution of the total wavepacket and to further compare the two methods. As depicted in Fig. 6.7, a fast population transfer is taking place within the first 5 fs where almost 50% of the population is transferred to the $^1A_2$ state. Overall, the two methods have managed to accurately describe the state populations which is in accordance with the experimental finding as presented by Flöthman and coworkers.[249] Furthermore there is

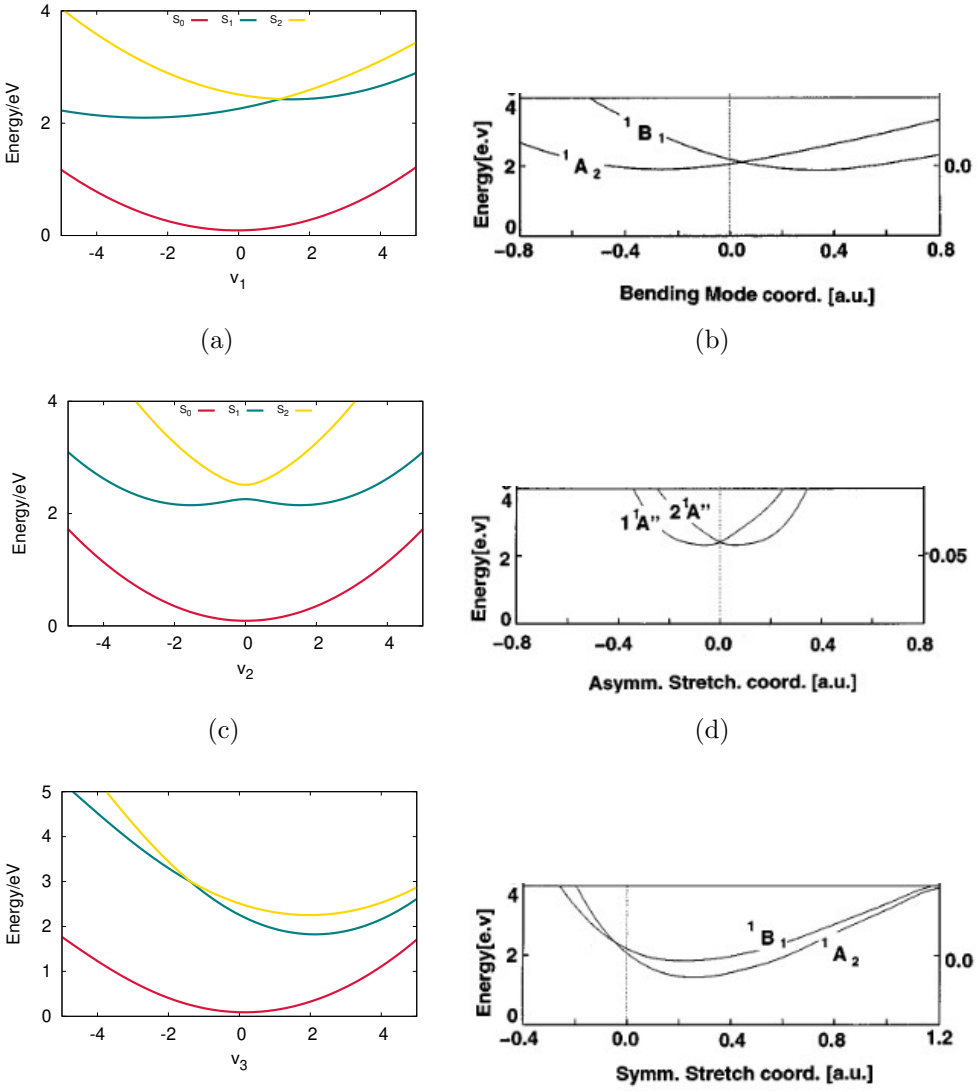

Fig. 6.6: One-dimensional cuts through the adiabatic potential energy surfaces along various coordinates obtained from DD-vMCG calculations (a,c,e) and (b,d,f) reprinted from Batista, V. S.; Miller, W. H.J. Chem. Phys. 1998, 108, 498–510, with the permission of AIP Publishing.

no population transfer to the ground state. The main difference is that when the DD-vMCG method was employed (Fig. 6.7(a)) the amount of the total population transfer at the beginning and more significantly at the end of the propagation is higher compared to Fig. 6.7(b) with the GAP-vMCG method. As a final note, the results above suggest that GAP-vMCG can efficiently and accurately generate diabatic state populations which are a good match to those with direct dynamics.

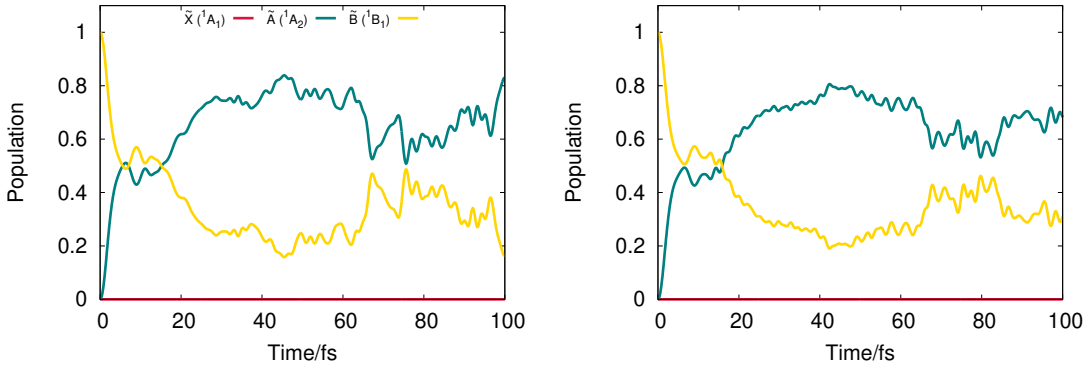

(a) (b)

Fig. 6.7: Normalised diabatic state populations from (a) DD-vMCG and (b) GAP-vMCG simulations of ozone starting with a vertical excitation to the $\tilde{B}(^1B_1)$ state for a 3-state model.

Moreover, a key feature of an accurate simulation is that the energy is conserved. During the simulation with both DD-vMCG and GAP-vMCG the energy was almost totally conserved throughout the calculation. More specifically for the case of LHA the maximum energy difference was 0.10 eV and for GAP was 0.12 eV. For this example the LHA approach seems to be more accurate but the difference is extremely small and it would be thus more accurate to say that the two methods had the same performance in terms of total energy conservation.

Hyperparameters

In this work the hyperparameters have been adjusted in the input file of the GAP-vMCG calculation to attain the best possible performance. To illustrate the importance of hyper-parameter selection, the effect of the hyperparameters and more

specifically the α parameter which controls the length-scale is now examined. The choice of the length-scale affects the kernel employed to determine the prior normal distribution in the functional space and to efficiently expand the potential energy surface.

In order to examine the effect of the α parameter on the PESs, the same calculations with varying α parameter were conducted. During these calculations, quantum chemistry calculations were excluded so that the code only reads the database which includes 2841 points and calculates the PESs from the database. All the remaining parameters have been kept constant. Moreover, for this comparison the adiabatic surfaces for the bond angle coordinate were plotted. As it can be seen in Fig. 6.8, smaller α values which means a much wider Gaussian kernel lead to smoother PESs. However, GAP-vMCG faces problems in describing the potentials at very high displacements even for small values of α. This failure was also observed in the case of butatriene. This feature is attributed to the fact that GAP employs Gaussian functions. Additionally in the case of α equal to 5 and 1, the Gaussians are narrower which makes the covariance matrix approach the unit matrix; there would likely be more problems with matrix becoming singular for small α. With large α the Gaussians decay to zero quickly so this is why the potential lacks smoothness; there need to be more DB points between the ones already there.

These results strongly indicate that the α parameter significantly affects the shape of the PESs and shows how important it is for it to be properly optimized and not manually selected; the purpose of a computational method is to be able to explore areas of the dynamics that are unknown and thus no validation results will exist like in this case where it was possible to rerun calculations with different parameters to match the results obtained from DD-vMCG. In other words, this optimisation at each step will give great flexibility to the method.

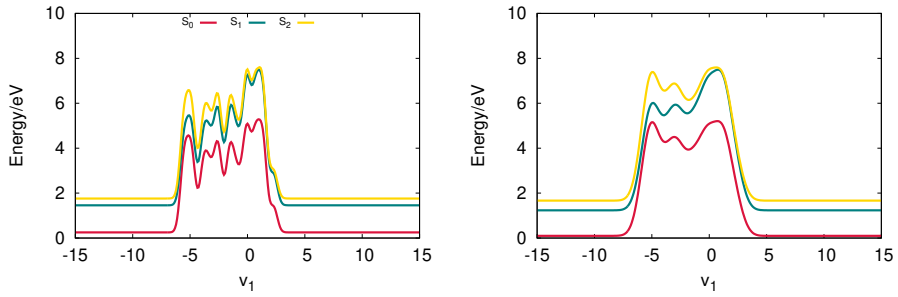

(a) $\alpha = 5$

(b) $\alpha = 1$

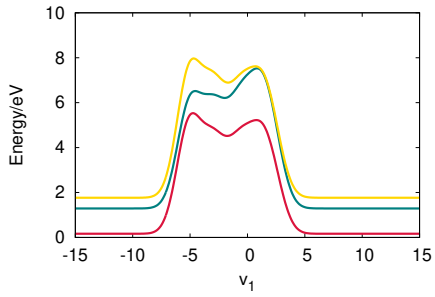

(c) $\alpha = 0.5$

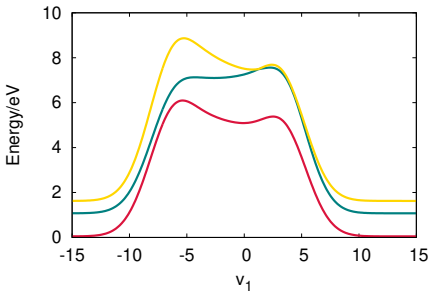

(d) $\alpha = 0.1$

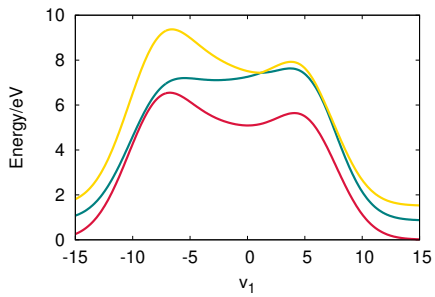

(e) $\alpha = 0.05$

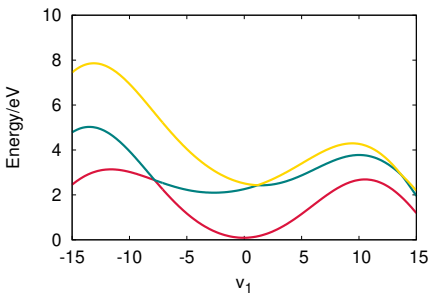

(f) $\alpha = 0.01$

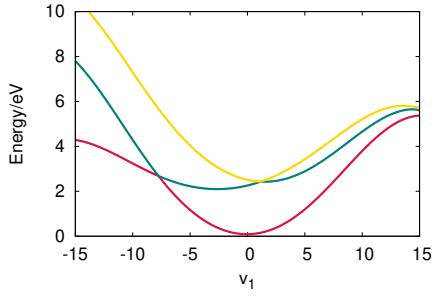

(g) $\alpha = 0.005$

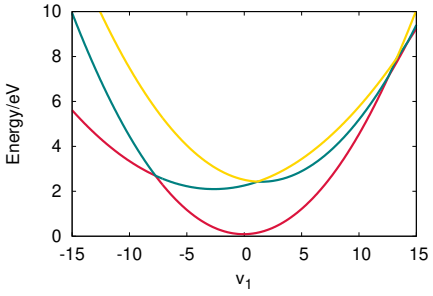

(h) $\alpha = 0.001$

Fig. 6.8: One-dimensional cuts through the adiabatic potential energy surfaces varying the α hyperparameter and employing the GAP-vMCG method for ozone, in the space of the O-O-O bond angle, ν_2, normal mode. All other coordinates have a value of 0.

Efficiency Analysis

Finally, the code dealing with the GAP-vMCG method was developed in order to benefit from the local DBs presented in Chapter 4. The results were not successful as GAP needs significantly more points compared to LHA as just the energies are going to be used. The way the GAP-vMCG method is structured could not benefit from the local DBs approach since the shape of the PESs that each GWP needs to describe at a specific time interval is more complicated and the points at each local DB cannot be defined as a circle of closest points like in the case of the DD-vMCG method. A direct comparison of the different total timings needed for each method for the same propagation is very difficult to conduct since different databases are used.

The DD-vMCG method was always significantly faster compared to the GAP scheme when calculations with the same number of GWPs and total propagation time were used. Especially when the local DBs approach is employed then the computational cost significantly drops. For the results presented in this chapter using 20 GWPs for 100 fs, the total computation time for GAP-vMCG was 3,746 minutes with 2841 points in the database, for DD-vMCG was 449 minutes with the full DC database and for DD-vMCG with local DBs was 117 minutes with 984 total points in the database. It is important to note that these timings refer to the serial calculations where no new points were added in the database but only the existing ones were read, and all the remaining common parameters between the methods have been kept constant.

However, these time differences do not principally depend on the number of total points in the two databases which is quite a small number in both cases, but mostly on the way GAP-vMCG works. More specifically, GAP-vMCG offers the option to use kernel functions that are localised, which corresponds to standard GAP, or kernel functions that are spread out where a manually selected order of

additive GAP is employed. When the second option is used, for example if a second order additive kernel is selected, the total time of the calculation is severely affected as there are 6 integrals per datapoint, 1 each per DOF and per pair of DOFs due to the form of the GAP kernel, compared to just 1 for the first option and thus the calculation would take about 6 times longer. In our case the only way to get state populations and sensible PESs was by using a second order which played a crucial role in the computational cost of ozone propagation when GAP-vMCG was employed.

6.5 Discussion and Future Work

In this chapter, the theoretical framework around Gaussian process regression has been presented along with its implementation to the DD-vMCG method which led to the GAP-vMCG method. Benchmark calculations on ozone have been performed aiming to compare the efficiency and accuracy of these two methods. To examine the accuracy, the results from the fitting of adiabatic and diabatic PESs and the diabatic state populations using both the DD-vMCG and the GAP-vMCG methods were investigated. GAP results are in great agreement with the ones generated by employing the LHA approach and also experimental findings. Thus, it can be concluded that the GAP approach can be employed in order to approximate potential energy surface matrix elements, which are fundamental for vMCG calculations, in a very straightforward way.

In an effort to further unravel the performance of GAP, the role of the α hyperparameter was examined by altering its value and running identical GAP-vMCG calculations. It was proved that this parameter has a high impact on the dynamics where the shape of the PES was severely changed and sometimes lead to completely unreliable results. The results showed the most important drawback of this approach is that hyperparameters are manually selected at the current

implementation.

With regards to efficiency, DD-vMCG and especially the small DBs approach requires significantly less computational effort compared to GAP-vMCG. This time difference depends on the fewer database points in DD-vMCG for the same molecule and with the same settings, but most importantly on the way GAP-vMCG works and the selection of the additive kernel which in the ozone case was the only way to get sensible results.

Despite the issues, GPR could be a promising approach to replace LHA in order to improve the accuracy of the DD-vMCG method. However, it should be noted that important strategies should be pursued in various directions. Firstly, the most important step is to optimise the hyperparameters. Various studies have claimed that an appropriate selection of the kernel hyperparameters has a significant effect on the performance of the GPR algorithm. More specifically, tuning of the hyperparameters improves the fitting of the target model, the ability to be a generally applicable method and its accuracy, and minimizes the number of iterations needed for GPR learning. Thus, this optimisation constitutes a key element for successful GPR quantum dynamics simulations. One option to achieve optimisation is by employing cross-validation where the hyperparameters are optimized by minimising the errors.[199] Instead, the log marginal likelihood[250] can be maximized, which has the following form

$$\Theta = -\frac{1}{2}\mathbf{y}^T\mathbf{w} - \frac{1}{2}\log\left|\mathbf{A} + \sigma^2\mathbf{I}-\right| - \frac{M}{2}log2\pi \tag{6.31}$$

Moreover, it will be of a great benefit to take advantage of the error estimation that GPR offers. At every prediction, the algorithm can produce an error of the prediction that in the case of DD-vMCG, the prediction is the PES at a point $\mathbf{q}_i(t)$ of the configuration space. The user can then define a threshold up to which this prediction can be trusted or a new quantum chemistry calculation should be performed instead.

Currently, the GWP weights include only the potential energy values. These weights could be modified in order to also include the forces without additional cost regarding the PES calculation, as at the centre of a GWP the forces are already available. This approach should further improve the accuracy of the GAP-vMCG results.

Additionally, another important point is to include the gradients and Hessians from the quantum chemistry calculations as additional training data instead of just using the energies. Machine learning heavily relies on the amount and quality of data, thus a better description of the PES when our model is being trained will result in more accurate prediction of the PESs of unknown points in the configuration space.

Finally, one could think beyond GPR and the GAP-vMCG method and maybe try different machine learning algorithms as a way to eliminate the limitations introduced in DD-vMCG when the LHA scheme is employed. As an example, ANNs have been proved to be an excellent approach for fitting global PESs.[251]

Chapter 7

Conclusions and Future Work

This chapter presents the main outcomes of this research study. All the key findings are summarised along with future work recommendations based on the results. In this thesis, the results reflect the two main strands of this research work. Firstly, to improve the *Direct Dynamics Variational Multi-configurational Gaussian* method and test its limitations for different molecules. Further, the ultimate aim was to carry out investigations on molecules hitherto unfeasible by employing the improved DD-vMCG method.

Aiming to firstly improve the efficiency and the accuracy of DD-vMCG, an efficient parallel algorithm using local databases for the potential surfaces around each basis function has been established, which leads to an improved implementation of the method in the Quantics package. Benchmark calculations on butatriene cation, allene cation and formamide proved that the DD-vMCG method were able to provide good quality diabatic surfaces for multi-dimensional non-adiabatic simulations directly from a set of quantum chemistry calculations. Within the improvements, the update of the interpolation by employing a modified Shepard interpolation scheme was also carried out. Total energy and norm conservation are both adequate, demonstrating the stability of the interpolation scheme used.

Moreover, both the efficiency and accuracy of the new algorithm were examined by performing test calculations employing local databases of different sizes

and the full quantum chemistry database. Test calculations showed that including only the closest points during the propagation of each basis function leads to a significant speed up, solving a major bottleneck encountered by the DD-vMCG method when treating complex chemical systems. The speed up becomes even larger when using a parallel version of the algorithm, as well as more Gaussian wavepackets to describe the molecule under investigation. Smooth adiabatic and diabatic potential energy surfaces are produced, as well as smooth couplings between the diabatic states. The novelty of this development work is in making DD-vMCG a competitive, efficient and accurate method for nonadiabatic direct quantum dynamics simulations. Systems that were not computationally feasible can be now efficiently treated with the improved implementation.

Following the aforementioned improved algorithm for DD-vMCG has made possible the successful study of the full dimensional photo-dissociation dynamics of phenol. This theoretical study by including for the first time five excitation states showed the importance of designing models with more states than the target ones in order to have a better description for the molecule under investigation. It has been shown that for phenol the 3-state model has to be completely abandoned and even the 4-state model that clearly offers a significantly better description of the dynamics is still not enough to match the experimental findings. This outcome is especially important for the dynamics of molecules which are strongly affected by conical intersections. Moreover, the analysis of the diabatic state population results suggest that the 6-state model after excitation to the $\tilde{A}$ state can best describe the population transfer and distribution between the states and also the rate of the dissociation which matches the experimental findings.

Important conclusions regarding the decay mechanism have also been presented by computing the diabatic state populations and the flux distribution into the different states. It is clear that the dissociation pathways provided by the conical

intersections between the $1^1\pi\sigma^*$ and the $^1\pi\pi^*$ and $^1\pi\pi$ states is accessible during the phenol dynamics, offering a rapid relaxation to the ground state.

Beyond the successful description of the photodissociation of phenol, this study illustrates the potential of the DD-vMCG method as it is capable of capturing the complete quantum picture of the coupled nuclear and electronic motions after photo-excitation into multiple states for a molecule like phenol with 33 vibrational modes. Additionally, a comparison analysis with existing models where the PESs were obtained analytically showed that DD-vMCG can not only reproduce these PESs but also generate smoother surfaces with better defined states and conical intersections between them. The less computational effort combined with the higher accuracy and the significant flexibility over analytically calculated PESs confirmed the great advantage of using DD-vMCG.

After dealing with the time needed to read, sort and analyse the database which was the main bottleneck that DD-vMCG was encountering, the LHA approach for calculating the potential energy surface matrix elements was found to be responsible for accuracy errors and computational delays. Benchmark calculations on ozone showed that results when GAP-vMCG is employed are in great agreement with the ones generated by employing the LHA approach and also experimental findings. Thus, it can be concluded that the GAP approach can be employed instead of LHA in order to approximate potential energy surface matrix elements, which are fundamental for vMCG calculations, in a very straightforward way. There are however some drawbacks to this approach such as the manual selection of the hyperparameters resulting in a less flexible method and also an increase in the computational effort compared to DD-vMCG.

A natural extension of this work will be to treat larger chemical systems with the developed DD-vMCG version and further to compare the outcomes and performance with other available quantum molecular dynamics methods such as tra-

jectory surface hopping.[252] Moreover, the photodissociation dynamics of phenol can be further studied by conducting quantum dynamics simulations with DD-vMCG to the phenoxyl radical. Also, since phenol is a major component of the green fluorescent protein chromophore, the successful characterization of the photodissociation of phenol accompanied with the methodological improvements of DD-vMCG offers the appropriate knowledge and confidence to study and apply this method to green fluorescent protein. Finally, future work should focus on the improvement and development of the existing code dealing with the very promising GAP approach. The implementation is at an initial stage and important strategies should be pursued in various directions to improve the performance of GAP-vMCG in order to completely abandon the LHA approach. The most important step towards the latter improvement is to optimise the hyper-parameters.

Bibliography

[1] Curchod, B.; Martínez, T. *Chem. Rev.* **2018**, *118*, 3305–3336.

[2] Ben-Nun, M.; Martínez, T. J. *Adv. Chem. Phys.* **2002**, *121*, 439–512.

[3] Ben-Nun, M.; Quenneville, J.; Martínez, T. *J. Phys. Chem. A* **2000**, *104*, 5172–5175.

[4] Jablonski, A. *Nature* **1933**, *131*, 839–840.

[5] Douhal, A.; Lahmani, F.; Zewail, A. H. *Chem. Phys.* **1996**, *207*, 477–498.

[6] Dantos, M.; Rosker, M. J.; Zewail, A. H. *J. Chem. Phys.* **1988**, *89*, 6128–6140.

[7] Rose, T. S.; Rosker, M. J.; Zewail, A. H. *J. Chem. Phys.* **1989**, *91*, 7415–7436.

[8] Zewail, A. H. *Science* **1988**, *242*, 1645–1653.

[9] Krausz, F.; Ivanov, M. *Rev. Mod. Phys.* **2009**, *81*, 163–234.

[10] Kling, M. F.; Vrakking, M. J. J. *Ann. Rev. Phys. Chem.* **2008**, *59*, 463–492.

[11] Born, M.; Oppenheimer, R. *Ann. Phys.* **1927**, *84*, 457–484.

[12] Schrödinger, E. *Phys. Rev.* **1926**, *28*, 1049–1070.

[13] Varandas, A. J. C. In *Conical intersections: electronic structure, dynamics & spectroscopy*; Domcke, W., Yarkony, D., Köppel, H., Eds.; World Scientific: River Edge, N. J., 2004; Vol. 15; pp 205–270.

[14] Murrell, J.; Carter, S.; Farantos, S.; Huxley, P.; Varandas, A. *Molecular Potential Energy Functions*; Wiley: Chichester, 1984; cited By 835.

[15] Varandas, A. J. C. In *Reaction and Molecular Dynamics*; Laganá, A., Riganelli, A., Eds.; Springer-Verlag: Berlin Heidelberg, 2000; Vol. 75; pp 33–56.

[16] Hui, Z. J. Z. *Theory and application of quantum molecular dynamics*; World Scientific: Singapore, 1998.

[17] Varandas, A. *Int. Rev. Phys. Chem.* **2000**, *19*, 199–245.

[18] Worth, G. A.; Robb, M. A.; Lasorne, B. L. *Mol. Phys.* **2008**, *106*, 2077–2091.

[19] Worth, G. A. Efficient Searching of Relevant Configuration Space: Direct Dynamics and the DD-vMCG Method. Multi-Dimensional Potential Energy Surfaces. Daresbury, U.K., 2008; pp 79–87.

[20] Chalfie, M.; Tu, Y.; Euskirchen, G.; Ward, W.; Prasher, D. *Sci.* **1994**, *263*, 802–805.

[21] Worth, G. A.; Giri, K.; Richings, G. W.; Beck, M. H.; Jäckle, A.; Meyer, H.-D. Quantics package, Version 1.1. 2015.

[22] Barford, W. *Lecture notes for Advanced Quantum Mechanics*; 2014.

[23] Min, S. K.; Agostini, F.; Tavernelli, I.; Gross, E. K. U. *J. Phys. Chem. Lett.* **2017**, *8*, 3048–3055.

[24] Curchod, B. F. E.; Penfold, T. J.; Rothlisberger, U.; Tavernelli, I. *Phys. Rev. A* **2011**, *84*, 42507.

[25] Granucci, G.; Persico, M.; Spighi, G. *J. Chem. Phys.* **2012**, *137*, 22A501.

[26] Richter, M.; Marquetand, P.; González-Vázquez, J.; Sola, I.; González, L. *J. Chem. Theo. Comp.* **2011**, *7*, 1253–1258.

[27] Mai, S.; Marquetand, P.; González, L. *Int. J. Quant. Chem.* **2015**, *115*, 1215–1231.

[28] Shalashilin, D. V. *J. Chem. Phys.* **2009**, *130*, 244101–244111.

[29] Shalashilin, D. V. *J. Chem. Phys.* **2010**, *132*, 244111.

[30] Kapral, R. *Annu. Rev. Phys. Chem.* **2006**, *57*, 129–157.

[31] Agostini, F.; Abedi, A.; Suzuki, Y.; Gross, E. *Mol. Phys.* **2013**, *111*, 3625–3640.

[32] Poirier, B.; Parlant, G. *J. Phys. Chem. A* **2007**, *111*, 10400–10408.

[33] Atkins, P. W. *Molecular Quantum Mechanics*, 2nd ed.; OUP: Oxford, U.K., 1983.

[34] Böhm, A. *Quantum Mechanics: Foundations and Applications*; Springer: New York, 1986.

[35] Zettili, N. *Quantum Mechanics: Concepts and Applications*, 2nd ed.; Wiley, 2009.

[36] Messiah, A. *Quantum Mechanics*; John Wiley: New York, 1962; Vol. 1; pp 222–228.

[37] Schatz, G. C.; Ratner, M. A. *Quantum Mechanics in Chemistry*; Prentice-Hall: Englewood Cliffs, NJ, 1993.

[38] Huggins, E. R. *Physics 2000 Non-calculus*; 2000; Chapter 33, pp 1–15.

[39] Mead, C. A.; Truhlar, D. G. *J. Chem. Phys.* **1979**, *70*, 2284–2296.

[40] Mead, C. A. *J. Chem. Phys.* **1980**, *72*, 3839–3840.

[41] Yarkony, D. R. *Rev. Mod. Phys.* **1996**, *68*, 985–1013.

[42] Kutzelnigg, W. *Mol. Phys.* **1997**, *90*, 909–916.

[43] Hinze, J.; Alijah, A.; Wolniewicz, L. *Pol. J. Chem.* **1998**, *72*, 1293–1303.

[44] Baer, M. *Phys. Rep.* **2002**, *358*, 75–142.

[45] Kendrick, B. K.; Mead, C. A.; Truhlar, D. G. *Chem. Phys.* **2002**, *277*, 31–41.

[46] Atchity, G. J.; Xantheas, S. S.; Ruedenberg, K. *J. Chem. Phys.* **1991**, *95*, 1862–1876.

[47] Baer, M. *Chem. Phys. Lett* **1975**, *35*, 112–118.

[48] Helgaker, T.; Jorgensen, P.; Olsen, J. *Molecular electronic-structure theory*; John Wiley & Sons: New York, 2014.

[49] Yarkony, D. *Modern electronic structure theory*; World Scientific, 1995; Vol. 2.

[50] Herzberg, G.; Longuet-Higgins, H. C. *Discuss. Farad. Soc.* **1963**, *35*, 77.

[51] Lee, T. J.; Fox, D. J.; Schaefer III, H. F.; Pitzer, R. M. *J. Chem. Phys.* **1984**, *81*, 356–361.

[52] Truhlar, D. G.; Steckler, R.; Gordon, M. S. *Chem. Rev.* **1987**, *87*, 217–236.

[53] Manthe, U.; Köppel, H. *J. Chem. Phys* **1990**, *93*, 1658–1669.

[54] Helgaker, T.; Uggerud, E.; Jensen, H. J. A. *Chem. Phys. Lett.* **1990**, *173*, 145–150.

[55] Amatatsu, Y.; Morokuma, K.; Yabushita, S. *J. Chem. Phys.* **1991**, *94*, 4858.

[56] Head, J. D.; Weiner, B.; Zerner, M. C. *Int. J. Quantum Chem.* **1988**, *33*, 177–186.

[57] Schlegel, H. B. *J. Comput. Chem.* **2003**, *24*, 1514–1527.

[58] Mckee, M. L.; Page, M. In *Computing reaction pathways on molecular potential energy surfaces*; Lipkowitz, K. B., Boyd, D. B., Eds.; Wiley Online Library, 2007; pp 35–65.

[59] Schlegel, B. H. In *Modern Electronic Structure Theory:Part I*; Yarkony, D. R., Ed.; World Scientific, 1995; pp 459–500.

[60] Van der Lugt, W. T. A. M.; Oosterhoff, L. J. *J. Am. Chem. Soc.* **1969**, *91*, 6042–6049.

[61] Michl, J. *Mol. Photochem.* **1972**, *4*, 243.

[62] Teller, E. *J. Phys. Chem.* **1937**, *41*, 109–116.

[63] Zimmerman, H. E. *J. Am. Chem. Soc.* **1966**, *88*, 1566.

[64] Curchod, B. F. E.; Agostini, F. *J. Phys. Chem. Lett.* **2017**, *8*, 831–837.

[65] Bernardi, F.; Olivucci, M.; Robb, M. A. *Chem. Soc. Rev.* **1996**, *25*, 321–328.

[66] Robb, M. A.; Bernardi, F.; Olivucci, M. *Pure Appl. Chem.* **1995**, *67*, 783 – 789.

[67] Cederbaum, L. S.; Friedman, R. S.; Ryabov, V. M.; Moiseyev, N. *Phys. Rev. Lett* **2003**, *90*, 13001.

[68] Von Neumann, J.; Wigner, E. In *Quantum Chemistry: Classic Scientific Papers*; Hettema, H., Ed.; World Scientific, 2000; Vol. 8; pp 25–31.

[69] Bearpark, M. J.; Blancafort, L.; Robb, M. A. *Mol. Phys.* **2002**, *100*, 1735–1739.

[70] Boggio-Pasqua, M.; Ravaglia, M.; Bearpark, M. J.; Garavelli, M.; Robb, M. A. *J. Phys. Chem.* **2003**, *107*, 11139–11152.

[71] Palmer, I. J.; Ragazos, I. N.; Bernardi, F.; Olivucci, M.; Robb, M. A. *J. Am. Chem. Soc.* **1993**, *115*, 672–682.

[72] Barckholtz, T. A.; Miller, T. A. *J. Phys. Chem. A* **1999**, *103*, 2321–2336.

[73] Barckholtz, T. A.; Miller, T. A. *Int. Rev. Phys. Chem.* **1998**, *17*, 435–524.

[74] Stolow, A.; Bragg, A. E.; Neumark, D. M. *Chem. Rev.* **2004**, *104*, 1719–1757.

[75] Ben-Nun, M.; Martínez, T. J. *Chem. Phys. Lett.* **1998**, *298*, 57–65.

[76] Hartree, D. R. *Math. Proc. Cam. Phil. Soc.* **1928**, *24*, 89–110.

[77] Hartree, D. R. *Math. Proc. Cam. Phil. Soc.* **1928**, *24*, 111–132.

[78] Pauli, W. *Phys. Rev.* **1940**, *58*, 716–722.

[79] Slater, J. *Quantum Theory of Atomic Structure*; International series in pure and applied physics; McGraw-Hill: New York, 1960.

[80] Spinlove, K. E.; Vacher, M.; Bearpark, M.; Robb, M. A.; Worth, G. A. *Chem. Phys.* **2017**, *482*, 52–63.

[81] Frisch, M. J.; Trucks, G. W.; Schlegel, H. B.; Scuseria, G. E.; Robb, M. A.; Cheeseman, J. R.; Scalmani, G.; Barone, V.; Petersson, G. A.; Nakatsuji, H.; Li, X.; Caricato, M.; Marenich, A.; Bloino, J.; Janesko, B. G.; Gomperts, R.; Mennucci, B.; Hratchian, H. P.; Ort, J. V. Gaussian 09, Revision A.02. 2009; `www.gaussian.com`.

[82] Richings, G. W.; Polyak, I.; Spinlove, K. E.; Worth, G. A.; Burghardt, I.; Lasorne, B. *Int. Rev. Phys. Chem.* **2015**, *34*, 269–308.

[83] Anderson, K.; Malmqvist, P.-Å.; Roos, B. O.; Sadlej, A. J.; Wolinski, K. *J. Phys. Chem.* **1990**, *94*, 5483–5488.

[84] Møller, C.; Plesset, M. S. S. *Phys. Rev.* **1934**, *46*, 618–622.

[85] Szabo, A.; Ostlund, N. S. *Modern Quantum Chemistry*; McGraw Hill: New York, 1989.

[86] Dreuw, A.; Wormit, M. *WIREs Comput. Mol. Sci.* **2015**, *5*, 82–95.

[87] Bartlett, R. J.; Musiał, M. *Rev. Mod. Phys.* **2007**, *79*, 291–352.

[88] Marques, M. A., Maitra, N. T., Nogueira, F. M., Gross, E., Rubio, A., Eds. *Fundamentals of Time-Dependent Density Functional Theory*; Lecture Notes in Physics; Springer: Berlin Heidelberg, 2012; Vol. 837.

[89] Roos, B. O.; Taylor, P. R.; Siegbahn, P. E. M. *Chem. Phys.* **1980**, *48*, 157–173.

[90] Knowles, P. J.; Werner, H.-J. *Chem. Phys. Lett.* **1985**, *115*, 259–267.

[91] Andersson, K.; Malmqvist, P.-Å.; Roos, B. O. *J. Chem. Phys.* **1992**, *96*, 1218–1226.

[92] Tully, J. C. *J. Chem. Phys* **1990**, *93*, 1061–1071.

[93] Meyer, H.-D.; Manthe, U.; Cederbaum, L. S. *Chem. Phys. Lett.* **1990**, *165*, 73–78.

[94] Meyer, H.-D.; Worth, G. A. *Theo. Chem. Acc.* **2003**, *109*, 251–267.

[95] Manthe, U.; Meyer, H.-D.; Cederbaum, L. S. *J. Chem. Phys* **1992**, *97*, 3199–3213.

[96] Thomas, L. H. *Math. Proc. Cam. Phil. Soc.* **1927**, *23*, 542–548.

[97] Kuleff, A. L.; Cederbaum, L. S. *J. Phys. B* **2014**, *47*, 124002.

[98] Beck, M. H.; Meyer, H.-D. *Z. Phys. D* **1997**, *42*, 113–129.

[99] Burghardt, I.; Meyer, H.-D.; Cederbaum, L. S. *J. Chem. Phys.* **1999**, *111*, 2927–2938.

[100] Burghardt, I.; Giri, K.; Worth, G. A. *J. Chem. Phys.* **2008**, *129*, 174104–174114.

[101] Burghardt, I.; Nest, M.; Worth, G. A. *J. Chem. Phys.* **2003**, *119*, 5364–5378.

[102] Dirac, P. A. M. *Proc. Cambridge Philos. Soc.* **1930**, *26*, 376–385.

[103] McLachlan, A. D. *Mol. Phys.* **1964**, *8*, 39.

[104] Frenkel, J. *Wave Mechanics*; Clarendon Press: Oxford, U.K., 1934.

[105] Meyer, H.-D. *Introduction to MCTDH: Lecture Notes*; 2011.

[106] Worth, G. A.; Robb, M. A.; Burghardt, I. *Faraday Discuss.* **2004**, *127*, 307–323.

[107] Worth, G. A.; Burghardt, I. *Chem. Phys. Lett.* **2003**, *368*, 502–508.

[108] Lasorne, B.; Robb, M. A.; Worth, G. A. *Phys. Chem. Chem. Phys.* **2007**, *9*, 3210–3227.

[109] Richings, G. W.; Worth, G. A. *J. Phys. Chem. A* **2015**, *119*, 12457–12470.

[110] Fock, V. *Z. Phys.* **1930**, *61*, 126–148.

[111] Bohr, N. *Z. Phys.* **1922**, *9*, 1–67.

[112] Worth, G. A.; Hunt, P.; Robb, M. A. *J. Phys. Chem. A* **2003**, *107*, 621–631.

[113] Crespo-Otero, R.; Barbatti, M. *Chem. Rev.* **2018**, *118*, 7026–7068.

[114] Curchod, B. F. E.; Rothlisberger, U.; Tavernelli, I. *Chemphyschem* **2013**, *14*, 1314–1340.

[115] Collins, M. A.; Zhang, D. H. *J. Chem. Phys.* **1999**, *111*, 9924–9931.

[116] Ischtwan, J.; Collins, M. A. *J. Chem. Phys.* **1994**, *100*, 8080–8088.

[117] Frankcombe, T. J.; Collins, M. A.; Worth, G. A. *Chem. Phys. Lett.* **2010**, *489*, 242–247.

[118] Lasorne, B.; Bearpark, M. J.; Robb, M. A.; Worth, G. A. *J. Phys. Chem. A* **2008**, *112*, 13017–13027.

[119] Araújo, M.; Lasorne, B.; Magalhães, A. L.; Worth, G. A.; Bearpark, M. J.; Robb, M. A. *J. Chem. Phys.* **2009**, *131*, 144301–144308.

[120] Allan, C. S. M.; Lasorne, B.; Worth, G. A.; Robb, M. A. *J. Phys. Chem. A* **2010**, *114*, 8713–8729.

[121] Mendive-Tapia, D.; Lasorne, B.; Worth, G. A.; Robb, M. A.; Bearpark, M. J. *J. Chem. Phys.* **2012**, *548*, 22A548–10.

[122] Lasorne, B.; Bearpark, M. J.; Robb, M. A.; Worth, G. A. *Chem. Phys. Lett.* **2006**, *432*, 604–609.

[123] Beck, M. H.; Jäckle, A.; Worth, G. A.; Meyer, H.-D. *Phys. Rep.* **2000**, *324*, 1–105.

[124] Thompson, K. C.; Jordan, M. J. T.; Collins, M. A. *J. Chem. Phys.* **1998**, *108*, 8302–8316.

[125] Godsi, O.; Evenhuis, C. R.; Collins, M. A. *J. Chem. Phys.* **2006**, *125*, 104105.

[126] Bettens, R. P. A.; Collins, M. A. *J. Chem. Phys.* **1999**, *111*, 816–826.

[127] Jeffers, J.; Reinders, J.; Sodani, A. *Intel Xeon Phi Processor High Performance Programming*, 2nd ed.; Morgan Kaufmann: Boston, 2016; pp 3–13.

[128] Kirk, D.; Hwu, W.-M. W. *Programming Massively Parallel Processors*, 2nd ed.; Morgan Kaufmann: Boston, 2012; pp 1–21.

[129] Kirk, D.; Hwu, W.-M. W. *Programming Massively Parallel Processors*, 3rd ed.; Morgan Kaufmann: Boston, 2016; pp 1–18.

[130] Alessandrini, V. *Shared Memory Application Programming*; Morgan Kaufmann: Boston, 2015; pp 307–339.

[131] Wang, Z.; Ma, S.; Huang, L.; Lai, M.; Shi, W. *Networks-On-Chip*; Morgan Kaufmann: Oxford, 2015; pp 253 – 254.

[132] Brill, M.; Vendrell, O.; Meyer, H.-D. In *Advances in the Theory of Atomic and Molecular Systems*; Piecuch, P., Maruani, J., Delgado-Barrio, G., Wilson, S., Eds.; Progress in Theoretical Chemistry and Physics; Springer Netherlands: Dordrecht, 2009; Vol. 20; pp 67–80.

[133] Cederbaum, L. S.; Domcke, W.; Köppel, H.; von Niessen, W. *Chem. Phys.* **1977**, *26*, 169–177.

[134] Cattarius, C.; Worth, G. A.; Meyer, H.-D.; Cederbaum, L. S. *J. Chem. Phys.* **2001**, *115*, 2088–2100.

[135] Frisch, M. J.; Trucks, G. W.; Schlegel, H. B.; Scuseria, G. E.; Robb, M. A.; Cheeseman, J. R.; Montgomery Jr., J. A.; Vreven, T.; Kudin, K. N.; Burant, J. C.; Millam, J. M.; Iyengar, S. S.; Tomasi, J.; Barone, V.; Mennucci, B.; Cossi, M.; Scalmani, G.; Rega, N.; Petersson, G. A.; Nakatsuji, H.; Hada, M.; Ehara, M.; Toyota, K.; Fukuda, R.; Hasegawa, J.;

Ishida, M.; Nakajima, T.; Honda, Y.; Kitao, O.; Nakai, H.; Klene, M.; Li, X.; Knox, J. E.; Hratchian, H. P.; Cross, J. B.; Bakken, V.; Adamo, C.; Jaramillo, J.; Gomperts, R.; Stratmann, R. E.; Yazyev, O.; Austin, A. J.; Cammi, R.; Pomelli, C.; Ochterski, J. W.; Ayala, P. Y.; Morokuma, K.; Voth, G. A.; Salvador, P.; Dannenberg, J. J.; Zakrzewski, V. G.; Dapprich, S.; Daniels, A. D.; Strain, M. C.; Farkas, O.; Malick, D. K.; Rabuck, A. D.; Raghavachari, K.; Foresman, J. B.; Ortiz, J. V.; Cui, Q.; Baboul, A. G.; Clifford, S.; Cioslowski, J.; Stefanov, B. B.; Liu, G.; Liashenko, A.; Piskorz, P.; Komaromi, I.; Martin, R. L.; Fox, D. J.; Keith, T.; Al-Laham, M. A.; Peng, C. Y.; Nanayakkara, A.; Challacombe, M.; Gill, P. M. W.; Johnson, B.; Chen, W.; Wong, M. W.; Gonzalez, C.; Pople, J. A.; Montgomery, J. A.; Jr.,; Vreven, T.; Kudin, K. N.; Burant, J. C.; Millam, J. M.; Iyengar, S. S.; Tomasi, J.; Barone, V.; Mennucci, B.; Cossi, M.; Scalmani, G.; Rega, N.; Petersson, G. A.; Nakatsuji, H.; Hada, M.; Ehara, M.; Toyota, K.; Fukuda, R.; Hasegawa, J.; Ishida, M.; Nakajima, T.; Honda, Y.; Kitao, O.; Nakai, H.; Klene, M.; Li, X.; Knox, J. E.; Hratchian, H. P.; Cross, J. B.; Bakken, V.; Adamo, C.; Jaramillo, J.; Gomperts, R.; Stratmann, R. E.; Yazyev, O.; Austin, A. J.; Cammi, R.; Pomelli, C.; Ochterski, J. W.; Ayala, P. Y.; Morokuma, K.; Voth, G. A.; Salvador, P.; Dannenberg, J. J.; Zakrzewski, V. G.; Dapprich, S.; Daniels, A. D.; Strain, M. C.; Farkas, O.; Malick, D. K.; Rabuck, A. D.; Raghavachari, K.; Foresman, J. B.; Ortiz, J. V.; Cui, Q.; Baboul, A. G.; Clifford, S.; Cioslowski, J.; Stefanov, B. B.; Liu, G.; Liashenko, A.; Piskorz, P.; Komaromi, I.; Martin, R. L.; Fox, D. J.; Keith, T.; Al-Laham, M. A.; Peng, C. Y.; Nanayakkara, A.; Challacombe, M.; Gill, P. M. W.; Johnson, B.; Chen, W.; Wong, M. W.; Gonzalez, C. Gaussian 03, Revision C.02. 2003.

[136] Schmidt, B.; González-Domínguez, J.; Hundt, C.; Schlarb, M. *Parallel Pro-*

gramming: Concepts and Practice; Morgan Kaufmann: Mainz, 2018; pp 1–416.

[137] Cederbaum, L. S.; Domcke, W.; Köppel, H. *Chem. Phys.* **1978**, *33*, 319–326.

[138] Woywod, C.; Domcke, W. *Chem. Phys.* **1992**, *162*, 349–358.

[139] Mahapatra, S.; Worth, G. A.; Meyer, H.-D.; Cederbaum, L. S.; Köppel, H. *J. Phys. Chem. A* **2001**, *105*, 5567–5576.

[140] Worth, G. A.; Cederbaum, L. S. *Chem. Phys. Lett.* **2001**, *348*, 477–482.

[141] Werner, H.-J.; Knowles, P. J.; Knizia, G.; Manby, F. R.; Schütz, M.; Celani, P.; Györffy, W.; Kats, D.; Korona, T.; Lindh, R.; Mitrushenkov, A.; Rauhut, G.; Shamasundar, K. R.; Adler, T. B.; Amos, R. D.; Bernhardsson, A.; Berning, A.; Cooper, D. L.; Deegan, M. J. O.; Dobbyn, A. J.; Eckert, F.; Goll, E.; Hampel, C.; Hesselmann, A.; Hetzer, G.; Hrenar, T.; Jansen, G.; Köppl, C.; Liu, Y.; Lloyd, A. W.; Mata, R. A.; May, A. J.; McNicholas, S. J.; Meyer, W.; Mura, M. E.; Nicklass, A.; O'Neill, D. P.; Palmieri, P.; Peng, D.; Pflüger, K.; Pitzer, R.; Reiher, M.; Shiozaki, T.; Stoll, H.; Stone, A. J.; Tarroni, R.; Thorsteinsson, T.; Wang, M. MOLPRO, version 2015.1, a package of ab initio programs. 2015; `http://www.molpro.net`.

[142] Freibert, A. Simulating Non-Adiabatic Photochemistry using Direct Quantum Dynamics. 7, 2019.

[143] Freibert, A. Simulating Non-Adiabatic Photochemistry using Direct Quantum Dynamics The Diabatisation Scheme in the DD-vMCG Method. 7, 2019.

[144] Kua, J.; Thrush, K. L. *J. Phys. Chem. B* **2016**, *120*, 8175–8185.

[145] Guzmán-Angel, D.; Inostroza-Rivera, R.; Gutiérrez-Oliva, S.; Herrera, B.; Toro-Labbé, A. *Theor. Chem. Acc.* **2016**, *135*, 10–37.

[146] Artoshina, O. V.; Vorobéva, M. Y.; Dushanov, E. B.; Kholmurodov, K. T. *Russ. J. Phys. Chem. A* **2014**, *88*, 951–958.

[147] Inostroza-Rivera, R.; Herrera, B.; Toro-Labbé, A. *Phys. Chem. Chem. Phys.* **2014**, *16*, 14489–14495.

[148] Nguyen, V. S.; Orlando, T. M.; Leszczynski, J.; Nguyen, M. T. *J. Phys. Chem. A* **2013**, *117*, 2543–2555.

[149] Bipp, H.; Kieczka, H. *Ullmann's Encyclopedia of Industrial Chemistry*; American Cancer Society, 2011.

[150] Saladino, R.; Crestini, C.; Pino, S.; Costanzo, G.; Di Mauro, E. *Phys. Life Rev.* **2012**, *9*, 84–104.

[151] Nguyen, V. S.; Abbott, H. L.; Dawley, M. M.; Orlando, T. M.; Leszczynski, J.; Nguyen, M. T. *J. Phys. Chem. A* **2011**, *115*, 841–851.

[152] Spinlove, K. E.; Richings, G. W.; Robb, M. A.; Worth, G. A. *Farad. Discuss.* **2018**, *212*, 191–215.

[153] Robin, M. *Higher excited states of polyatomic molecules*; Academic Press, 2012; Vol. 3.

[154] Crespo-Hernández, C.; Cohen, B.; Hare, P.; Kohler, B. *Chem. Rev.* **2004**, *104*, 1977–2019.

[155] Callis, P. *Annu. Rev. Phys. Chem.* **1983**, *34*, 329–357.

[156] Creed, D. *Photochem. Photobiol.* **1984**, *39*, 537–562.

[157] Reuther, A.; Iglev, H.; Laenen, R.; Laubereau, A. *Chem. Phys. Lett.* **2000**, *325*, 360–368.

[158] Nienhaus, K.; Nienhaus, G. *J. Phys. Condens. Matter* **2016**, *28*, 443001.

[159] Roberts, G. M.; Chatterley, A. S.; Young, J. D.; Stavros, V. G. *J. Phys. Chem. Lett.* **2012**, *3*, 348–352.

[160] Dixon, R. N.; Oliver, T. A. A.; Ashfold, M. N. R. *J. Chem. Phys.* **2011**, *134*, 194303.

[161] Pino, G. A.; Oldani, A. N.; Marceca, E.; Fujii, M.; Ishiuchi, S.-I.; Miyazaki, M.; Broquier, M.; Dedonder, C.; Jouvet, C. *J. Chem. Phys.* **2010**, *133*, 124313.

[162] Nix, M. G. D.; Devine, A. L.; Cronin, B.; Dixon, R. N.; Ashfold, M. N. R. *J. Chem. Phys.* **2006**, *125*, 133318.

[163] Zhu, X.; Malbon, C.; R. Yarkony, D. *J. Chem. Phys.* **2016**, *144*, 124312.

[164] Lan, Z.; Domcke, W.; Vallet, V.; Sobolewski, A.; Mahapatra, S. *J. Chem. Phys.* **2005**, *122*, 283–293.

[165] Schick, C. P.; Weber, P. M. *J. Phys. Chem. A* **2001**, *105*, 3725–3734.

[166] Sobolewski, A.; Domcke, W.; Dedonder-Lardeux, C.; Jouvet, C. *Phys. Chem. Chem. Phys* **2002**, *4*, 1093–1100.

[167] Sobolewski, A.; Domcke, W. *J. Phys. Chem. A* **2001**, *105*, 9275–9283.

[168] King, G. A.; Oliver, T. A. A.; Nix, M. G. D.; Ashfold, M. N. R. *J. Phys. Chem. A.* **2009**, *113*, 7984–7993.

[169] Iqbal, A.; Cheung, M. S. Y.; Nix, M. G. D.; Stavros, V. G. *J. Phys. Chem. A.* **2009**, *113*, 8157–8163.

[170] Hause, M.; Heidi Yoon, Y.; Case, A.; Crim, F. *J. Chem. Phys.* **2008**, *128*, 104307.

[171] Devine, A. L.; Cronin, B.; Nix, M. G. D.; Ashfold, M. N. R. *J. Chem. Phys.* **2006**, *125*, 184302–184309.

[172] Ashfold, M. N. R.; Devine, A. L.; Dixon, R. N.; King, G. A.; Nix, M. G. D.; Oliver, T. A. A. *Proc. Nat. Acad. Sci.* **2008**, *105*, 12701–12706.

[173] Ashfold, M. N. R.; Cronin, B.; Devine, A. L.; Dixon, R. N.; Nix, M. G. D. *Science* **2006**, *312*, 1637–1640.

[174] Yang, K. R.; Xu, X.; Zheng, J.; Truhlar, D. G. *Chem. Sci.* **2014**, *5*, 4661–4680.

[175] Lan, Z.; Domcke, W. *Chem. Phys.* **2008**, *350*, 125–138.

[176] King, G. A.; Oliver, T. A. A.; Ashfold, M. N. R. *J. Chem. Phys.* **2010**, *132*, 214307.

[177] Brand, U.; Hippler, H.; Lindemann, L.; Troe, J. *J. Phys. Chem.* **1990**, *94*, 6305–6316.

[178] Sevy, E. T.; Muyskens, M. A.; Rubin, S. M.; Flynn, G. W.; Muckerman, J. T. *J. Chem. Phys.* **2000**, *112*, 5829–5843.

[179] Ni, C.-K.; Tseng, C.-M.; Lin, M.-F.; Dyakov, Y. A. *J. Phys. Chem. B.* **2007**, *111*, 12631–12642.

[180] Lee, C.; Lin, Y.-C.; Lee, S.-H.; Lee, Y.-Y.; Tseng, C.-M.; Lee, Y.-T.; Ni, C.-K. *J. Chem. Phys.* **2017**, *147*, 013904.

[181] Sobolewski, A. L.; Domcke, W. *J. Phys. Chem. A* **2001**, *105*, 9275–9283.

[182] Zhu, X.; Yarkony, D. R. *J. Chem. Phys.* **2014**, *140*, 024112.

[183] Xie, C.; Ma, J.; Zhu, X.; Yarkony, D. R.; Xie, D.; Guo, H. *J. Am. Chem. Soc.* **2016**, *138*, 7828–7831.

[184] Andersson, K.; Blomberg, M. R. A.; Fülscher, M. P.; Karlström, G.; Lindh, R.; Malmqvist, P.; Neogrády, P.; Olsen, J.; Roos, B. O.; Sadlej, A. J.; Schütz, M.; Seijo, L.; Serrano-Andrés, L.; Siegbahn, P. E. M.; Widmark, P. O. MOLCAS, Version 4. 1997.

[185] Xu, X.; Zheng, J.; Yang, K. R.; Truhlar, D. G. *J. Am. Chem. Soc.* **2014**, *136*, 16378–16386.

[186] Xu, X.; Yang, K. R.; Truhlar, D. G. *J. Chem. Theory Comput.* **2013**, *9*, 3612–3625.

[187] Leforestier, C.; Wyatt, R. E. *J. Chem. Phys* **1983**, *78*, 2334.

[188] Kosloff, R.; Kosloff, D. *J. Comp. Phys.* **1986**, *63*, 363–376.

[189] Bist, H.; Brand, J.; Williams, D. *J. Mol. Spectrosc.* **1966**, *21*, 76–98.

[190] Fuh, R. C. *Phenol*; 1995.

[191] Vieuxmaire, O.; Lan, Z.; Sobolewski, A.; Domcke, W. *J. Chem. Phys.* **2008**, *129*, 224307.

[192] Lan, Z.; Domcke, W.; Vallet, V.; Sobolewski, A. L.; Mahapatra, S. *J. Chem. Phys.* **2004**, *127*, 224315.

[193] King, G.; Devine, A.; Nix, M.; Kelly, D.; Ashfold, M. *Phys. Chem. Chem. Phys.* **2008**, *10*, 6417–6429.

[194] Sur, A.; Johnson, P. *J. Chem. Phys.* **1986**, *84*, 1206–1209.

[195] Ebata, T.; Furukawa, M.; Suzuki, T.; Ito, M. *J. Opt. Soc. Am. B.* **1990**, *7*, 1890–1897.

[196] Nix, M. G. D.; Devine, A. L.; Dixon, R. N.; Ashfold, M. N. R. *Chem. Phys. Lett.* **2008**, *463*, 305–308.

[197] Christopoulou, G.; Freibert, A.; Worth, G. A. *J. Chem. Phys.* **2021**, (accepted for publication).

[198] Dral, P. O. *J. Phys. Chem. Lett.* **2020**, *11*, 2336–2347.

[199] Rasmussen, C.; Williams, C. *Gaussian processes for machine learning*; MIT Press, 2006; Vol. 14; pp 69–106.

[200] Alborzpour, J.; Tew, D.; Habershon, S. *J. Chem. Phys.* **2016**, *145*, 174112.

[201] Shepard, R. In *Modern Electronic Structure Theory*; Yarkony, D. R., Ed.; World Scientific: Singapore, 1995; pp 345–458.

[202] Heller, E. J. *J. Chem. Phys.* **1981**, *75*, 2923–2931.

[203] Fletcher, T.; Popelier, P. *J. Chem. Theory Comput.* **2016**, *12*, 2742–2751.

[204] Kandathil, S.; Fletcher, T.; Yuan, Y.; Knowles, J.; Popelier, P. *J. Comput. Chem.* **2013**, *34*, 1850–1861.

[205] Mills, M.; Popelier, P. *Theor. Chem. Acc.* **2012**, *131*, 1–16.

[206] Mills, M.; Popelier, P. *Comput. Theor. Chem.* **2011**, *975*, 42–51.

[207] Hinton, G.; Osindero, S.; Teh, Y.-W. *Neural Comput.* **2006**, *18*, 1527–1554.

[208] Kamath, A.; Vargas-Hernández, R.; Krems, R.; Carrington, J., T.; Manzhos, S. *J. Chem. Phys.* **2018**, *148*, 241702.

[209] Kolb, B.; Marshall, P.; Zhao, B.; Jiang, B.; Guo, H. *J. Phys. Chem. A* **2017**, *121*, 2552–2557.

[210] Cui, J.; Krems, R. *J. Phys. B: At., Mol. Opt. Phys.* **2016**, *49*, 224001.

[211] Loeppky, J.; Sacks, J.; Welch, W. *Technometrics* **2009**, *51*, 366–376.

[212] Mattos, C.; Dai, Z.; Damianou, A.; Barreto, G.; Lawrence, N. *J. Process Control* **2017**, *60*, 82–94.

[213] Han, J.; Zhang, X.-P.; Wang, F. *EEE J. Sel. Topics Signal Process.* **2016**, *10*, 1015–1028.

[214] Mahler, J.; Krishnan, S.; Laskey, M.; Sen, S.; Murali, A.; Kehoe, B.; Patil, S.; Wang, J.; Franklin, M.; Abbeel, P.; Goldberg, K. Learning accurate kinematic control of cable-driven surgical robots using data cleaning and Gaussian Process Regression. 2014 IEEE International Conference on Automation Science and Engineering (CASE). 2014; pp 532–539.

[215] Dral, P. O. In *Chemical Physics and Quantum Chemistry*; Ruud, K., Brändas, E. J., Eds.; Advances in Quantum Chemistry; Academic Press, 2020; Vol. 81; pp 291–324.

[216] Xu, C.; Liu, B.-G.; Liu, K.-Y.; Guo, J.-Q. *Rock and Soil Mechanics* **2011**, *32*, 1669–1675.

[217] Sundararajan, S.; Keerthi, S. *Neural Comput.* **2001**, *13*, 1103–1118.

[218] Koch, W.; Zhang, D. H. *J. Chem. Phys.* **2014**, *141*, 21101.

[219] Cawley, G. C.; Talbot, N. L. C.; Chapelle, O. Estimating Predictive Variances with Kernel Ridge Regression. Machine Learning Challenges. Evaluating Predictive Uncertainty, Visual Object Classification, and Recognising Tectual Entailment. Berlin, Heidelberg, 2006; pp 56–77.

[220] Richings, G.; Habershon, S. *J. Chem. Theory Comput.* **2017**, *13*, 4012–4024.

[221] Richings, G.; Habershon, S. *Chem. Phys. Lett.* **2017**, *683*, 228–233.

[222] Polyak, I.; Richings, G.; Habershon, S.; Knowles, P. *J. Chem. Phys.* **2019**, *150*, 041101.

[223] Polyak, I.; Richings, G. W.; Habershon, S.; Knowles, P. *J. Chem. Phys.* **2019**, *150*, 041101–5.

[224] Tao, S.; Chen, D.; Hu, W. *Journal of Chemical Industry and Engineering* **2007**, *58*, 1514–1517.

[225] Duan, K.; Keerthi, S.; Poo, A. *Neurocomputing* **2003**, *51*, 41–59.

[226] Keerthi, S. *IEEE Trans. Neural Netw.* **2002**, *13*, 1225–1229.

[227] Gold, C.; Sollich, P. *Neurocomputing* **2003**, *55*, 221–249.

[228] Bacis, R.; Bouvier, A.; Flaud, J. *Spectrochim. Acta A Mol. Biomol. Spectrosc.* **1998**, *54*, 17–34.

[229] Flaud, J.; Bacis, R. *Spectrochim. Acta A Mol. Biomol. Spectrosc.* **1998**, *54*, 3–16.

[230] Solomon, S. *Rev. Geophys.* **1999**, *37*, 275–316.

[231] Tanaka, T.; Morino, Y. *J. Mol. Spectrosc.* **1970**, *33*, 538–551.

[232] Braunstein, M.; Pack, R. *J. Chem. Phys.* **1992**, *96*, 6378–6388.

[233] Minaev, B.; Khomenko, E. *High Energy Chem.* **2006**, *40*, 230–233.

[234] Bouvier, A.; Wannous, G.; Churassy, S.; Bacis, R.; Brion, J.; Malicet, J.; Judge, R. *Spectrochim. Acta A Mol. Biomol. Spectrosc.* **2001**, *57*, 561–579.

[235] Braunstein, M.; Martin, R.; Hay, P. *J. Chem. Phys.* **1995**, *102*, 3662–3666.

[236] Banichevich, A.; Peyerimhoff, S.; Grein, F. *Chem. Phys.* **1993**, *178*, 155–188.

[237] Tsuneda, T.; Nakano, H.; Hirao, K. *J. Chem. Phys.* **1995**, *103*, 6520–6528.

[238] Borowski, P.; Fülscher, M.; Malmqvist, P.-Å.; Roos, B. *Chem. Phys. Lett.* **1995**, *237*, 195–203.

[239] Ndengué, S.; Gatti, F.; Schinke, R.; Meyer, H.-D.; Jost, R. *J. Phys. Chem. A* **2010**, *114*, 9855–9863.

[240] Grebenshchikov, S.; Qu, Z.-W.; Zhu, H.; Schinke, R. *Phys. Chem. Chem. Phys.* **2007**, *9*, 2044–2064.

[241] Hay, P.; Pack, R.; Walker, R.; Heller, E. *J. Phys. Chem.* **1982**, *86*, 862–865.

[242] Xie, D.; Guo, H.; Peterson, K. *J. Chem. Phys.* **2001**, *115*, 10404–10408.

[243] Xie, D.; Guo, H.; Peterson, K. *J. Chem. Phys.* **2000**, *112*, 8378–8386.

[244] Le, H.; Dinh, T.; Le, H. *J. Phys. Chem. A* **2011**, *115*, 10862–10870.

[245] Xantheas, S.; Atchity, G.; Elbert, S.; Ruedenberg, K. *J. Chem. Phys.* **1991**, *94*, 8054–8069.

[246] Woywod, C.; Stengle, M.; Domcke, W.; Flöthmann, H.; Schinke, R. *J. Chem. Phys.* **1997**, *107*, 7282–7295.

[247] Batista, V. S.; Miller, W. H. *J. Chem. Phys.* **1998**, *108*, 498–510.

[248] Qu, Z.-W.; Zhu, H.; Grebenshchikov, S.; Schinke, R. *J. Chem. Phys.* **2005**, *123*, 074305.

[249] Flöthmann, H.; Beck, C.; Schinke, R.; Woywod, C.; Domcke, W. *J. Chem. Phys.* **1997**, *107*, 7296–7313.

[250] Laude, G.; Calderini, D.; Tew, D.; Richardson, J. *Faraday Discuss.* **2018**, *212*, 237–258.

[251] Cooper, A.; Hallmen, P.; Kästner, J. *J. Chem. Phys.* **2018**, *148*, 094106.

[252] Tully, J. C.; Preston, R. K. *J. Chem. Phys.* **1971**, *55*, 562–572.